Doctoral Thesis

Dual contrast MRI for investigation of cerebrovascular alterations after ischemic stroke

MungSoo Kang

Department of Biomedical Engineering

Ulsan National Institute of Science and Technology

2021

Dual contrast MRI for investigation of cerebrovascular alterations after ischemic stroke

MungSoo Kang

Department of Biomedical Engineering

Ulsan National Institute of Science and Technology

Dual contrast MRI for investigation of cerebrovascular alterations after ischemic stroke

A thesis submitted to
Ulsan National Institute of Science and Technology
in partial fulfillment of the
requirements for the degree of
Doctor of Philosophy

MungSoo Kang

06.08.2021 of submission

Approved by

Advisor

HyungJoon Cho

MungSoo Kang

Dual contrast MRI for investigation of cerebrovascular alterations after ischemic stroke

MungSoo Kang

This certifies that the thesis of MungSoo Kang is approved.

06.08.2021 of submission

Signature

Advisor: HyungJoon Cho

Signature

Joon-Mo Yang

Signature

Woonggyu Jung

Signature

Jung-Hoon Park

Signature

Jae-Hyeok Lee

Abstract

Ischemic stroke induced by obstructed blood flow to the brain accounts for the majority of all strokes. Although diminished blood supply to the brain results in cell death, it promotes two phases of cerebrovascular remodeling, which are arteriogenesis and angiogenesis. Arteriogenesis is a process that improving collateral circulation for blood supply, while angiogenesis is a process that sprouting new capillaries for oxygen and nutrients supply. Through both cerebrovascular remodeling phases, brain macro- and microvascular remodeling occur. Appropriate macro- and microvascular remodeling after ischemic stroke have been shown to correlate with improved clinical outcomes and recovery. Consequently, simultaneous assessment of macro- and microvascular remodeling after ischemic stroke is a crucial process to evaluate the status of ischemic stroke. However, a non-invasive method for simultaneously assess the temporally heterogenous macro- and microvascular remodeling is not well established.

Ischemic stroke induced cerebral edema can be classified into several types including cytotoxic edema and vasogenic edema. Cytotoxic edema results in swelling of cells, which shows decreased magnetic resonance (MR) apparent diffusion coefficient (ADC), while vasogenic edema results in swelling of extracellular space, which shows increased ADC . Typically, pseudo-normalization of ADC occurs around a week after ischemic stroke (subacute phase). However, affected by accelerated development of vasogenic edema, the temporal occurrence of this pseudo-normalization of ADC could be spatially heterogeneous in ischemic edema lesions. The rapid development of vasogenic edema results in pseudo-normalization of ADC before a week after ischemic stroke. Lesions of ADC early pseudo-normalization showed more widespread and faster expansion into the chronic stage. As ischemic stroke triggers vascular remodeling, quantitative analysis of vascular remodeling difference between early pseudo-normalization and typical pseudo-normalization lesions can provide further diagnostic and prognostic information about ischemic stroke.

To directly visualize vessels, magnetic resonance angiography (MRA) is widely used in clinical and scientific fields with various imaging techniques. Among techniques, contrast agent aid contrast-enhanced (CE) MRA has intrinsically high signal-to-noise ratio, spatial resolution, and less sensitivity to blood flow compared to non-contrast MRA techniques, which are based on blood flow. However, the spatial resolution of MRA (approximately in-plane resolutions of 250 μm^2 for clinical MR scanner and 50 μm^2 for small animal MR scanner) limits direct visualization of the microvasculature. However, administration of blood-pool contrast agent enables morphological (size and density) and functional (blood flow and mean transit time) mapping of microvasculature. Measurement of alteration of transverse relaxation rates (ΔR_2 and ΔR_2^*) due to the administration of contrast agent can generate maps

of morphological information of microvasculature including vessel size index (VSI) and microvessel density (Q and MVD), while ΔR_2^* contrast-based dynamic susceptibility contrast (DSC)-MRI enables mapping of functional information of microvasculature including relative cerebral blood flow (rCBF) and mean transit time (rMTT).

In this thesis, firstly, the feasibility of dual contrast MRI for visualization of whole brain macro- and microvascular remodeling was verified by applying dual contrast MRI to transient middle cerebral artery occlusion (tMCAO) rat model. Using superparamagnetic iron oxide nanoparticles (SPION) as a blood-pool single contrast agent, macrovascular remodeling after ischemic stroke was longitudinally visualized using T_1 contrast-based ultra-short echo time (UTE) MRA, while morphological microvascular remodeling was visualized by mapping of ΔR_2 and ΔR_2^* contrast-based VSI, Q, and MVD. Monte Carlo simulation was performed to verify the feasibility of VSI, Q, and MVD at the MRI experimental conditions. Dual contrast MRI directly visualized ischemic stroke induced macrovascular remodeling occurs at the brain surface region from UTE-MRA. Also, the morphological microvascular remodeling that occurs at the brain inner region was simultaneously visualized by mapping of VSI, Q, and MVD.

Secondly, morphological and functional vascular remodeling were investigated in two spatiotemporally different ischemic edema lesions, which are early pseudo-normalization and typical pseudo-normalization lesions. Macrovascular remodeling, morphological (size and density) microvascular remodeling, and functional (blood flow and mean transit time) microvascular remodeling were simultaneously visualized by UTE-MRA, VSI, MVD, and rCBF, and rMTT, respectively. Longitudinal acquisition of dual contrast MRI verified the quantitative difference of macrovascular remodeling, morphological microvascular remodeling, and functional microvascular remodeling between the early pseudo-normalization and typical pseudo-normalization lesions. Also, light sheet fluorescence microscopy (LSFM) images validated the quantitative difference of MRI-derived microvascular remodeling between early pseudo-normalization and typical pseudo-normalization lesions.

In conclusion, ischemic stroke induced whole brain macro- and microvascular remodeling were investigated using dual contrast MRI. Using SPION as a single contrast agent, various vascular parameters were visualized and quantified. Also, the difference in vascular remodeling between early pseudo-normalization and typical pseudo-normalization lesions was investigated. Simultaneous visualization and quantification of whole brain macro- and microvascular remodeling by dual contrast MRI would provide further insight regarding ischemic stroke.

Contents

List of figures

Chapter 2. Background

2.1 MRI basic contrasts

2.2 3D UTE-MRA (morphology of macrovasculature)

2.4 DSC-MRI (function of microvasculature)

Chapter 3. Dual contrast MRI: Method

Chapter 4. Dual contrast MRI: Application

Chapter 1. Introduction

1.1 Purpose

The aim and content of this thesis can be summarized into two distinct subjects. One is to verify the feasibility of dual contrast MRI method for visualization of morphological macro- and microvascular remodeling after ischemic stroke using single superparamagnetic iron oxide nanoparticles (SPION) contrast agent. The other is to assess morphological and functional vascular remodeling differences between two heterogeneous edema lesions utilizing dual contrast MRI.

The detailed objectives of the research are as follows:

1) MRI visualization of whole brain macro- and microvascular remodeling in ischemic stroke rats
2) MRI investigation of vascular remodeling for heterogeneous edema lesions in subacute ischemic stroke rats

1.2 Outline

This thesis is organized as follows:

Chapter 2 introduces the background of this thesis. In this section, to understand the fundamental concept, detailed dual contrast MRI is explained including 3D ultra-short echo time magnetic resonance angiography (UTE-MRA), ΔR_2- ΔR_2^*-MRI, and DSC-MRI for morphological macrovascular remodeling, morphological microvascular remodeling, and functional microvascular remodeling, respectively.

Chapter 3 describes the feasibility of dual contrast MRI for visualization of morphological macro- and microvascular remodeling in a transient middle cerebral artery occlusion (tMCAO) rat model. In ischemic edema lesions measured by apparent diffusion coefficient (ADC), macro- and microvascular remodeling are visualized and quantified.

Chapter 4 describes quantitative assessment of morphological and functional vascular remodeling differences between two heterogeneous edema lesions by application of dual contrast MRI. Not only edema lesion status via ADC and T_2, but also various vascular parameters are observed and quantitively analyzed. Also, correlation between morphological microvascular remodeling and functional microvascular remodeling is verified.

Chapter 5 provides the summary and conclusions of this thesis.

1.3 Abbreviations

ADC	Apparent diffusion coefficient
BVf	Blood volume fraction
CBF	Cerebral blood flow
CBV	Cerebral blood volume
CE	Contrast enhanced
cRHV	caudal rhinal vein
DCV	Dorsal cerebral vein
DLS	Differential light scattering
DSC-MRI	Dynamic susceptibility contrast – magnetic resonance imaging
EPI	Echo planar imaging
FA	Flip angle
FOV	Field of view
FPM	Finite perturber method
GRE	Gradient echo
IACUC	Institutional animal care and use committee
KESM	Knife-edge scanning microscopy
LSFM	Light sheet fluorescence microscopy
MC	Monte carlo
MCA	Middle cerebral artery
MEGE	Multi echo gradient echo
MIP	Maximum intensity projection

MRA	Magnetic resonance angiography
MRI	Magnetic resonance imaging
MSME	Multi slice multi echo
MTT	Mean transit time
MVD	Microvessel density
NA	Number of averages
NR	Number of repetitions
ROI	Region of interest
SE	Spin echo
SNR	Signal to noise ratio
SPION	Superparamagnetic iron oxide nanoparticles
TE	Echo time
tMCAO	transient middle cerebral artery
TR	Repetition time
UTE	Ultra-short echo time
VSI	Vessel size index

Chapter 2. Background

2.1 MRI basic contrasts

As a non-invasive medical imaging technique, magnetic resonance imaging (MRI) is widely used to explore the anatomy and physiology of whole body with high sensitivity and flexibility in clinical and scientific fields. Unlike x-ray and computed tomography (CT), MRI scanning does not result in exposure to ionizing radiation. Fundamentals of MRI can be understandable as interaction between applied magnetic field and a nucleus that possesses spin. Atomic nuclei possessing odd number of protons or neutrons have a non-zero spin. intensity of magnetic resonance (MR) signal is proportional to gyromagnetic ratio, which is a nucleus depended constant. Single proton hydrogen (^{1}H) is by far the most studied due to its abundance in human body. Other nuclei with an odd number of protons or neutrons such as carbon (^{13}C), sodium (^{23}Na), oxygen (^{17}O), and nitrogen (^{15}N) can be used for MRI as well. However, there are limitations of relatively low abundance or small gyromagnetic ratio compared to hydrogen (^{1}H).

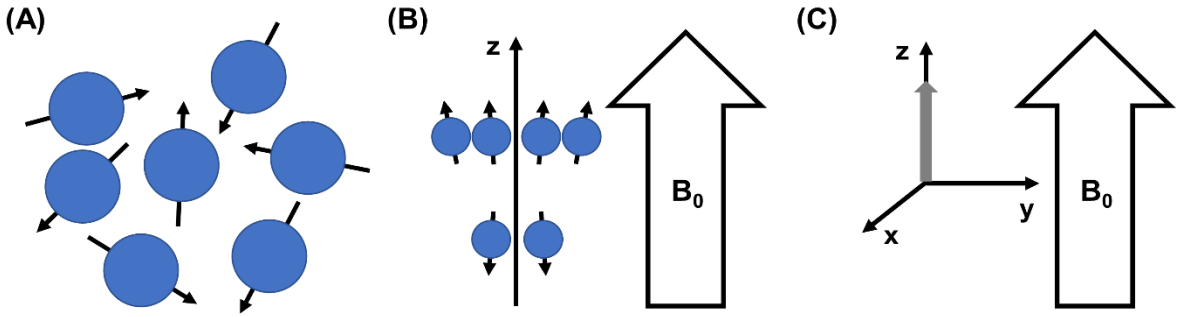

Figure 2.1.1 The spin behavior in absence and presence of external magnetic field. (A) Randomly oriented spin vectors with absence of external magnetic field (B_0). (B) Parallel alignment of spin vectors with presence of external magnetic field (B_0). (C) Formation of net magnetization (gray arrow in z axis) with parallel and same direction of external magnetic field (B_0).

The net magnetization vector from numerous spins is exclusively used to explain MRI signal behavior. Without an external magnetic field, each spin vector orients randomly. On the contrary, with presence of an external magnetic field B_0, spins will be aligned to parallel direction to B_0 with two directions (positive and negative to B_0 direction). But, there are slightly more positive spins that make non-zero net magnetization with parallel and same direction to the B_0. The depiction of spin behavior in absence and presence of B_0 is shown in Figure 2.1.1. In equilibrium state, net transverse (x-y plane) magnetization is zero. Generally, z-axis is the direction B_0. The main signal source of MRI is net magnetization and it is affected by several factors including the magnetic field strength, spin density,

and temperature.

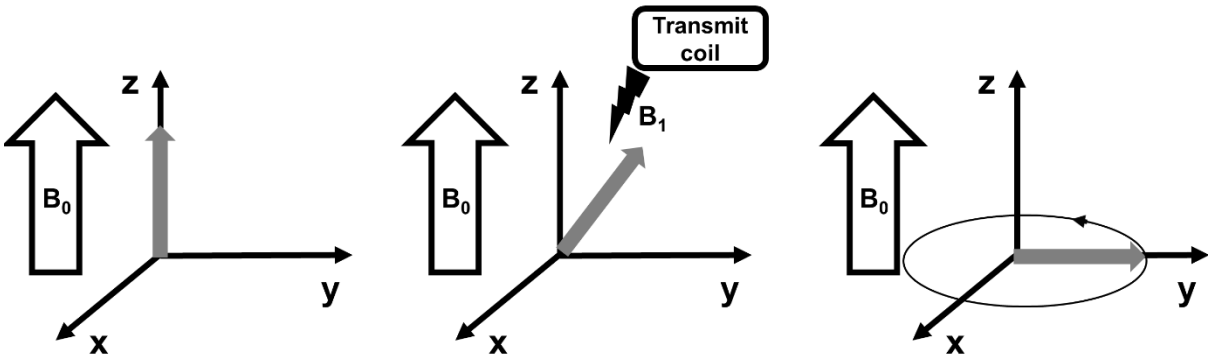

Figure 2.1.2 The interaction between the net magnetization and the RF magnetic field.

To generate MR signal, oscillating magnetic field with resonance frequency of spin is required in addition to magnetic field B_0. As resonance frequency of spin is in the range of radio frequency (RF), the oscillating magnetic field (B_1) is induced from RF pulse. Amplitude of generated B_1 field is weaker than B_0 field. Application of the RF pulse from transmit coil with short duration (~ ms) tip down the net magnetization into the x-y plane to form transverse magnetization. The duration and amplitude of RF pulse determine a flip angle of net magnetization. Figure 2.1.2 describes the interaction between the net magnetization and the RF pulse.

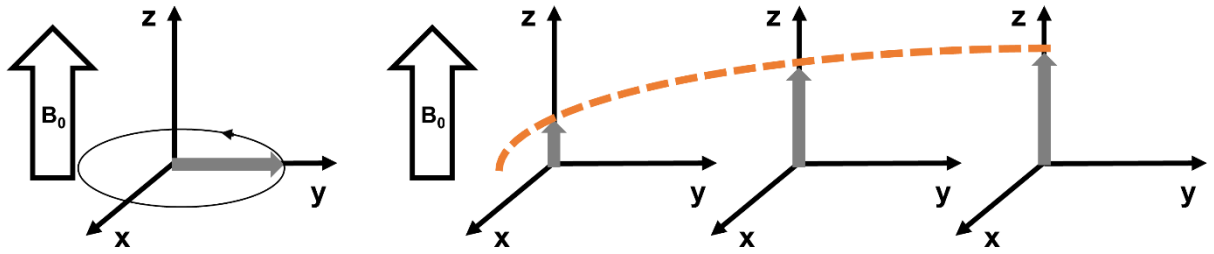

Figure 2.1.3 The process that transverse magnetization back to an equilibrium state (T_1 relaxation).

After formation of the transverse magnetization from RF pulse, the transverse magnetization goes back to its equilibrium state (z-axis). This process is called the longitudinal (T_1) relaxation or spin-lattice relaxation. The name of spin-lattice relaxation is derived from that spin gives energy back to the surrounding lattice. The T_1 relaxation depends on energy exchange between spin and its lattice. Simultaneously, there is a transverse (T_2) relaxation or spin-spin relaxation induced from the reducing transverse magnetization. The name of spin-spin relaxation is derived from that each spin affect neighbor spins. The interaction of spins randomly changes local magnetic fields. This process result in loss of phase coherence and gradually reduce the transverse magnetization. The T_1 is defined as a relaxation time when 63% of longitudinal (z-axis) magnetization recovers its equilibrium state and the T_2 is a relaxation time when transverse magnetization is reduced to 37% of its initial transverse

magnetization. The T_1 relaxation is always longer than the T_2 relaxation. Through Figure 2.1.3 and Figure 2.1.4, T_1 and T_2 relaxation processes are described, respectively.

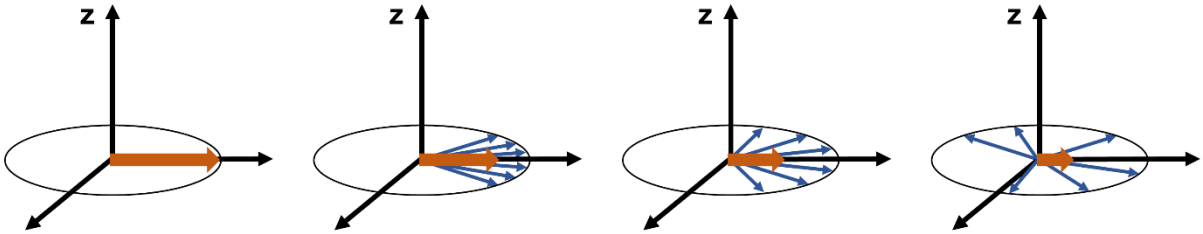

Figure 2.1.4 The process of transverse magnetization reduction (T_2 relaxation).

As a transverse relaxation, there is a T_2^* relaxation in addition to T_2 relaxation. The T_2^* relaxation has additional transverse magnetization decaying factor which is T_2' relaxation and described as following equation:

$$\frac{1}{T_2^*} = \frac{1}{T_2} + \frac{1}{T_2'} \quad (2.1.1)$$

In contrast to irreversible T_2 relaxation, T_2' relaxation is from a static magnetic field inhomogeneity resulted from magnetic susceptibility differences and is reversible. The spin echo (SE) based pulse sequence uses additional RF pulse as refocusing pulse to recover signal decay from the T_2' relaxation. However, the T_2' relaxation provides essential information regarding magnetic susceptibility. To manipulate the T_2^* relaxation, gradient echo (GRE) based pulse sequences are generally used. The GRE based pulse sequence uses bipolar magnetic field gradient. One direction of magnetic field gradient is applied as dephasing gradient to accelerate loss of spin coherence by changing local magnetic fields. Subsequently, the opposite direction of magnetic field gradient is applied as rephrasing gradient to reverse spin incoherence induced from previous dephasing gradient. Generally, the Bloch equation is used to express the MR signal of SE as following:

$$MR\ Signal = M_0\left(1 - \exp\left(-\frac{TR}{T_1}\right)\right)\exp\left(-\frac{TE}{T_2}\right) \quad (2.1.2)$$

Where M_o is a proton density, T_1 and T_2 are relaxation time, TR is a repetition time, and TE is an echo time. For MR signal of GRE, modified Bloch equation is used due to the flip angle (FA) α, which affect T_1 relaxation effect and expressed as following:

$$MR\ Signal = M_0\frac{\sin\alpha\left(1-\exp\left(-\frac{TR}{T_1}\right)\right)}{\left(1-(\cos\alpha)\exp\left(-\frac{TR}{T_1}\right)\right)}\exp\left(-\frac{TE}{T_2^*}\right) \quad (2.1.3)$$

The M_0, T_1, and T_2 (or T_2^*) are inherent constant and different depending on tissue type. The TR and

TE are adjustable MR parameters and they determine the weights of M_0, T_1, T_2 and (or T_2^*) for various MR image contrasts. For example, long TE allows distinguishing relative differences of signal decay among various tissues. It enhances the T_2 or T_2^* effect. On the contrary, short TE minimizes the T_2 or T_2^* effect. For long TR, all transverse magnetizations from various tissues have time to back to their equilibrium state, which makes no significant signal difference. It minimizes the T_1 effect. On the contrary, short TR enhances the T_1 effect. Consequently, short TR and TE can generate T_1-weighted image, while long TR and TE can generate T_2-weighted or T_2^*-weighted images. In case of long TR and short TE, proton density weighted image can be acquired.

2.2 3D UTE-MRA (morphology of macrovasculature)

Generally, the MRA technique has been utilized to assess various vascular information. Over many decades, various MRA techniques have been developed and implemented in clinical and scientific fields. Among MRA techniques, contrast enhanced MRA (CE-MRA) is a technique acquired with the aid of contrast agent [1]. Contrast agent shortens relaxation times (T_1, T_2, and T_2^*) and offers additional contrast. The relaxation rate after administration of contrast agent can be expressed as following equations [2-4]:

$$\frac{1}{T_1} = r_1 \cdot C + \frac{1}{T_{1t}}, \ \frac{1}{T_2} = r_2 \cdot C + \frac{1}{T_{2t}} \quad (2.2.1)$$

Where r_1 and r_2 (or r_2^*) are relaxivities of contrast agent and they are depending on several factors including magnetic field strength and temperature. The C is concentration of contrast agent and the T_{1t} and T_{2t} (or T_{2t}^*) represent intrinsic tissue T_1 and T_2 (or T_2^*) properties. Other non-contrast MRA techniques that do not use any contrast agent, typically rely on the blood flow to visualize vasculature [5]. These techniques are extensively implemented in clinical field because they do not require any contrast agent. However, non-contrast MRA techniques are affected mainly by artery due to their fast blood flow compared to veins. To visualize veins, blood oxygen level-dependent (BOLD) effect induced by alterations of paramagnetic deoxyhemoglobin in blood vessels has been utilized as non-contrast MRA [6,7]. In contrast to non-contrast MRA, the CE-MRA can simultaneously visualize arteries and veins. Commonly, T_1 contrast enhanced MRA with gadolinium (Gd) based contrast agent is acquired [8-10]. After administration of Gd-based contrast agent, T_1 of blood is reduced and result in improvement of the vessel-tissue contrast. Superparamagnetic iron oxide nanoparticles (SPION) contrast agent can be utilized as T_1 contrast enhanced MRA as well. As SPION has characteristics of adequate size, high relaxivities and relatively long plasma half-life, it is utilized as blood pool contrast

agent. Most blood pool contrast agents have high molecular weight, which prevent them leaking from vessel to interstitial space.

Ultra-short echo time (UTE) is MRI pulse sequence that utilized to image tissue components having short T_2 with an extremely short TE [11]. The implementation of 3D allows much reduced TE compared to 2D due to non-selective RF excitation. The UTE pulse sequence radially samples k-space, which is a grid of raw data acquired directly from the MR signals. After a hard RF pulse for non-selective RF excitation, echoes are immediately collected to the k-space with center-out and half-radial sampling by all three directions of imaging gradients. The center-out and half-radial sampling of 3D UTE offers the shortest executable TE and insensitivity to motion and flow artifacts because it inherently compensates the flow [12]. Figure 2.2.1 shows k-spaces with radial sampling and conventional cartesian sampling. The radial sampling method inherently performs oversampling the center of k-space. This overlapping can be utilized for motion detection and correction. The radial sampling results in high sampling density in center k-space and low sampling density in outer k-space. The drawback of radial sampling is that non-uniformly sampled k-space should be gridded to form a cartesian grid before image formation and image processing. Implementation of the 3D UTE-MRA can visualize morphology of vasculature.

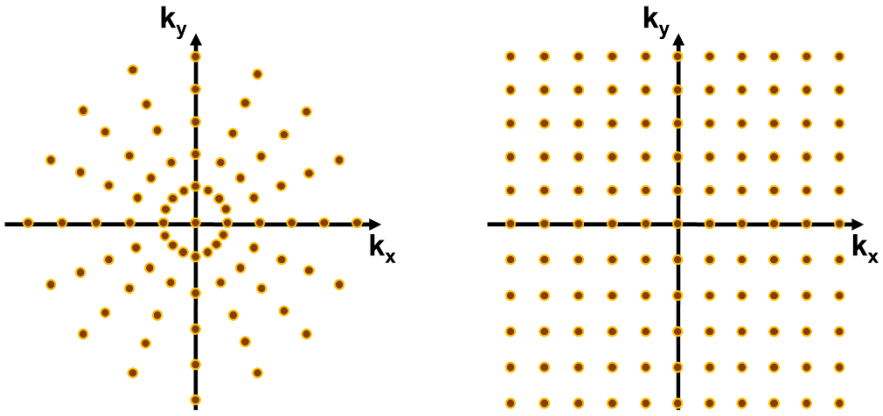

Figure 2.2.1 K-spaces with radial sampling (left) and cartesian sampling (right).

2.3 ΔR_2-ΔR_2^*-MRI (morphology of microvasculature)

Although MRA technique offers direct visualization of vasculature, the spatial resolution limitation of MRI hamper its application to assess microvasculature. Characterization of microvasculature could provide information about diseases. However, analytical approaches verified feasibility that utilizing alteration of transverse relaxation rates (ΔR_2 and ΔR_2^*), which are induced from administration of contrast agent, can visualize morphology of microvasculature such as vessel size and density [13]. Both

dynamic and steady-state acquisition methods can acquire SE based ΔR_2 and gradient echo based ΔR_2^*. The dynamic acquisition method allows faster acquisition of ΔR_2 and ΔR_2^* at the expense of the coverage and spatial resolution. On the contrary, compared to the dynamic acquisition method, the steady-state acquisition method offers high spatial resolution and large coverage at the expense of scan time. For the morphology of microvasculature, vessel size index (VSI) and vessel density (Q and MVD) can be acquired by following equations [13,14]:

$$\text{VSI } (\mu m) = 0.424(ADC/(\gamma \Delta\chi B_0))^{1/2}(\Delta R_2^*/\Delta R_2)^{3/2} \quad (2.3.1)$$

$$Q\ (s^{-1/3}) = \Delta R_2/(\Delta R_2^*)^{2/3} \quad (2.3.2)$$

$$MVD\ (mm^{-2}) \approx Q^3/(4.725ADC) \quad (2.3.3)$$

Where γ is the gyromagnetic ratio and B_0 is the strength of main magnetic field. Apparent diffusion coefficient (ADC) is the term reflecting magnitude of diffusion within tissue. The ADC is measured by diffusion weighted imaging (DWI) technique of MRI. The $\Delta\chi$ is the intravascular susceptibility difference due to the administration of contrast agent. The $\Delta\chi$ depends on the concentration of contrast agent and calculated by following equation:

$$\Delta\chi = \frac{3\Delta R_2^*}{4\pi\ BVf\ \gamma\ B0} \quad (2.3.4)$$

The BVf is the blood volume fraction. Since the introduction of the VSI, Q, and MVD, they have been successfully implemented to assess microvascular size and density in clinical and scientific fields. Also, other validation studies verified quantitative consistency of MRI-derived VSI, Q, and MVD.

2.4 DSC-MRI (function of microvasculature)

Utilizing diverse MRI techniques, not only morphological information but also functional information about microvasculature can be acquired. For functional microvascular information, perfusion MRI techniques are generally used. As a perfusion MRI technique, dynamic susceptibility contrast MRI (DSC-MRI) provides hemodynamic parameters, which are cerebral blood volume (CBV), cerebral blood flow (CBF), and mean transit time (MTT) [15-17]. A susceptibility from contrast agent passing through capillary network results in regional signal loss, which DSC-MRI technique exploits. For the DSC-MRI technique, both T_2 and T_2^* MR sequences can be used. However, T_2-based DSC-MRI requires higher dose of contrast agent compared to T_2^*-based DSC-MRI. Consequently, using GRE echo-planar imaging (EPI) pulse sequence, T_2^*-based DSC-MRI is generally employed [18].

For detection of signal loss, rapidly repeated images of the tissue are acquired during intravenous bolus administration of contrast agent. The susceptibility-induced signal loss is primarily affected by amount of the contrast material primarily in the microvasculature [18,19]. Measured time-series signal alteration can be converted to alteration of transverse relaxation rate with the following equation [20]:

$$\Delta R_2^*(t) = -\frac{1}{TE}\ln\left(\frac{S(t)}{S_{pre}}\right) \quad (2.4.1)$$

Where S_{pre} is an averaged signal before the administration of contrast agent. During the first passage of contrast agent, time-series signal alteration induced ΔR_2^* curve should be acquired. However, affected by recirculation, mixed curve is measured as shown in Figure 2.4.1. To eliminate contribution of recirculation, the ΔR_2^* curve is commonly fitted with gamma-variate function [21,22]:

$$\Delta R_2^*(t) = Kt^{\alpha}\exp(-\beta t) \quad (2.4.2)$$

Where K, α, and β are constant and arbitrary parameters, respectively. Subsequently, perfusion parameters which are relative CBV (rCBV), MTT, and relative (rCBF) can be acquired with the following equations [15,22]:

$$rCBV = \int_0^t \Delta R_2^*(\tau)d\tau$$

$$MTT = \frac{\int_0^t \tau\Delta R_2^*(\tau)d\tau}{\int_0^t \Delta R_2^*(\tau)d\tau} \quad (2.4.2)$$

$$rCBF = \frac{rCBV}{MTT}$$

The rCBV can be acquired by measuring area under ΔR_2^* curve, while the MTT can be acquired by using the non-deconvolved ΔR_2^* curve. By dividing previously acquired rCBV and MTT, the rCBF can be acquired.

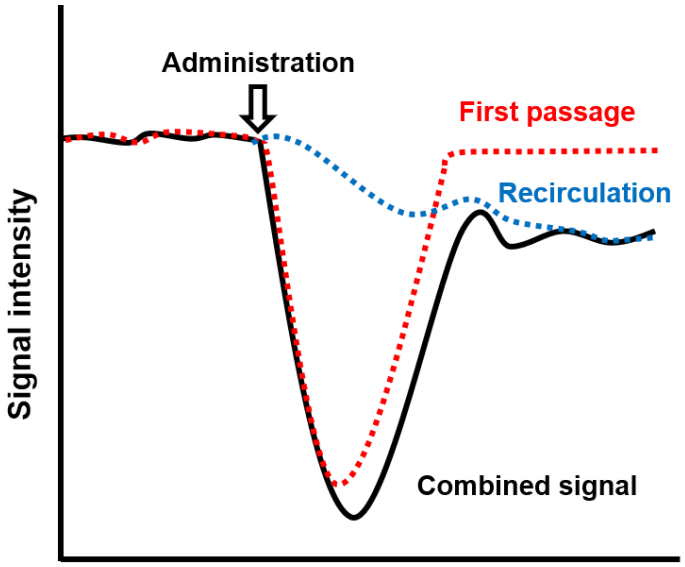

Figure 2.4.1 DSC-MRI signal intensity curve.

Chapter 3. Dual contrast MRI: Method

3.1 Introduction

Obstruction of the blood supply to part of the brain causes an ischemic stroke. Although diminished blood flow can result in cell death, it typically promotes two-phase cerebrovascular remodeling involving arteriogenesis and angiogenesis. Arteriogenesis, induced by physical forces such as fluid shear stress and circumferential wall stress, is a process that improves collateral circulation by vasodilating pre-existing circulatory anastomoses [23]. Vasodilation lasts until the physical forces are normalized [24]. Then, the dilated vessels are known to return to their normal diameter [25]. However, the remodeling of venous vessel size and its association with ischemic edema status is rarely investigated in the post-ischemic brain. Angiogenesis is triggered by hypoxia and induces pro-angiogenic factors that result in the sprouting of new capillaries from pre-existing vessels for maintenance or restoration of local oxygen and nutrition supplies [23,26]. In general, arteriogenesis is involved in both macro- and microvascular remodeling, while angiogenesis is a mechanism of microvascular remodeling. Adequate collateral circulation status through arteriogenesis and increased microvessel density through angiogenesis have been shown to correlate with better clinical outcomes and recovery after ischemic stroke [27-35]. However, noninvasive methods for simultaneously assessing morphological macro- and microvascular remodeling after ischemic stroke have not been established, and there is little experimental evidence of the need for such evaluation.

As a noninvasive imaging modality, magnetic resonance imaging (MRI) can provide morphological information about the vascular system. With those advantages, MRI is being widely used to investigate vascular remodeling after ischemic stroke. Time of flight MR angiography (TOF-MRA) has revealed an association between arteriogenic collateral circulation and clinical outcomes [36-38]. In a preclinical study of transient middle cerebral artery occlusion (tMCAO) in a rat model, TOF-MRA showed that macrovascular remodeling occurred at the rat brain surface region [39]. However, previous TOF-MRA studies on the ischemic stroke brains have focused mainly on arterial blood vessels, and vascular remodeling of venous pial vessels has hardly been studied to our knowledge. Also, the low spatial resolution of MRA limits the direct local morphological visualization of microvascular remodeling [23].

On the other hand, the spatial changes of MR signals can be measured with the administration of a blood-pool contrast agent, enabling morphological mapping of the macro- and microvasculature. To obtain morphological information regarding the entire macrovasculature, high resolution 3-dimensional T_1-contrast-based ultra-short echo time MR angiography (UTE-MRA) can be used [40,41]. To obtain morphological information about the microvasculature, vessel size index (VSI) and microvessel density indices (Q and MVD) can be measured. VSI, Q, and MVD values obtained through alteration of

transverse relaxation rates (ΔR_2 and ΔR_2^*) due to the administration of contrast agent [13,42,43] can be used to map morphological microvascular alterations after ischemic stroke [44-50]. As arteriogenesis and angiogenesis are likely to correlate with recovery after ischemic stroke, the association between vessel morphology and corresponding tissue ischemic edema status (via apparent diffusion coefficient [ADC])) can be verified by simultaneous assessment of total macro- and microvascular remodeling in the ischemic brain.

In this pilot study, we performed dual contrast MRI using superparamagnetic iron oxide nanoparticles (SPION) as a single contrast agent [40,41]. We used Monte Carlo simulation to optimize the dose of SPION by correlating ΔR_2 and ΔR_2^* values at various vessel sizes/volumes at 7-T. High resolution (59 μm^3) 3-dimensional UTE-MRA was combined with ΔR_2- ΔR_2^*-MRI derived VSI/Q/MVD maps on tMCAO rat models. Such dual contrast MRI acquisition enabled simultaneous morphological visualization of macrovascular size remodeling at the brain surface region and microvascular size/density remodeling at the deep inner brain region. ADC values, macrovascular diameters (UTE-MRA) and microvascular size /density (VSI/Q/MVD) in cortical and subcortical regions were respectively evaluated and compared to elucidate the morphological responses of the cerebral vascular system in rat brain during recovery of ischemic stroke.

3.2 Materials and methods

3.2.1 Animal preparation

All animal experiments were approved by the Institutional Animal Care and Use Committee (IACUC) of the Ulsan National Institute of Science and Technology (UNIST) and carried out in accordance with the Animal Protection Act of Korea and Guide for the Care and Use of Laboratory Animals of the National Institutes of Health. Adult male Wistar rats (body weight 280-320 g) were housed in cages under a 12 h light/12 h dark cycle with *ad libitum* access to food and water. Rats were initially anesthetized by inhalation of 3% isoflurane in a mixture of 30% oxygen and 70% nitrous oxide and isoflurane was maintained in the range of 1~1.5% during surgery and MRI acquisition. As isoflurane and nitrous oxide is known to involve some degree of vessel dilations, vasculatures in contralateral brains were used as a reference to monitor any ipsilateral vascular alterations. Body temperature was kept constant (37 $\pm$ 1 ℃) by using a warm-water circuit integrated into the animal bed and a feedback-controlled heating pad for MRI acquisition and surgery, respectively. Focal brain ischemia was induced by transient occlusion of the middle cerebral artery (MCA) according to a previously described method [51,52] with an intraluminal monofilament (0.37 mm diameter filament, Doccol Corporation, Redlands, CA, USA). After 60 min of occlusion, the filament was withdrawn and the wound was sutured under

local anesthesia. MRI acquisitions were performed on the tMCAO rats up to reperfusion day 7 after surgery.

3.2.2 Microvessel size and density simulation

Monte Carlo simulation was performed to optimize the dose of SPION and examine the feasibility of vessel size-related VSI and microvessel density-related Q and MVD by comparing them with input vascular size and vascular density in experimental MRI parameters, similar to the methods used in a previous study [13]. The simulation was implemented via in-house MATLAB (MathWorks, Natick, MA) scripts, which are based on the finite perturber method (FPM) [53] and analogous to previously described procedures [41,54,55]. Randomly oriented cylinders were generated in a 3-dimensional binary matrix ($400 \times 400 \times 400$) to represent microvessels in a tissue. The magnetic field shift (ΔB) was calculated as the sum of magnetic field shifts from all the perturbers. As simulation parameters, the main magnetic field (B_0) was set to 7-T and the magnetic susceptibility difference between the intravascular contrast agent and nearby tissue ($\Delta\chi$) was set to 4.5×10^{-7} (CGS unit) corresponding to a SPION dose of 360 μmol Fe/Kg (20.106 mg/Kg) [41,56]. The Monte Carlo simulation was performed consecutively for the estimation of ΔR_2 and ΔR_2^* values. Initially, 64,000,000 ($400 \times 400 \times 400$) protons were positioned uniformly within the diffusion space. In the periodic boundary condition, each proton was diffused to an adjacent position in the simulation unit time (Δt) of 1 ms, with the diffusion length of $\sqrt{2D\Delta t}$ (D: diffusion coefficient, 800 $\mu m^2/s$). The phase accumulation of each proton during diffusion time induced from different magnetic field shifts according to the position of each proton was calculated. Subsequently, ΔR_2 and ΔR_2^* values from the MR signal estimated by averaging the accumulated phase of total diffusing protons were calculated with $\Delta R_2, \Delta R_2^* = -\frac{\ln[S(TE)]}{TE}$. TEs for the simulation and calculation of ΔR_2 and ΔR_2^* values were 8 ms and 3 ms, respectively. Based on simulated ΔR_2 and ΔR_2^* values, VSI/Q/MVD values were calculated with the following equations [13,14,42,43]:

$$\text{VSI } (\mu m) = 0.424(D/(\gamma \Delta\chi B_0))^{1/2}(\Delta R_2^*/\Delta R_2)^{3/2} \quad (1)$$

$$Q\ (s^{-1/3}) = \Delta R_2/(\Delta R_2^*)^{2/3} \quad (2)$$

$$\text{MVD } (mm^{-2}) \approx Q^3/(4.725D) \quad (3)$$

To simulate various microvascular conditions, different vascular radii (2-10 μm) were generated with several blood volume fractions (Bvfs) of 2%, 4%, and 6%. The MR signal simulation for each condition was repeated ten times and reported as the mean value $\pm$ standard deviation (SD).

3.2.3 MRI acquisition

All MRI acquisitions were carried out on a 7-T MR scanner (Bruker, Ettlingen, Germany) with a 40-mm volume coil. Before administration of SPION, ADC, R_2, and R_2^* maps were acquired. After administration of SPION, subsequent R_2 and R_2^* maps were sequentially acquired to generate ΔR_2 and ΔR_2^* maps. Lastly, UTE-MRA was acquired after the measurement of ΔR_2 and ΔR_2^*. SPION was synthesized in house[18]. The core size distribution of the iron oxide was 5 to 10 nm. Based on differential light scattering (DLS) experiment, the mean hydrodynamic diameter of the iron oxide nanoparticles was 20 ± 7 nm. The r_1 and r_2 of SPION were 2.36 $mM^{-1}s^{-1}$ and 32.94 $mM^{-1}s^{-1}$ at 7-T. SPION was administered as an intravenous bolus with a dose of 360 μmol Fe/Kg (optimized dose from simulation). For the experimental validations, two normal rats were scanned before and after SPION administration for UTE-MRA and two tMCAO rats were studied at 1 day after reperfusion for ΔR_2-ΔR_2^*-MRI. Then, four tMCAO rats were studied at 1, 4, and 7 days after reperfusion for the quantification of macro- or microvascular remodeling with corresponding ADC measurements.

The ADC map was acquired using a diffusion-weighted echo planar imaging (EPI) pulse sequence with the following parameters: TR/TE = 3500/25.2 ms; number of averages (NA) = 8; number of segments = 3; b-values = 100, 200, 400, 600, 800, and 1000 $s \cdot mm^{-2}$; flip angle (FA) = 90 °; matrix size = 100 × 100; field of view (FOV) = 30 × 30 mm^2; resolution = 300 × 300 μm^2; number of slices = 8; slice thickness = 1 mm.

The ΔR_2 map was acquired using a multi-slice multi-echo (MSME) pulse sequence with the following parameters: TR = 6000 ms; TE = 8-160 ms; echo spacing = 8 ms; NA =1; FA = 90 °; matrix size = 256 × 256; FOV = 30 × 30 mm^2; resolution = 117 × 117 μm^2; number of slices = 8; slice thickness = 1 mm.

The ΔR_2^* map was acquired using a multi-echo gradient echo (MEGE) pulse sequence with the following parameters: TR = 6000 ms; TE = 3-59 ms; echo spacing = 4 ms; NA = 1; FA = 90 °; matrix size = 256 × 256; FOV = 30 × 30 mm^2; resolution = 117 × 117 μm^2; number of slices = 8; slice thickness = 1 mm.

The UTE-MRA was acquired using an ultra-short echo time (UTE) pulse sequence with the following parameters: TR/TE = 22/0.012 ms; NA = 1; FA = 40 °; under-sampling factor = 1.13; matrix size = 512 × 512 × 512; FOV = 30 × 30 × 30 mm^3; resolution = 59 × 59 × 59 μm^3.

3.2.4 Data processing and analysis

Data processing and analysis were performed with MATLAB, RStudio (RStudio, Boston, MA), and ImageJ (US National Institutes of Health, Bethesda, MD) software. Voxel-wise ADC values were

obtained by fitting the mono-exponential decay equation $S = S_0 \times \exp(-ADC \times b\text{-value})$ with a nonlinear least-squares-fitting method.

The ΔR_2 and ΔR_2^* values were calculated by subtracting the transverse relaxation rates (R_2 and R_2^*) values acquired before administration of SPION from the R_2 and R_2^* values acquired after administration of SPION. Voxel-wise R_2 and R_2^* values were obtained by fitting the mono-exponential decay equation $S = S_0 \times \exp(-TE \times [R_2 \text{ or } R_2^*])$. ΔR_2 and ΔR_2^* maps were used to determine VSI, Q, and MVD maps following equations (1), (2), and (3).

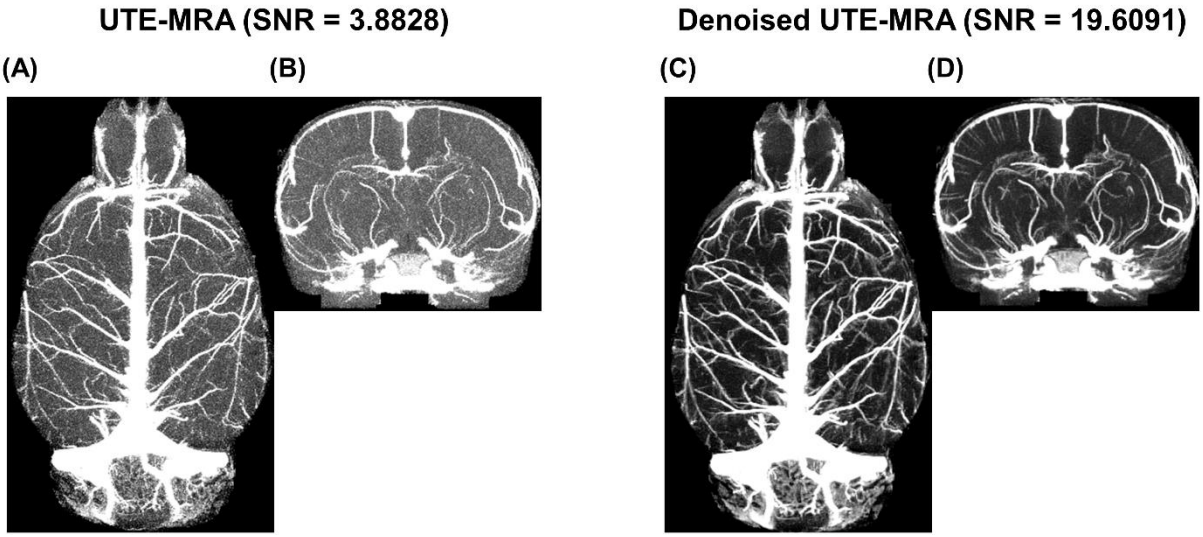

Figure 3.1 Original and BM4D filter applied UTE-MRAs. Dorsal views (A and C) and anterior-to-posterior views (B and D) of normal rat brain UTE-MRA and BM4D filter applied UTE-MRA with 60-slices maximum intensity projection and application of the same threshold value, respectively. SNR values of 3.8828 and 19.6091 for UTE-MRA and BM4D filter applied UTE-MRA, respectively.

Acquired UTE-MRAs were denoised by application of a BM4D filter [57]. Improved signal-to-noise ratio (SNR) in BM4D filter applied UTE-MRA is shown in Figure 3.1. The brain region of each UTE-MRA was segmented using a rat brain atlas [58] for visualization of brain vasculature only. Volume rendered UTE-MRAs were thresholded and visualized by 3DSlicer software (www.slicer.org) for the investigation of macrovascular remodeling in tMCAO rat models. The boundary value between noise and signal was set as a threshold value to delineate vasculature. In the accompanying figures, UTE-MRAs with the bluish and the yellowish regions represent brain tissue and brain vasculature, respectively. For the acquisition of vascular diameters from UTE-MRA, vasculatures in the UTE-MRA were segmented and thresholded. The same threshold value was set for each tMCAO rat model to reduce bias from diameter calculation. Based on binary images, the vascular diameters were calculated by fitting maximal spheres to every point in the vascular structure [59] via BoneJ software [60]. The

average diameter of the fitted sphere in the main vascular branch was determined as the corresponding vessel diameter. Also, the standard deviation was calculated to represent the error bar.

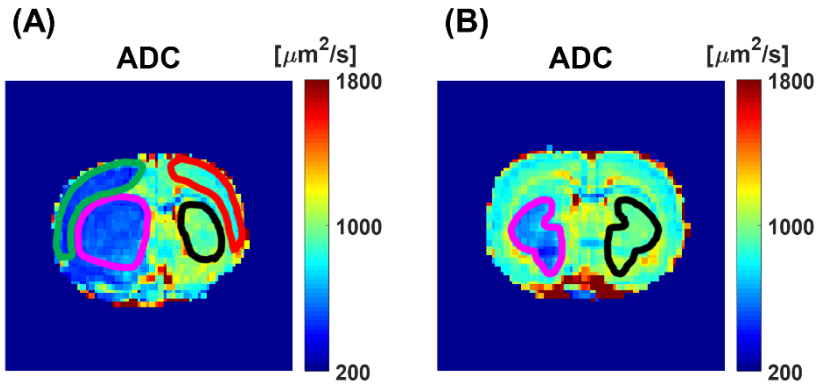

Figure 3.2 Scheme for cortex and subcortex segmentation. Representative ROIs for cortical and subcortical ischemic edema regions in ipsilateral hemisphere and corresponding normal regions in the contralateral hemisphere (A). Representative ROIs for subcortical ischemic edema region in ipsilateral hemisphere and corresponding normal region in contralateral hemisphere (B). A green line indicates ROI of cortical ischemic edema region in ipsilateral hemisphere, a red line indicates ROI of corresponding cortical normal region in contralateral hemisphere, purple lines indicate ROIs of subcortical ischemic edema regions in ipsilateral hemispheres, and black lines indicate ROIs of corresponding subcortical normal regions in contralateral hemisphere.

Cortical and subcortical regions of the ipsilateral and contralateral hemispheres were selected and segmented from the ADC map (4 or 5 slices to cover whole brain ischemic edema) of each experiment as shown in Figure 3.2. The values of ADC, VSI, Q, and MVD in the corresponding area were calculated and evaluated. Subsequently, relationship between the ADC value of the cerebral cortex and the pial venous (cRHV and DCV) and arterial (MCA) vessel diameters (derived from UTE-MRA) were shown using a bar graph for ischemic edema (ADC_{mean} < 650 μm²/s) and normal tissue (ADC_{mean} > 650 μm²/s), respectively. Correspondingly, correlation between the subcortical ADC and VSI/Q/MVD values (derived from ΔR_2-ΔR_2^*-MRI) were shown using a double box plot for ischemic edema and normal tissue, respectively. Conclusively with combined data from all experiments, Student's t-tests were performed to assess the significant differences of MR-derived vascular morphological parameters between the ischemic edema and normal tissue. As a validation study of MR-derived VSI, 3-dimensional mouse brain microvascular data from the (knife-edge scanning microscope) KESM brain atlas (http://kesm.cs.tamu.edu/home/index.php) was used [61,62]. The vasculature was selected by thresholding. Based on binary images, microvascular diameters were calculated by BoneJ software.

3.3 Results

3.3.1 High-resolution UTE-MRA

Figure 3.3 shows two normal volume-rendered rat brains acquired from high-resolution UTE-MRAs. Before administration of SPION, no cerebral veins are visible in the dorsal view (Figure 3.3(A)). In contrast, major arteries composing and contributing to the circle of Willis are visible in the ventral view (Figure 3.3(B), red arrows). In lateral views (Figure 3.3(C), red arrow), ascending MCAs are visible. No vessels are visible in the anterior-to-posterior view (Figure 3.3(D)). UTE-MRA before administration of SPION is a TOF-MRA, which shows large arteries populating the brain surface region. After administration of SPION, not only major arteries but also veins (including DCV, IPTGV, and cRHV) are visible in the dorsal (Figure 3.3(E), red arrow), ventral (Figure 3.3(F), red arrow), and lateral views (Figure 3.3(G), red arrows). In the anterior-to-posterior view (Figure 3.3(H)), intracortical penetrating and other macro-vessels are shown.

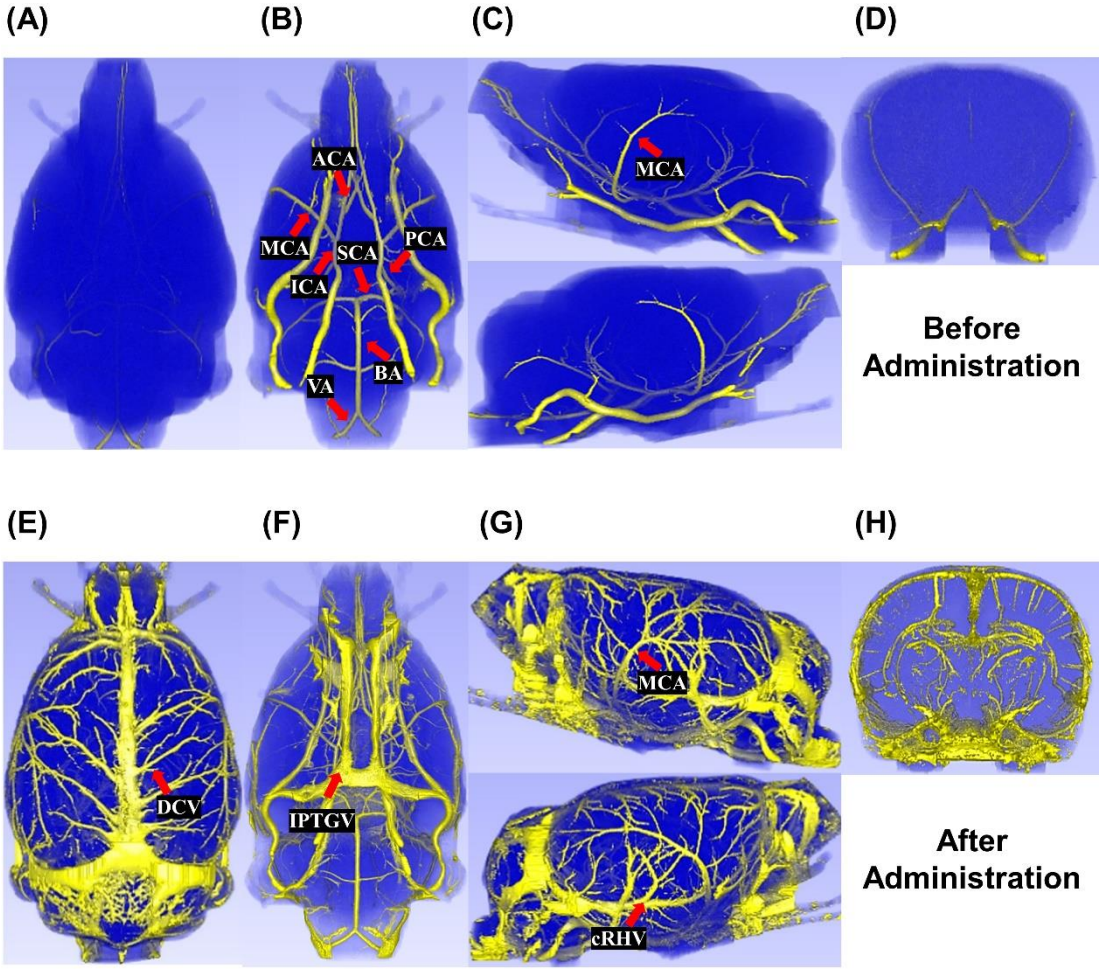

Figure 3.3 UTE-MRAs of two normal rat brain. Dorsal views (A and E), ventral views (B and F), lateral views (C and G) and anterior-to-posterior views (D and H) of UTE-MRAs acquired before and after administration of SPION, respectively. Red arrows indicate middle cerebral artery (MCA), posterior

cerebral artery (PCA), internal carotid artery (ICA), anterior cerebral artery (ACA), superior cerebellar artery (SCA), vertebral artery (VA), basilar artery (BA), dorsal cerebral vein (DCV), interpterygoid emissary vein (IPTGV), and caudal rhinal vein (cRHV).

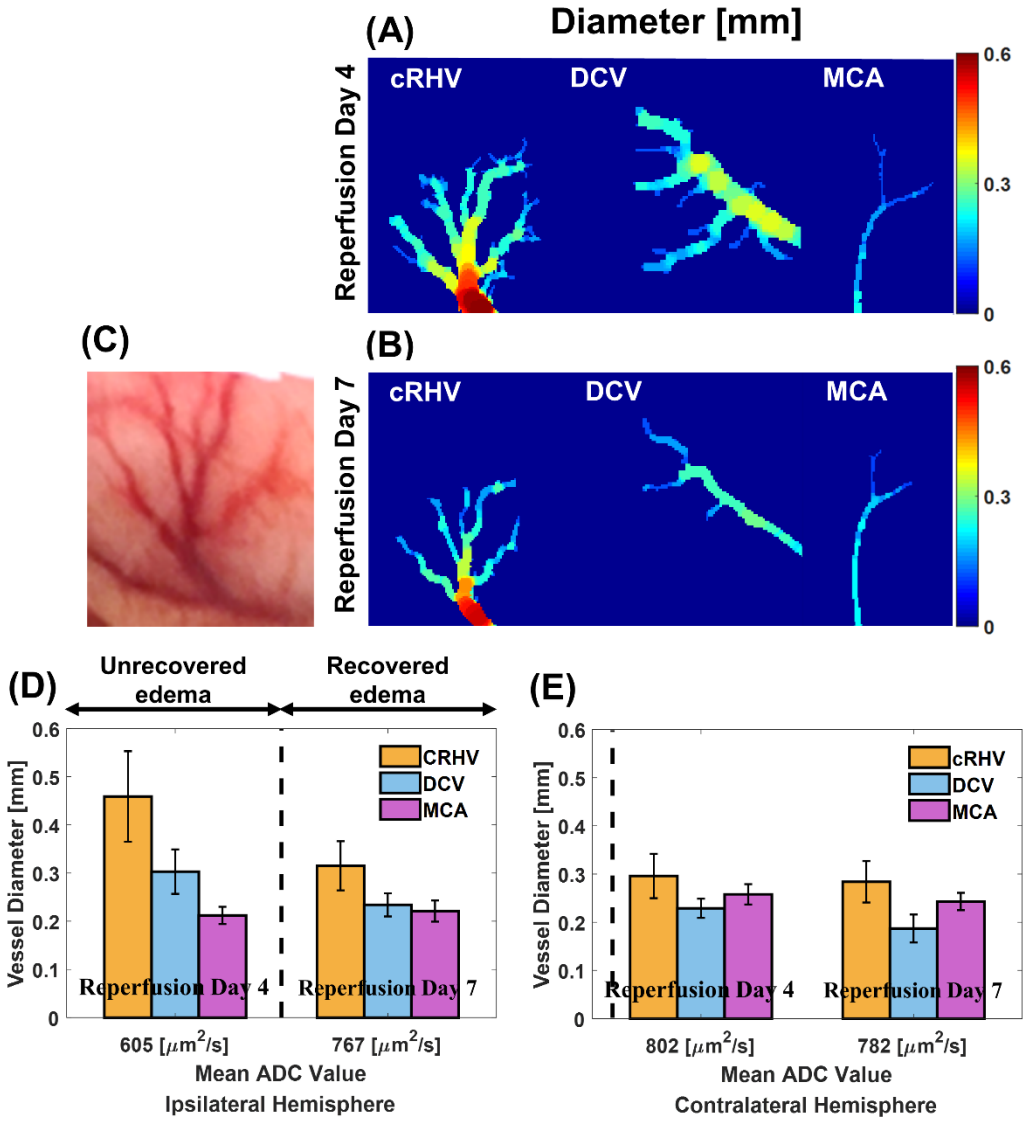

Figure 3.4 Macrovascular remodeling of tMCAO rat brain. The results of diameter fittings of cRHV, DCV and MCA in ipsilateral hemisphere at reperfusion day 4 (A) and at reperfusion day 7 (B). Corresponding snapshot of cRHV at reperfusion day 7 (C). The mean value of fitted sphere diameters of the main branch was set as respective vessel diameter. Vessel diameters of cRHV (orange), DCV (blue), and MCA (purple) of the ipsilateral hemisphere with respect to mean ADC values of the corresponding cortical lesion at reperfusion days 4 and 7 (D). Vessel diameters of cRHV (orange), DCV (blue), and MCA (purple) of the contralateral hemisphere with respect to mean ADC values of the corresponding cortical region at reperfusion days 4 and 7 (E). The dotted vertical lines mark the ADC = 650 μm^2/s, which are set to separate ischemic edema from recovered/normal tissue.

To directly visualize alterations of macrovasculature in ipsilateral hemisphere of UTE-MRAs, vessel diameter maps of cRHV, DCV and MCA in the ipsilateral hemisphere at reperfusion day 4 and day 7 are shown in Figures 3.4(A) and (B). As the illustrations for morphological changes of macrovasculature in the tMCAO model, longitudinally acquired UTE-MRAs and ADC maps of re-perfused tMCAO rat brains are fully shown in Figure 3.5. Bar graphs show mean ADC values of cortical regions along with the diameters of cRHV, DCV, and MCA in the ipsilateral and contralateral hemispheres at reperfusion day 4 (ischemic edema in the ipsilateral brain) and at reperfusion day 7 (recovered ischemic edema in the ipsilateral brain) as shown in Figures 3.4(D) and (E), respectively. Only the main branches of vasculatures were used to calculate mean vessel diameter to minimize measurement errors. A significant dilation of the pial venous vessels in the ipsilateral region is evident at reperfusion day 4 and reduced to normal diameters at reperfusion day 7, followed by recovery of the corresponding mean ADC value as shown in Figure 3.4(D). A snapshot of the corresponding cRHV is shown in Figure 3.4(C) at reperfusion day 7 as a reference for direct comparison with UTE-MRA. No significant variations were observed for both cRHV and DCV in the contralateral brain (Figure 3.4(E)). As shown in Figures 3.4(D) and (E), the MCA thinned at reperfusion day 4 was restored to its normal diameter at reperfusion day 7 when compared to that of the contralateral brain.

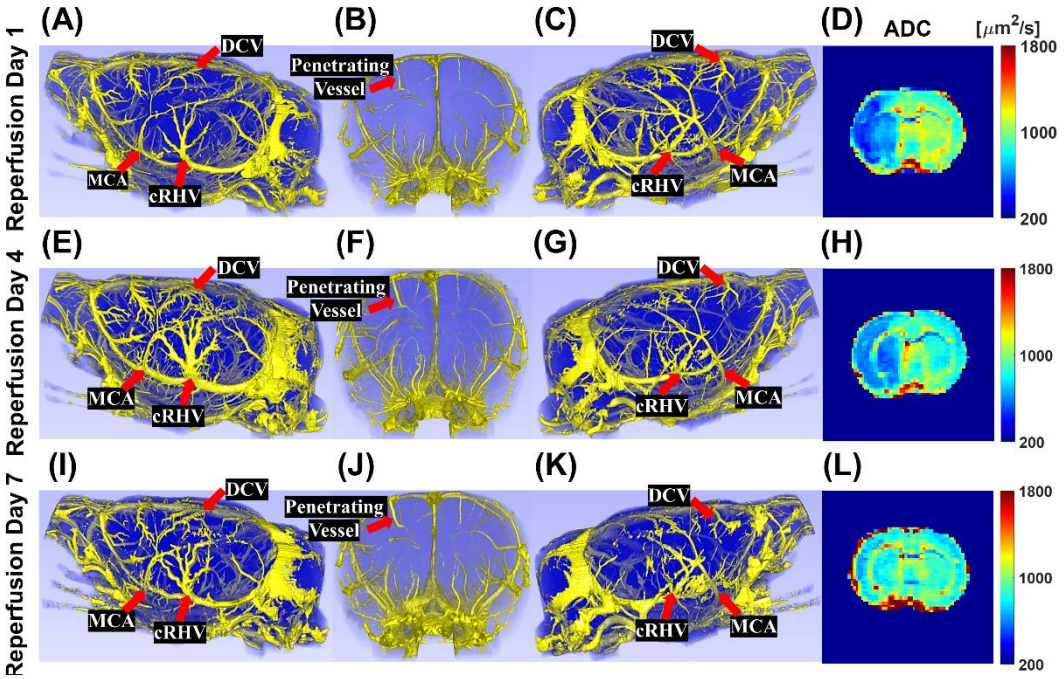

Figure 3.5 Macrovascular remodeling of tMCAO rat brain. Lateral views of ipsilateral hemisphere (A, E, and I), anterior-to-posterior views (B, F, and J) and lateral views of contralateral hemisphere (C, G, and K) of UTE-MRAs and ADC maps (D, H, and L) acquired at reperfusion days 1, 4, and 7, respectively.

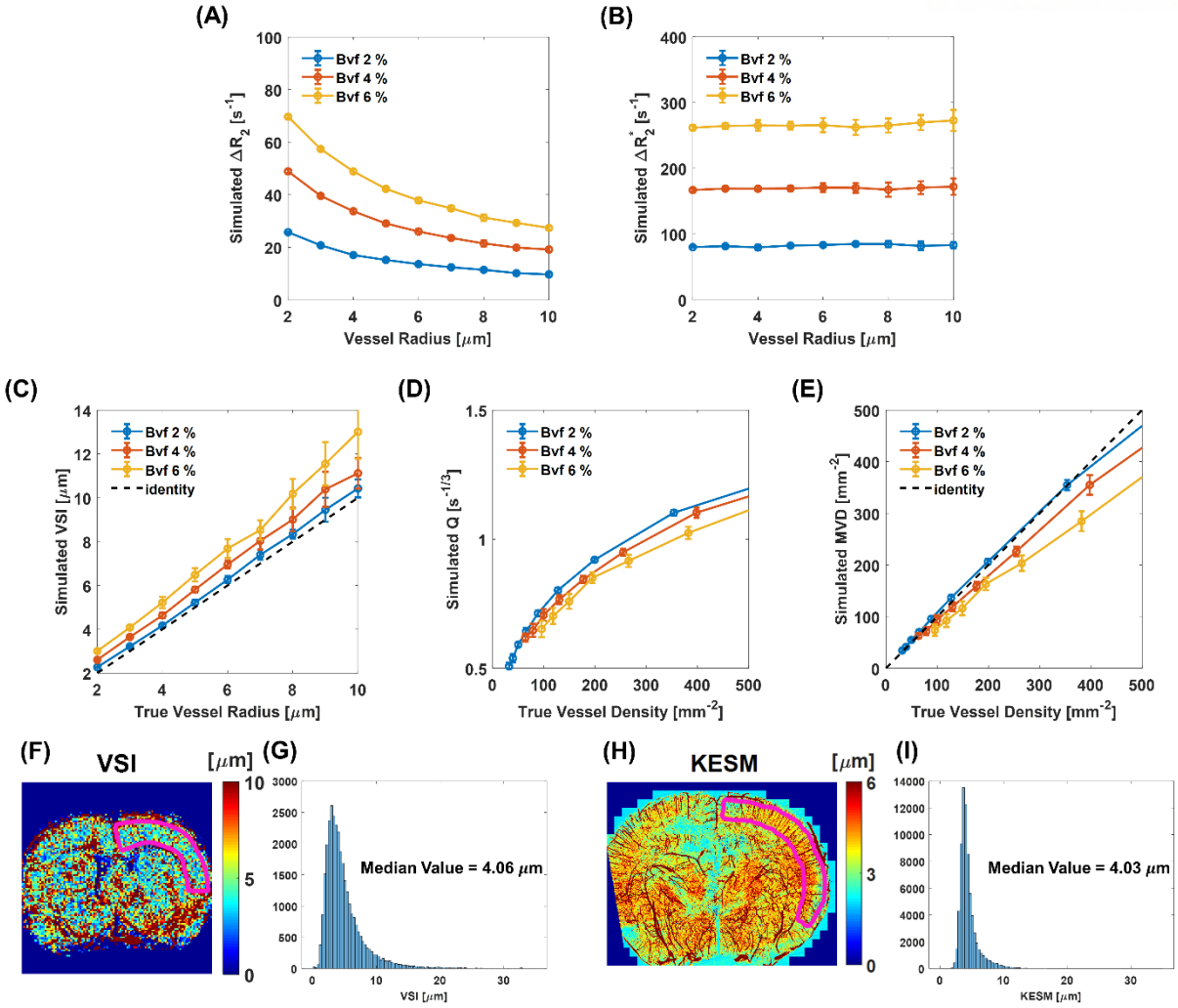

Figure 3.6 Monte Carlo simulation results. Vessel radius and blood volume fraction (Bvf) dependent simulated ΔR_2 (A) and ΔR_2^*(B). Comparison of simulated VSI with true vessel radius (C). Comparisons of simulated Q and MVD with true vessel density (D and E, respectively). Experimental VSI map (F) and distribution (G) in the cortical region (ROI, marked with purple line in F). Corresponding gold-stand vessel size map (H) and distribution (I) in cortical region from knife-edge scanning microscope (ROI, marked with purple line in H).

3.3.2 ΔR_2-ΔR_2^*-MRI

Vessel radius and Bvf-dependent ΔR_2 and ΔR_2^* values from the Monte Carlo simulation are shown at 7-T with experimental SPION dose and MRI parameters in Figures 3.6(A) and (B), respectively. As vessel radius increased, simulated ΔR_2 values decreased while simulated ΔR_2^* values were approximately constant in all Bvf conditions. Also, as Bvf increased, simulated ΔR_2 and ΔR_2^* values increased in the same vessel radius condition. Simulated VSI (Figure 3.6(C)) showed insignificant dependency on Bvf and increased as a function of the input vessel radius. Simulated Q and MVD values

increased as a function of input vessel density, irrespective of Bvf (Figures 3.6(D) and (E)). Experimental VSI values distribution in the cortical region (ROI was shown in Figure 3.6(F)) is shown in Figure 3.6(G). In direct comparison, the gold-standard vessel size distribution of the cortical region (ROI was shown in Figure 3.6(H)) from KESM is shown in Figure 3.6(I) and shows a consistent long-tail toward larger values distribution with respect to the experimental VSI values distribution. Median values of VSI and KESM are 4.06 μm and 4.03 μm, respectively. Although fitted echo trains showed low ΔR_2 values [13], those values showed less fluctuation compared to ΔR_2 values from the first echo (Figure 3.7). ΔR_2 values (~20 s^{-1}) from simulated (Bvf 2%, radii 2-4 μm) and the first echo of MSME acquisition were consistent as shown in Figure 3.7. For VSI/Q/MVD calculation, robust ΔR_2 maps obtained from fitted echo trains were multiplied by factor of 4.375 (determined from experiments) and used for VSI/Q/MVD input to be consistent with simulations.

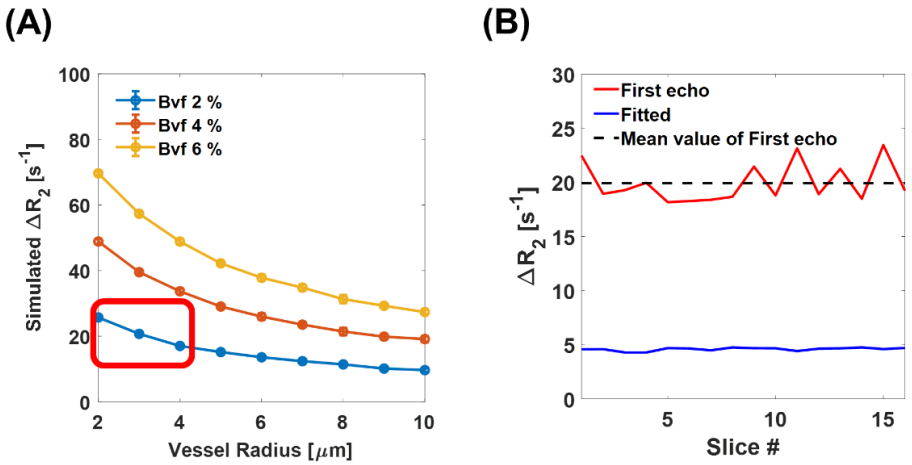

Figure 3.7 ΔR_2 value calibration. Simulated ΔR_2 values (A, red box) and corresponding values obtained from the first echo of MSME acquisition were consistent (B, red line). The ΔR_2 values obtained from the fitted echo trains of MSME acquisition (B, blue line). The ratio between ΔR_2 values first echo and fitted echo trains was 4.375 and this ratio was calibrated for VSI/Q/MVD calculation.

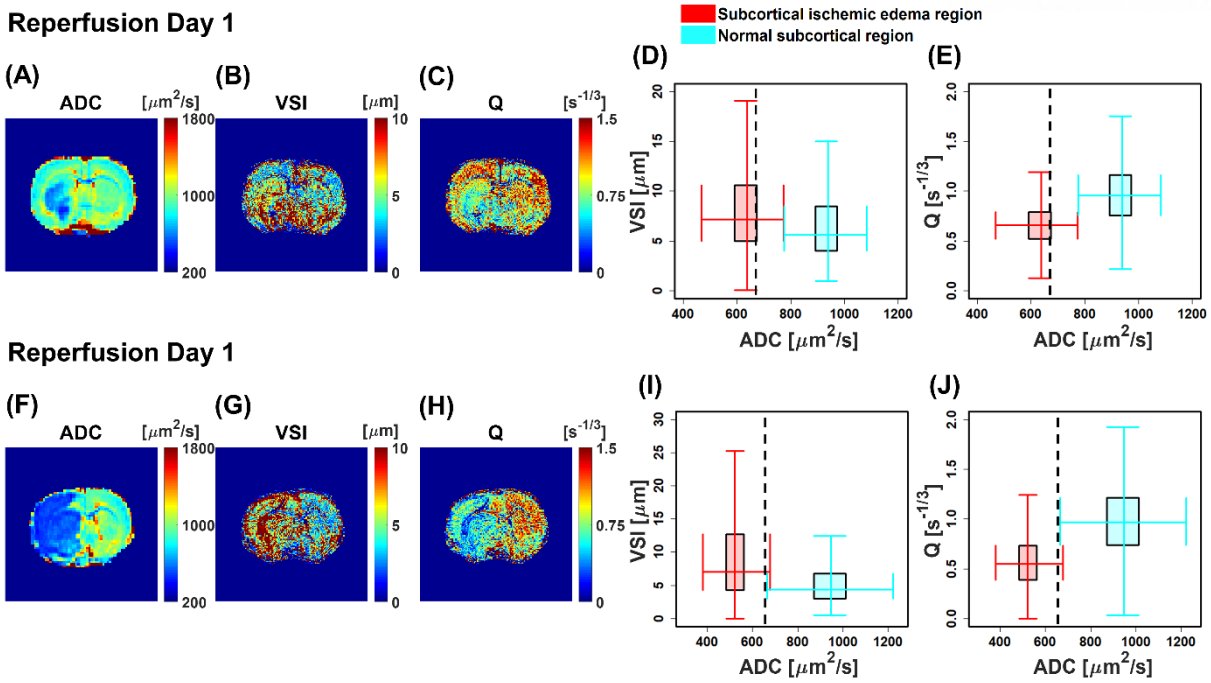

Figure 3.8 Microvascular remodeling of two tMCAO rat brains. ADC maps (A and F), VSI maps (B and G), and Q maps (C and H) of two tMCAO rat brains at reperfusion day 1. Double box plots between VSI values and corresponding ADC values of subcortex for both rats (D and I). Double box plots between Q values and corresponding ADC values of subcortex for both rats (E and J). The dotted vertical lines mark the ADC = 650 μm^2/s, which are set to separate ischemic edema from normal tissue.

As the illustrations for morphological changes of microvasculature in the tMCAO model, ADC, VSI, and Q maps of two tMCAO rat brains acquired at early reperfusion day (day 1) are shown in Figure 3.8. The two tMCAO rat brains show different ischemic edema size in the ipsilateral hemisphere of the ADC maps (Figures 3.8(A) and (F)). In each ipsilateral ischemic edema lesion, the corresponding VSI map showed increased VSI values than the corresponding region in the contralateral hemisphere (Figures 3.8(B) and (G)). In contrast, each Q map showed lower values compared to those of the corresponding region in the contralateral hemisphere (Figures 3.8(C) and (H)). The location of abnormal ADC, VSI, and Q values appeared to be strongly co-localized. Double box plots (VSI versus ADC and Q versus ADC) verified increased VSI values and decreased Q values in the subcortical ischemic edema lesions (ADC_{mean} < 650 μm^2/s) of the ipsilateral side compared with those of the contralateral side (Figures 3.8(D), (E), (I), and (J)).

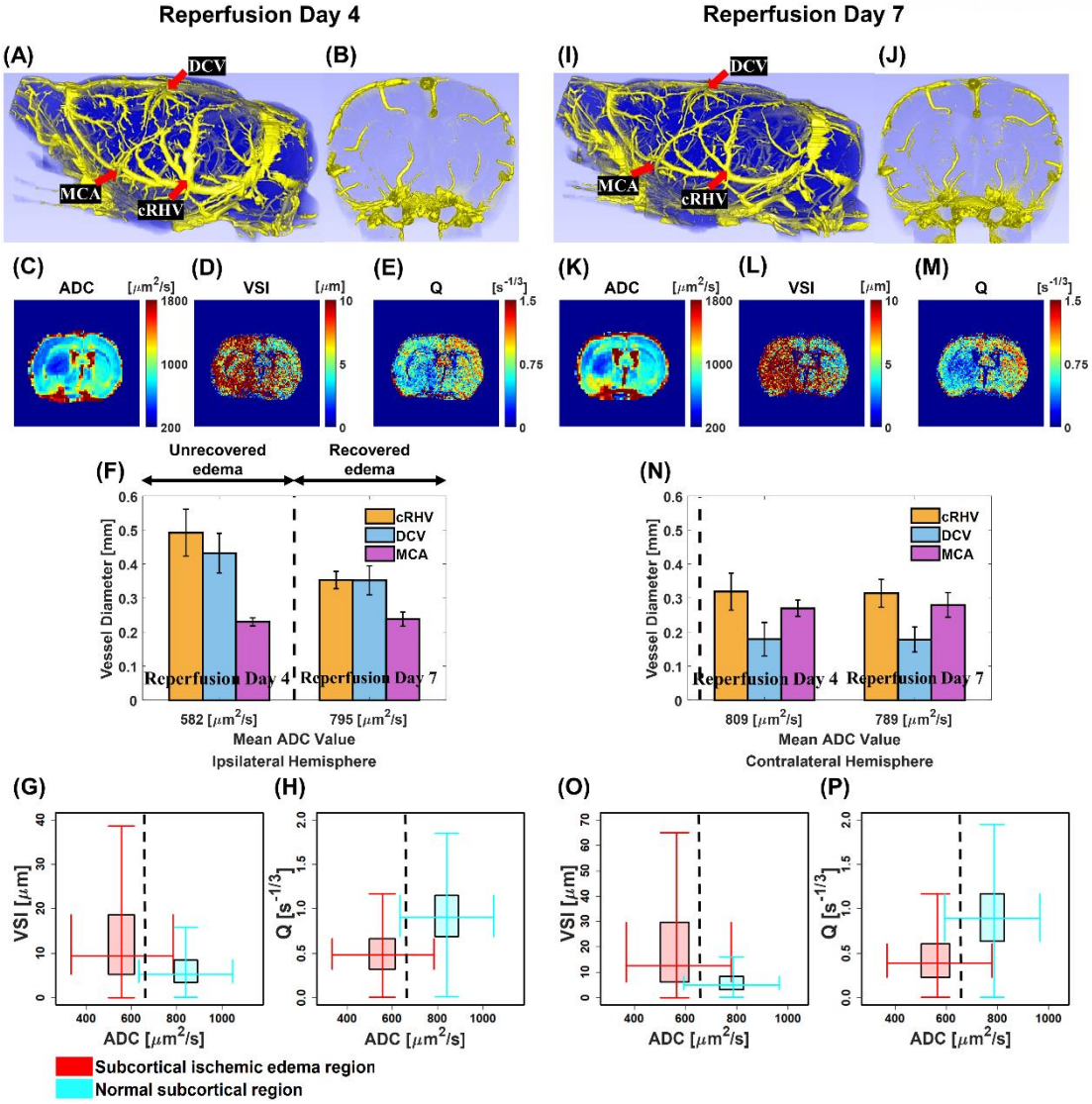

Figure 3.9 Macro- and microvascular remodeling of tMCAO rat brain. Lateral views of ipsilateral hemisphere (A and I) and anterior-to-posterior views (B and J) of tMCAO rat brain UTE-MRAs and corresponding ADC maps (C and K), VSI maps (D and L), and Q maps (E and M) of tMCAO rat brain acquired at reperfusion days 4 and 7, respectively. Vessel diameters of cRHV (orange), DCV (blue), and MCA (purple) of the ipsilateral hemisphere with respect to mean ADC values of the corresponding cortical lesion at reperfusion days 4 and 7 (F). Vessel diameters of cRHV (orange), DCV (blue), and MCA (purple) of the contralateral hemisphere with respect to mean ADC values of the corresponding cortical region at reperfusion days 4 and 7 (N). Double box plots between VSI values and corresponding ADC values of subcortex (G and O) for reperfusion days 4 and 7, respectively. Double box plots between Q values and corresponding ADC values of subcortex (H and P) for reperfusion days 4 and 7, respectively. The dotted vertical lines mark the ADC = 650 $\mu m^2/s$, which are set to separate ischemic edema from recovered/normal tissue.

3.3.3 Dual contrast MRI

Longitudinal dual contrast MRI results, which reflected macro- and microvascular remodeling in tMCAO rat models, are shown in Figures 3.9, 3.10, and 3.11. Even though each tMCAO rat model showed heterogeneous evolution after reperfusion, distinct vascular size alterations and density reductions at early reperfusion days (day 1~day 4) were consistently observed in the area of ipsilateral ischemic edema. After such alterations, morphological normalization of the pial vessels and microvessels was observed to be associated with the recovery of respective ADC values in the cerebral cortex and subcortex at late reperfusion day (day 7).

First, this tMCAO rat model demonstrates the necessity of whole-brain simultaneous mapping of the macro- and microvasculature after ischemic stroke. UTE-MRAs, ADC, VSI, and Q maps are shown in Figures 3.9(A), (B), (C), (D), (E), (I), (J), (K), (L), and (M). As reperfusion continued from day 4 to day 7, enlarged cRHV and DCV in the lateral view of ipsilateral hemisphere became thinner in UTE-MRAs (Figures 3.9(A) and (I), red arrows). The corresponding ADC values in the cortical ischemic edema region increased, while those of the subcortical ischemic edema region did not significantly change, as shown in Figures 3.9(C) and (K). In other words, high-resolution UTE-MRAs were insufficient to explain the observed persistence of ischemic edema in the subcortical region. In contrast, increased VSI and decreased Q values in the subcortical ischemic edema region (abnormal microvascular remodeling) were observed, as shown in Figures 3.9(D), (E), (L), and (M); this explains the persistence of edema in the corresponding region. Figures 3.9(B) and (J) show brain inner regions of UTE-MRAs as the same slice position and thickness with VSI/Q maps. Abnormality of vessels in subcortical ischemic edema region is more distinctly visible in VSI/Q maps compared to brain inner region of UTE-MRA at reperfusion day 7 (Figures 3.9(J), (L), and (M)).

In the cortical area, bar graphs show the diameter changes of cRHV, DCV, and MCA located in the ipsilateral (Figure 3.9(F)) and contralateral (Figure 3.9(N)) hemisphere at day 4 (ischemic edema (ADC_{mean} < 650 $\mu m^2/s$) in cortex and subcortex) and day 7 (ischemic edema in subcortex only) after reperfusion. The mean ADC values of each cortex are also shown. A significant dilation of pial venous vessels (cRHV and DCV) in the ipsilateral area is evident at reperfusion day 4, decreased to the normal diameter at reperfusion day 7, and corresponding mean ADC value at reperfusion day 7 was restored. The reduced diameter of MCA in the ipsilateral side at reperfusion day 4 was normalized at reperfusion day 7. In the subcortical area, double box plots show increased VSI and decreased Q values in ipsilateral ischemic edema lesions compared to those of in the contralateral region at both 4 and 7 days after reperfusion (Figures 3.9(G), (H), (O), and (P)). Thus, persisting microvascular changes were observed along with non-recovering ADC values in subcortical ischemic edema region regardless of normal macrovascular remodeling in the cortical ischemic edema region.

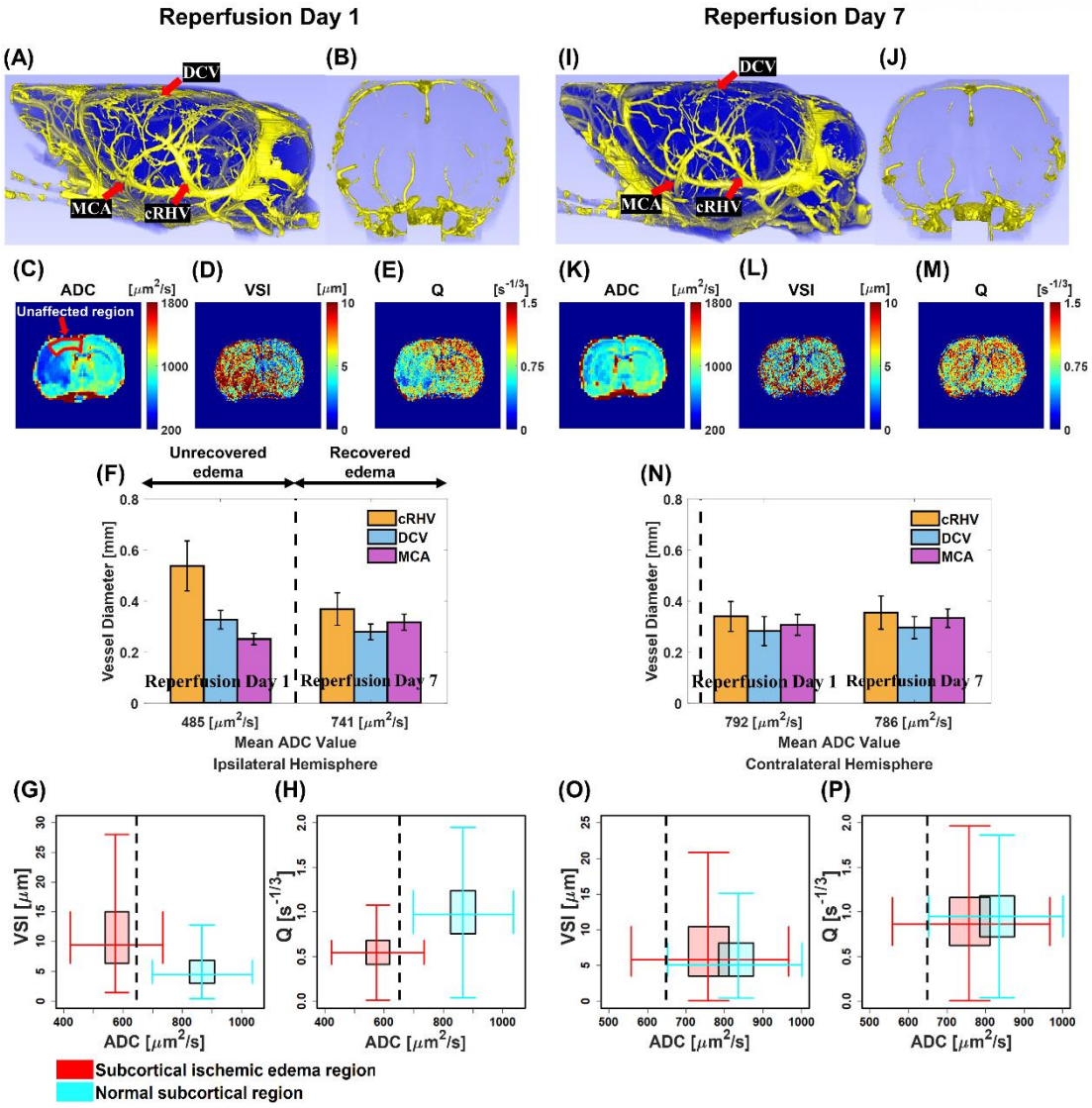

Figure 3.10 Macro- and microvascular remodeling of tMCAO rat brain. Lateral views of ipsilateral hemisphere (A and I) and anterior-to-posterior views (B and J) of tMCAO rat brain UTE-MRAs and corresponding ADC maps (C and K), VSI maps (D and L), and Q maps (E and M) of tMCAO rat brain acquired at reperfusion days 1 and 7, respectively. Vessel diameters of cRHV (orange), DCV (blue), and MCA (purple) of the ipsilateral hemisphere with respect to mean ADC values of the corresponding cortical lesion at reperfusion days 1 and 7 (F). Vessel diameters of cRHV (orange), DCV (blue), and MCA (purple) of the contralateral hemisphere with respect to mean ADC values of the corresponding cortical region at reperfusion days 1 and 7 (N). Double box plots between VSI values and corresponding ADC values of subcortex (G and O) for reperfusion days 1 and 7, respectively. Double box plots between Q values and corresponding ADC values of subcortex (H and P) for reperfusion days 1 and 7, respectively. The dotted vertical lines mark the ADC = 650 μm^2/s, which are set to separate ischemic edema from recovered/normal tissue.

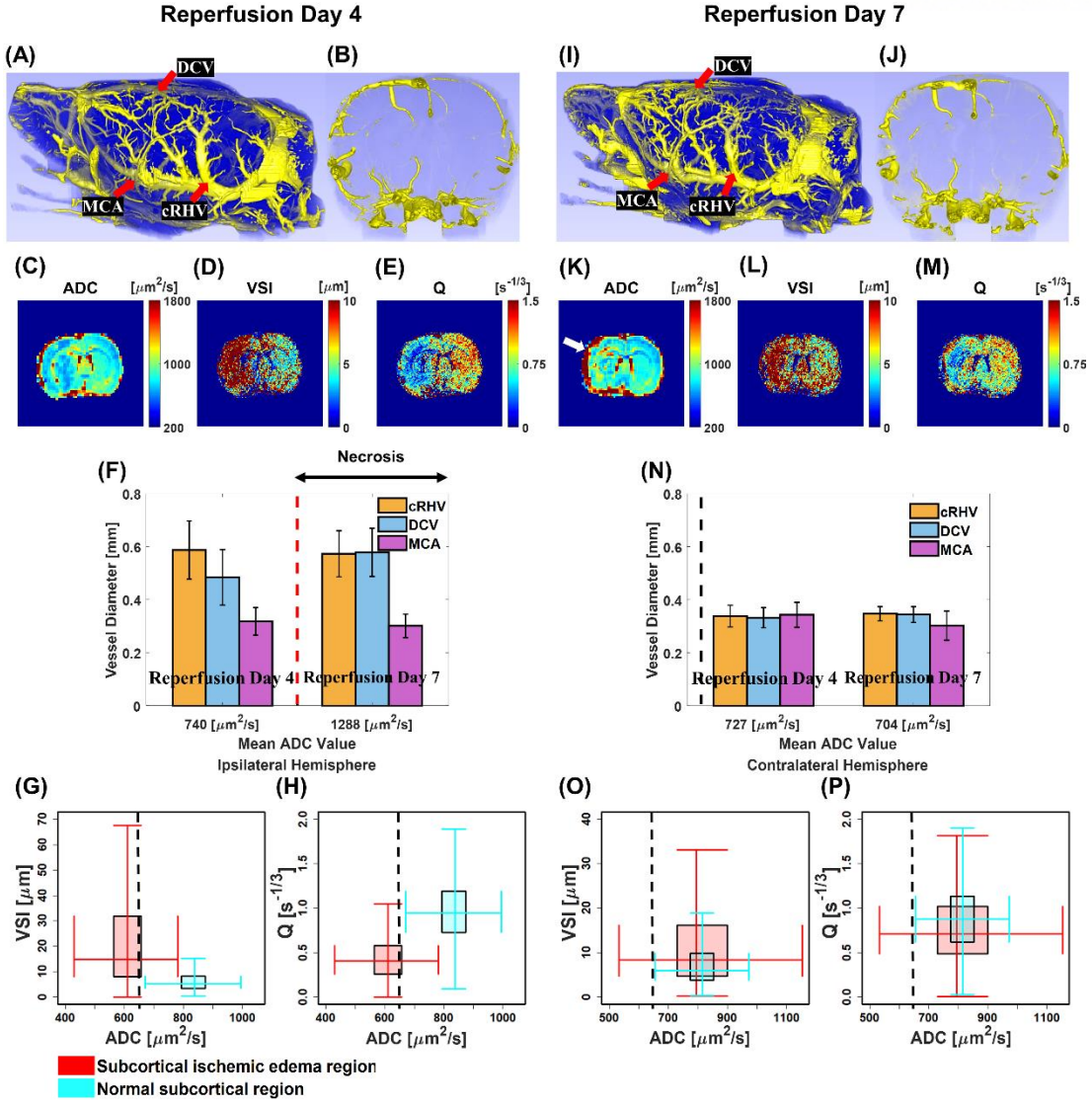

Figure 3.11 Macro- and microvascular remodeling of tMCAO rat brain. Lateral views of ipsilateral hemisphere (A and I) and anterior-to-posterior views (B and J) of tMCAO rat brain UTE-MRAs and corresponding ADC maps (C and K), VSI maps (D and L), and Q maps (E and M) of tMCAO rat brain acquired at reperfusion days 4 and 7, respectively. Vessel diameters of cRHV (orange), DCV (blue), and MCA (purple) of the ipsilateral hemisphere with respect to mean ADC values of the corresponding cortical lesion at reperfusion days 4 and 7 (F). Vessel diameters of cRHV (orange), DCV (blue), and MCA (purple) of the contralateral hemisphere with respect to mean ADC values of the corresponding cortical region at reperfusion days 4 and 7 (N). Double box plots between VSI values and corresponding ADC values of subcortex (G and O) for reperfusion days 4 and 7, respectively. Double box plots between Q values and corresponding ADC values of subcortex (H and P) for reperfusion days 4 and 7, respectively. The black dotted vertical lines mark the ADC = 650 μm²/s, which are set to separate ischemic edema from recovered/normal tissue. The red dotted vertical line separates recovered tissue

from necrotic tissue.

Second, we show a case of normal recovery of both cortical and subcortical lesions after reperfusion and explain the association of morphological vascular normalizations with ADC values. UTE-MRAs showed normal thinning of a dilated cRHV and DCV in lateral views of the ipsilateral hemisphere as reperfusion continued from day 1 to day 7 (Figures 3.10(A) and (I), red arrows). Corresponding cortical ADC values in the ischemic edema region increased as reperfusion continued from day 1 to day 7 (Figures 3.10(C) and (K)). Consistently, VSI values in the ischemic edema lesion decreased and Q values increased and returned to normal range, comparable to those of the contralateral hemisphere at reperfusion day 7 (Figures 3.10(D), (E), (L), and (M)). Subcortical ADC values in the ischemic edema region also increased to the normal range as reperfusion continued from day 1 to day 7 as well (Figures 3.10(C) and (K)).

In the cortical area, bar graphs show mean ADC values along with the diameters of cRHV, DCV, and MCA located in the ipsilateral (Figure 3.10(F)) and contralateral (Figure 3.10(N)) hemisphere at day 1 (ischemic edema in cortex and subcortex) and day 7 (recovered ischemic edema in ipsilateral brain) after reperfusion, respectively. A significant dilation of cRHV in the ipsilateral area was evident at reperfusion day 1, decreased to the normal diameter at reperfusion day 7, and corresponding ADC value at reperfusion day 7 was restored. On the other hand, DCV showed unimpressive variations, consistent with the fact that no significant ADC reduction was observed upper cortical region marked by a red arrow in Figure 3.10(C). The reduction of MCA diameter in the ipsilateral side at reperfusion day 1 was normalized at reperfusion day 7. In the subcortical area, double box plots show increased VSI values (Figure 3.10(G)) and reduced Q values (Figure 3.10(H)) in ipsilateral ischemic edema lesion compared to those in the contralateral region at reperfusion day 1. However, the VSI (Figure 3.10(O)) and Q (Figure 3.10(P)) values in ipsilateral lesion became similar to those of the contralateral region at reperfusion day 7. Corresponding ADC values in the subcortical ischemic edema region were restored.

The third case shows that abnormal macrovascular remodeling of the pial venous vessels is associated with tissue necrosis progression from cortical ischemic edema. In UTE-MRAs, increased cRHV and DCV diameters are visible in lateral view of the ipsilateral hemisphere at reperfusion day 4 (Figure 3.11(A), red arrows). However, no significant diameter change of those vessels is observable between reperfusion days 4 and 7 (Figures 3.11(A) and (I), red arrows). Markedly elevated ADC values of the cortical area at reperfusion day 7 (Figure 3.11(K), white arrow) indicate the possible occurrence of necrosis. At reperfusion day 13, greater increase and expansion of those elevated ADC values were observed (Figure 3.12), which further verifies the tissue necrosis.

However, in the subcortical region, decreased VSI values and increased Q values as reperfusion continued from day 4 to day 7 were observed, indicating a normal microvascular recovery in the

corresponding region with normal ADC values (Figures 3.11(D), (E), (K), (L), and (M)). Bar graphs show the diameters of cRHV, DCV and MCA for ipsilateral (Figure 3.11(F)) and contralateral (Figure 3.11(N)) hemisphere at day 4 and day 7 after reperfusion with mean ADC values of cortical regions. A significant dilation of the pial venous vessels in the ipsilateral area is evident from reperfusion day 4 to reperfusion day 7. Thereafter, necrosis proceeded in the cortex. In the subcortical area, double box plots show increased VSI values (Figure 3.11(G)) and reduced Q values (Figure 3.11(H)) in ipsilateral ischemic edema lesion at reperfusion day 4. However, the VSI (Figure 3.11(O)) and Q (Figure 3.11(P)) values of ipsilateral lesion became comparable to those values of the contralateral region at reperfusion day 7, and the recovery of the corresponding ADC values in subcortex followed. Thus, in the cortical area, sustained macrovascular dilation was observed regardless of normal microvascular remodeling in the subcortex. The need for dual contrast MR imaging is again emphasized in order to simultaneously investigate heterogeneous macro- and microvascular remodeling in ischemic stroke associated with the progression of ischemic edema.

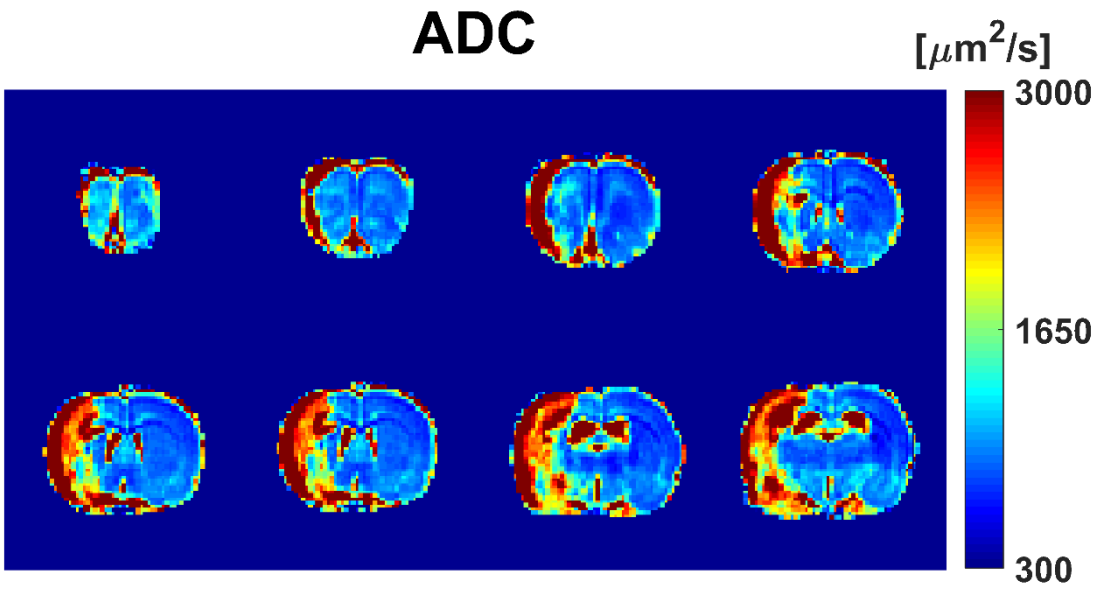

Figure 3.12 ADC maps of tMCAO rat brain acquired at reperfusion day 13 (same tMCAO rat model as in Figure 3.11).

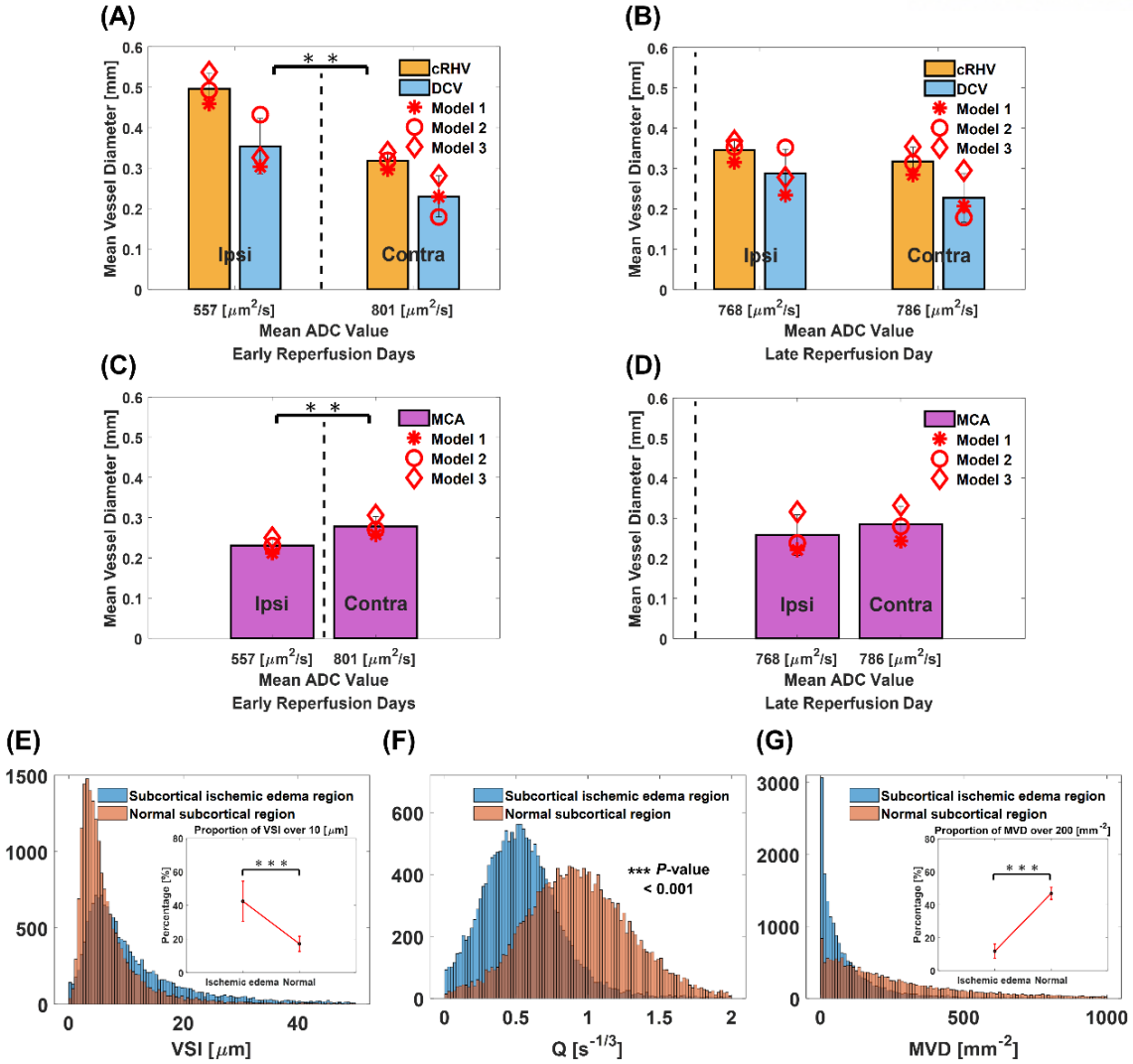

Figure 3.13 Statistical analysis of macro- and microvascular remodeling. Mean vessel diameters of combined maximum cRHVs and DCVs diameters at early days (from day 1 to day 4) of reperfusion (A, three tMCAO rat models marked with star, circle, and diamond symbols). Mean vessel diameters of combined cRHVs and DCVs at reperfusion day 7 (B, three tMCAO rat models marked with star, circle, and diamond symbols). Mean vessel diameter of combined minimum MCAs at early days (from day 1 to day 4) of reperfusion (C, three tMCAO rat models marked with star, circle, and diamond symbols). Mean vessel diameter of combined MCAs at reperfusion day 7 (D, three tMCAO rat models marked with star, circle, and diamond symbols). Corresponding mean ADC values of the cortex were shown. Combined VSI values versus ADC values (six cases for ischemic edema and eight cases for recovered/normal cases were summarized) in ischemic edema and normal regions of subcortex (E). Corresponding histograms of VSI values in ischemic edema and normal regions of subcortex (H). The proportions of larger VSI values (> 10 μm) in ischemic edema and normal regions of subcortex are respectively shown in the inset figure of H. Combined Q and MVD values versus ADC values in

ischemic edema and normal regions of subcortex (F and G), respectively. Corresponding histograms of Q and MVD values in ischemic edema and normal regions of subcortex (I and J). The proportions of larger MVD values (> 200 mm^{-2}) in ischemic edema and normal regions of subcortex are respectively shown in the inset figure of J. *** ($p<0.001$) and ** ($p<0.01$) from Student's t-test. The dotted vertical lines mark the ADC = 650 $\mu m^2/s$, which are set to separate ischemic edema from recovered/normal tissue.

3.3.4 Macro- and microvascular remodeling analysis

14In the cortex, the maximum vessel diameters of cRHV and DCV and the minimum vessel diameter of MCA in the ipsilateral brain were respectively combined at early reperfusion days (day 1 and day 4), except for the case of cortical necrosis progression. Consistently, the vessel diameters of normalizing cRHV, DCV, and MCA in the ipsilateral brain were respectively combined at late reperfusion day (day 7). Corresponding vessel diameters of the contralateral region were also combined, accordingly. Then, the association between mean ADC values of cortical regions and morphological alteration of pial venous and arterial vessels from UTE-MRAs were observed. Mean diameters of venous cRHVs and DCVs were significantly ($p = 0.0051$, paired Student's t-test with combined cRHV and DCV diameters) dilated in the lesions of ischemic edema at early reperfusion days and then normalized at late reperfusion day with the restoration of corresponding ADC values as shown in Figures 3.13(A) and (B), respectively. On the contrary, the mean diameter of arterial MCAs was significantly ($p = 0.0096$, paired Student's t-test) thinned at early reperfusion days and then recovered at late reperfusion day as shown in Figures 3.13(C) and (D), respectively.

In the subcortex, the VSI/Q/MVD values in ischemic edema lesions ($ADC_{mean} < 650\ \mu m^2/s$) and those values in normal tissue of contralateral hemisphere ($ADC_{mean} > 650\ \mu m^2/s$, recovered ipsilateral area included) were also respectively combined for all cases. Then, the association between ADC values and VSI/Q/MVD values from ΔR_2-ΔR_2^*-MRI was also revealed. The VSI values showed a non-Gaussian distribution with a long tail toward larger values as shown in Figure 3.13(E). Compared with normal tissues, VSI values in ischemic edema lesions showed wider distribution with significantly ($p < 0.001$, unpaired Student's t-test) increasing relative proportion of larger vessels (VSI > 10 μm). The proportion of small vessels (VSI < 10 μm) was observed to be relatively reduced. The Q values of ischemic edema lesions were significantly ($p < 0.001$, unpaired Student's t-test) smaller than those of values in the normal areas as shown in Figure 3.13(F). MVD values in ischemic edema lesions showed narrower distribution with significantly ($p < 0.001$, unpaired Student's t-test) reduced relative proportion of larger vessel densities (MVD > 200 mm^{-2}) as shown in Figure 3.13(G).

3.4 Discussion and conclusions

To quantitatively evaluate macro- and microvascular remodeling after ischemic stroke, we performed dual contrast MRI on tMCAO rat models. To estimate of association of vascular remodeling with ischemic edema status, ADC maps were also acquired, which quantitatively represent ischemic tissue status [63-65]. T_1-contrast-based UTE-MRAs visualized morphological alterations of the macrovasculature occurring at the tMCAO rat brain surface region at an isotropic resolution of 59 μm^3. In response to MCA occlusion, dilated pial venous vessels (cRHV and DCV) were clearly observed at early reperfusion days (1 to 4 days) as collateral circulatory role likely to accommodate thinned MCA, reflecting the early phase of venous macrovascular dilation. After this dilation, reduced venous vessel diameters were visible (7 days after reperfusion), which correlated with the restoration of ADC values. In contrast, thinned pial arterial vessel (MCA) was observed at early reperfusion days and restored at late reperfusion day (7 days). Because MCA was occluded initially, it is likely that the size of MCA was observed to be reduced even at early days of reperfusion and gradually recovered along with ADC recovery. Our observations on the different morphological response of pial arterial and venous vessels during the ischemic edema recovery would still require further investigations for physiological origins.

At the same time, the utilization of VSI/Q/MVD maps, which were derived from ΔR_2-ΔR_2^*-MRI, verified morphological alterations of the microvasculature occurring at the tMCAO rat brain inner region. As a comparison of our VSI/Q/MVD values with other previous validation studies, cortical regions of contralateral hemispheres for all tMCAO rat models were segmented and combined. Such median values of VSI/Q/MVD from all tMCAO rat models were 4.06 μm, 1.07 $s^{-1/3}$, and 337.4 mm^{-2}, respectively. Those values are quantitatively consistent with other validation reports [13,46,66]. Consistent with macrovascular remodeling, comparison VSI/Q/MVD values with subcortical ischemic edema status revealed an increased proportion of larger VSI values in the subcortical ischemic edema lesions. Also, reduced Q and proportion of larger MVD values were observed in the subcortical ischemic edema lesions, which are qualitatively consistent with other reports [44,47,67]. Microvascular normalization was observed at late reperfusion day (day7) as well. On the other hand, simultaneous morphological characterization of macro- and microvasculature showed a significant spatial variation of vascular changes. In some cases, even when cortical macrovascular remodeling was normal, subcortical microvascular remodeling was observed to correlate with unrestored ischemic edema and vice versa. The importance of such whole-brain monitoring of the cerebral vasculature and their association with ischemic recovery in multiple length-scales is illustrated in ischemic stroke brains.

It is also important to note that morphological changes of venous vessels in the post-ischemic stroke brain were rarely reported before. Considering the fact venous macrovascular dilations were observed

from UTE-MRAs in early reperfusion days, and that the venous cerebral volume fraction reaches 70% in the rodent brain [68], observed changes of VSI/Q/MVD values may be partially attributed to changes in venous microvasculature in subcortex area as well. Because the ischemic edema (via the ADC) is observed to be significantly associated with changes in MR-derived morphological (size and density) macro- and microvasculature, multi-length vascular information, including venous vasculature may help optimize the drug or treatment strategy after ischemic stroke. However, further quantification of sole venous microvascular information in the ischemic brain ideally requires a technical ability to differentiate morphologically changes in the arterial and venous systems of the microvascular system.

The difference in the distribution of VSI values between the subcortical ischemic edema lesion and the normal region is informative. In our Monte Carlo simulation, each VSI, Q, and MVD value was calculated from a single microvessel radius condition. However, in real cerebrovascular systems, various vascular radiuses may co-exist, which may complicate direct interpretation of MR-derived microvascular parameters. For example, in Monte Carlo simulation, reduction of relatively small vessels or actual dilation of all vessels may provide similarly increased VSI values. Also, if distributions of relatively small and large vessels are reduced in similar proportions, VSI values may not change. In this case, Q and MVD values should provide complementary information. Experimentally, a significant decrease in the Q and MVD values in ischemic edema lesions observed with changes in the VSI distribution supports the hypothesis that a number of small vessels decreases and a number of large vessels increases in the ischemic edema lesions. To establish the effectiveness of MRI-derived microvascular remodeling data for analyzing ischemic stroke progression, a validation study with microvessel size distributions may be required, using proven techniques from the previous studies [46,48,69].

This study also suggests areas for possible technical improvements. First, as the current method enables sequential acquisition of perfusion parameters from DSC-MRI as well, combining diffusion and vascular morphological and functional information may provide a more complete picture of ischemic stroke progression, requiring further optimization of acquisition protocols. Second, high-resolution dual contrast MRI requires relatively long scan times, which hampers its routine application yet. For reduction of scan time, adjusting resolution with MR parameters that can affect scan time is necessary. There are several techniques, such as compressed sensing [70], parallel imaging [71], and super-resolution reconstruction via deep learning [72,73], that can additionally reduce scan time. Further study is required to verify the effectiveness of those techniques for clinical application of dual contrast MRI.

In summary, dual contrast MRI with SPION as a single contrast agent can be successfully performed on rat models of tMCAO to simultaneously visualize whole brain macro- and microvascular remodeling

after ischemic stroke, including pial venous vessels. Visualization and quantification of such simultaneous macro- and microvascular remodeling indicated that MR-based morphological (size and density) vessel normalization is directly associated with restored ADC values in post-ischemic stroke rat brains. Multiscale monitoring of the cerebrovascular system with dual contrast MRI may further elucidate the vascular mechanism of ischemic stroke recovery.

The original source of Chapter 3 is the article, Kang, M.; Jin, S.; Lee, D.; Cho, H., MRI Visualization of Whole Brain Macro-and Microvascular Remodeling in a Rat Model of ischemic Stroke: A pilot Study. *Scientific reports* **2020,** *10* (1), 1-12.

Chapter 4. Dual contrast MRI: Application

4.1 Introduction

Following an ischemic stroke, multiple neurologic complications, including cerebral edema, inflammation, and vascular alteration, develop dynamically during the subacute stage (1 to 7 days). As the status of the subacute stage affects the progression of the chronic stage, a detailed investigation of the subacute stage of ischemic stroke is crucial. For example, pseudo-normalization of the magnetic resonance (MR) apparent diffusion coefficient (ADC) values is typically observed around one week after ischemic stroke [74-78]. This is most likely due to a combination of cytotoxic edema (lowering ADC, swelling of cells) and the development of vasogenic edema (increasing ADC, swelling of the extracellular space) [79-83]. On the other hand, the temporal occurrence of such pseudo-normalization of the ADC may be spatially heterogeneous in ischemic brains [84,85]. If vasogenic edema occurs faster in certain ischemic areas, an accelerated pseudo-normalization of the ADC develops, and these lesions more quickly and widely expand into the chronic stage. As a result, detailed spatial characterization and diagnosis of early and typical ADC pseudo-normalization lesions and subsequent treatment decisions may be important [80,86-88]. However, since these early pseudo-normalization lesions have a higher ADC (closer to ADC of normal tissue) than typical pseudo-normalization lesions in the early subacute stage (1 to 4 days), distinguishing these lesions by ADC alone can be problematic, especially in the subacute stage.

Ischemic stroke is induced by cerebrovascular dysfunction and results in vascular remodeling. The visualization and quantification of the macro- and microvascular status may help characterize and differentiate early and typical pseudo-normalization lesions. Previous MR imaging (MRI) investigations of vascular remodeling have revealed a correlation between adequate vascular remodeling, recovery, and clinical outcomes after ischemic strokes [27,30,32,35]. However, differential MRI characterizations of both vascular morphology and function between early and typical pseudo-normalization lesions are rare in the subacute stage. Consequently, simultaneous longitudinal visualization and quantification of morphological (size/density) and functional (perfusion) vascular status in both lesions can provide further insights and prognostic information in addition to general measurements of lesion tissue status via the ADC or T_2. For example, the segmentation of ischemic lesions may elucidate the origins of hyperperfusion and delayed transit time observed in the subacute stage by cross-monitoring vascular morphology and function.

As an investigation of vascular alterations after ischemic stroke, MR angiography (MRA) has shown morphological macrovascular remodeling at the brain surface region after ischemic stroke [36,37,39]. Microvascular remodeling in the inner brain region can be visualized by morphological mapping of the

vessel size index (VSI) and microvessel density (MVD and Q), overcoming the spatial resolution limitation of MRA [44-48,89]. Dynamic susceptibility contrast MRI (DSC-MRI) can be used to estimate functional microvascular status, such as the cerebral blood volume (CBV), cerebral blood flow (CBF), and mean transit time (MTT) in lesions [90-92].

In this study, longitudinal morphological and functional vascular remodeling were investigated differentially between early and typical pseudo-normalization lesions to assess contrasting vascular conditions in a transient middle cerebral artery occlusion (tMCAO) rat model using dual contrast superparamagnetic iron oxide nanoparticles (SPION) [89]. Early and typical pseudo-normalization lesions were selected and segmented using longitudinally acquired ADC maps. Corresponding VSI and MVD maps were generated to evaluate the morphological vascular status. For evaluation of functional vascular status, relative CBV (rCBV), CBF (rCBF), and MTT (rMTT) maps from DSC-MRI acquisitions were simultaneously analyzed. Ultra-short echo time MRAs (UTE-MRAs) were acquired to compare morphological macrovascular remodeling occurring at the brain surface region. For the direct validation of VSI, MVD, and rCBV values between two lesions, light sheet fluorescence microscopy (LSFM) images of tMCAO rat models were acquired and quantitatively compared at reperfusion day 7.

4.2 Materials and methods

4.2.1 Animal preparation

Animal experiments were performed in accordance with the Animal Protection Act of Korea under a protocol approved by the Institutional Animal Care and Use Committee of the Ulsan National Institute of Science and Technology. All experiments were reported in compliance with the ARRIVE guidelines (Animal Research: Reporting In Vivo Experiments) [93]. Male Wistar rats (bodyweight 280-320 g, n = 13) were subjected to focal brain ischemia by transient occlusion of the middle cerebral artery (MCA). Initially, rats were anesthetized by inhalation of 3% isoflurane in a mixture of 70% nitrous oxide and 30% oxygen. Anesthesia was maintained by changing the range of isoflurane to 1-1.5%. Body temperature was kept constant (37 ± 1 ℃) through a feedback-controlled heating pad. As previously described [52], an intraluminal monofilament (0.37 mm diameter, Doccol Corporation, Redlands, CA, USA) was inserted into the external carotid artery and positioned to the internal carotid artery to block the MCA. The monofilament was withdrawn after 1 h of occlusion, and rats were housed in a 12 h light-12 h dark cycle with access to food and water *ad libitum*.

4.2.2 MRI acquisition

MRI acquisitions were conducted using a 7-T MR scanner (Bruker, Ettlingen, Germany). The tMCAO rat models were anesthetized using the same method of focal brain ischemia surgery. A single contrast agent, SPION, was synthesized in-house according to previously described methods [94]. The core size distribution of the iron oxide measured by transmission electron microscopy was 5-10 nm, and the mean hydrodynamic diameter of the iron oxide nanoparticles measured by differential light scattering was 20 ± 7 nm. The r_1 and r_2 of SPION were 2.36 $mM^{-1}s^{-1}$ and 32.94 $mM^{-1}s^{-1}$ at 7-T, respectively. SPION was administered as an intravenous bolus with a dose of 75 μmol Fe/Kg for DSC-MRI acquisition, and an additional SPION dose of 285 μmol Fe/Kg (total 360 μmol Fe/Kg) was administered for ΔR_2, ΔR_2^*, and UTE-MRA acquisitions. Longitudinal MRI acquisitions of tMCAO rat models were performed at reperfusion days 1, 4, and 7. Morphological and functional microvascular remodeling (VSI and MVD and DSC-MRI, respectively) were acquired for all (n = 11) tMCAO rat models, and macrovascular remodeling (UTE-MRA) was acquired for two representative tMCAO rat models showing early pseudo-normalization and typical pseudo-normalization in the cortex lesions.

The ADC map was acquired using a diffusion-weighted echo planar imaging (EPI) pulse sequence with the following parameters: TR/TE = 3500/26.6 ms, number of averages (NA) = 8, number of segments = 3, b-values = 100, 200, 400, 600, 800, and 1000 s/mm^2, flip angle (FA) = 90 °, matrix size = 100 × 100, field of view (FOV) = 30 × 30 mm^2, resolution = 300 × 300 μm^2, number of slices = 8, and slice thickness = 1 mm. Three directional (x, y, and z) ADC maps were acquired and averaged.

The DSC-MRI perfusion maps were acquired using a gradient-echo EPI pulse sequence with the following parameters: TR/TE = 420/17 ms, NA = 1, number of segments = 1, number of repetitions = 400, FA = 30 °, matrix size = 96 × 96, FOV = 30 × 30 mm^2, resolution = 313 × 313 μm^2, number of slices = 8, and slice thickness = 1 mm.

The ΔR_2 map was acquired using a multi-slice multi-echo pulse sequence with the following parameters: TR = 6000 ms, TE = 8-160 ms, echo spacing = 8 ms, NA =1, FA = 90 °, matrix size = 256 × 256, FOV = 30 × 30 mm^2, resolution = 117 × 117 μm^2, number of slices = 8, and slice thickness = 1 mm.

The ΔR_2^* map was acquired using a multi-echo gradient-echo pulse sequence with the following parameters: TR = 6000 ms, TE = 3-59 ms, echo spacing = 4 ms, NA = 1, FA = 90 °, matrix size = 256 × 256, FOV = 30 × 30 mm^2, resolution = 117 × 117 μm^2, number of slices = 8, and slice thickness = 1 mm.

The UTE-MRA was acquired using the UTE pulse sequence with the following parameters: TR/TE = 22/0.012 ms, NA = 1, FA = 40 °, under-sampling factor = 1.13, matrix size = 512 × 512 × 512, FOV = 30 × 30 × 30 mm^3, and resolution = 59 × 59 × 59 μm^3.

4.2.3 Fluorescence image acquisition

To label cerebral blood vessels, fluorescein isothiocyanate (FITC)-dextran solution was heart perfused in two representative tMCAO rat models, which showed early pseudo-normalization and typical pseudo-normalization in the cortex lesions at reperfusion day 7 according to the previously described methods [95]. One hundred milliliters of saline solution was administered into the left ventricle to extract cerebrovascular blood through the right atrium. Subsequently, FITC-dextran was mixed with 5% gelatin solution at a concentration of 0.075% and administered into the left ventricle. After 30 min of refrigeration, the rat brain was dissected and fixed in 4% paraformaldehyde (PFA) for two days. Then, 2 mm of the brain, including the edema lesion, was dissected. Tissue clearing was then performed to acquire 3-dimensional structural images using a Binaree tissue clearing™ kit (Cat. HRTC-001; Binaree, Korea). In brief, the tissue was immersed in the Binaree tissue clearing solution, which was changed every two to three days until the sample was visibly clear. The brains were transferred to Binaree Mounting and Storage™ Solution (Cat. SHMS-060, Binaree) for refractive index matching. Subsequently, using LSFM (Zeiss Lightsheet Z.1), 3-dimensional fluorescence images of tissue-cleared tMCAO rat brains were acquired with a resolution of $1.2 \times 1.2 \times 5.2\ \mu m^3$. In addition, 4% PFA fixed brains were embedded in OCT compound and dissected using a cryostat (Leica) at a thickness of 100 μm. Fluorescence images were acquired at a resolution of $0.8 \times 0.8\ \mu m^2$ using a fluorescence stereo zoom microscope (Zeiss Axio Zoom. V16) with a 38 Zeiss filter (excitation wavelength of 470 ± 40 nm and an emission wavelength of 525 ± 50 nm).

4.2.4 Data processing and analysis

MATLAB (MathWorks, Natick, MA) and ImageJ (US National Institutes of Health, Bethesda, MD) software were used for the data processing and analysis. Voxel-wise ADC values were estimated by fitting the equation $S = S_0 \times e^{-ADC \times b}$ with a nonlinear least-squares fitting method using MATLAB. b refers to the b-value for the corresponding MRI acquisition. Acquired ADC maps were up-sampled to a size of 256×256 for VSI and MVD calculations.

rCBV, rMTT, and rCBF maps were acquired using DSC-MRI. Initially, time-series signal intensity alteration due to SPION passage of each voxel was measured to calculate $\Delta R_2^*(t) = -\frac{1}{TE}\ln\left(\frac{S(t)}{S_{pre}}\right)$, where S_{pre} is an averaged signal before the administration of SPION. Subsequently, the area under the curve of $\Delta R_2^*(t)$ was measured after fitting $\Delta R_2^*(t)$ with the gamma-variate function to calculate the indices of rCBV, MTT, and rCBF using $rCBV_{index} = \int_0^t \Delta R_2^*(\tau)d\tau$, $MTT_{index} = \frac{\int_0^t \tau \Delta R_2^*(\tau)d\tau}{\int_0^t \Delta R_2^*(\tau)d\tau}$, $rCBF_{index} =$

$\frac{rCBV_{index}}{MTT_{index}}$ [96]. Finally, each rCBV, rMTT, and rCBF map was generated by dividing the index by the median value of the contralateral corpus callosum region indices for each tMCAO rat model.

The ΔR_2 and ΔR_2^* values were calculated by subtracting the transverse relaxation rate (R_2 and R_2^*) values acquired before the administration of SPION from the respective values acquired after the administration of SPION. The voxel-wise R_2 and R_2^* values were estimated by fitting the equation $S = S_0 \times e^{-TE \times [R_2 \text{ or } R_2^*]}$. ΔR_2 and ΔR_2^* maps were used to determine the VSI and MVD maps using the following equations [13,14]:

$$VSI\ (\mu m) = 0.424(ADC/(\gamma \Delta \chi B_0))^{1/2}(\Delta R_2^*/\Delta R_2)^{3/2} \quad (1)$$

$$MVD\ (mm^{-2}) \approx Q^3/(4.725ADC) \quad (2)$$

where γ is the proton gyromagnetic ratio, $\Delta\chi$ is the magnetic susceptibility difference between the vessel and tissue, and B_0 is the magnetic field strength. $\Delta\chi$ was estimated by $\Delta\chi = \frac{3\Delta R_2^*}{4\pi\, BVf\, \gamma\, B0}$, where BVf is the blood volume fraction. In addition, the microvessel density index Q was estimated by $Q\ (s^{-1/3}) = \Delta R_2/(\Delta R_2^*)^{2/3}$.

Acquired UTE-MRAs were denoised and visualized using 3D Slicer software (www.slicer.org) to investigate macrovascular remodeling in the tMCAO rat models [89]. The caudal rhinal veins (cRHVs), populated in the contralateral and ipsilateral regions for each representative tMCAO rat model, were selected and segmented for macrovascular remodeling. Vessel diameters of the segmented cRHVs were calculated using BoneJ software integrated with ImageJ [60]. In addition, the SD of each cRHV was derived.

Due to the DSC-MRI-derived rCBV maps' low spatial resolution, rCBV maps were replaced with high spatial resolution ΔR_2^* maps. The values of the ADC, T_2, VSI, MVD, CBV (ΔR_2^*), rCBF, and rMTT in early pseudo-normalization lesions, typical pseudo-normalization lesions, and contralateral regions were calculated and quantitatively evaluated. Subsequently, the relationship of vascular remodeling according to the status of cerebral edema was compared. A Mann-Whitney U test was performed to compare significant differences between early and typical pseudo-normalization lesions. To validate the difference in MRI-derived microvascular remodeling between early and typical pseudo-normalization lesions at reperfusion day 7, the vessel radius, vessel density, and blood volume fraction from the LSFM images were evaluated. The LSFM images were resized to an isotropic resolution of $1 \times 1 \times 1\ \mu m^3$. Three different regions of interest (ROIs) were selected for each early pseudo-normalization, typical pseudo-normalization lesions, and contralateral regions (total 12 ROIs). Then, the vessel radii were measured using BoneJ software with the same process as the vessel diameter calculation of UTE-MRA. The vessels in the segmented ROIs were counted using ImageJ software to calculate the vessel density.

4.3 Results

4.3.1 Early pseudo-normalization and typical pseudo-normalization lesions

Even though the pathogenesis of cerebral edema after ischemic stroke is complex, the underlying ADC dependence of early pseudo-normalization and typical pseudo-normalization lesions with associated vascular remodeling are conceptualized in Figure 4.1. To address the heterogeneity in the pseudo-normalization of ADC in ischemic lesions, two different edema progressions, marked by gold and green solid lines, are shown in Figure 4.1(A). The gold line shows the pseudo-normalization of ADC before reperfusion day 7 as marked by gold arrow (early pseudo-normalization), while the green line shows the pseudo-normalization of ADC at reperfusion day 7 as marked by green arrow (typical pseudo-normalization). The gold line shows a much higher ADC than the green line at reperfusion day 7. In Figure 4.1(B), the exemplar MRI-derived morphological VSI map and functional rCBF map are both visualized along with volume-rendered LSFM images, which were quantitatively analyzed and compared between the lesions of early and typical pseudo-normalization of ADC in the current study.

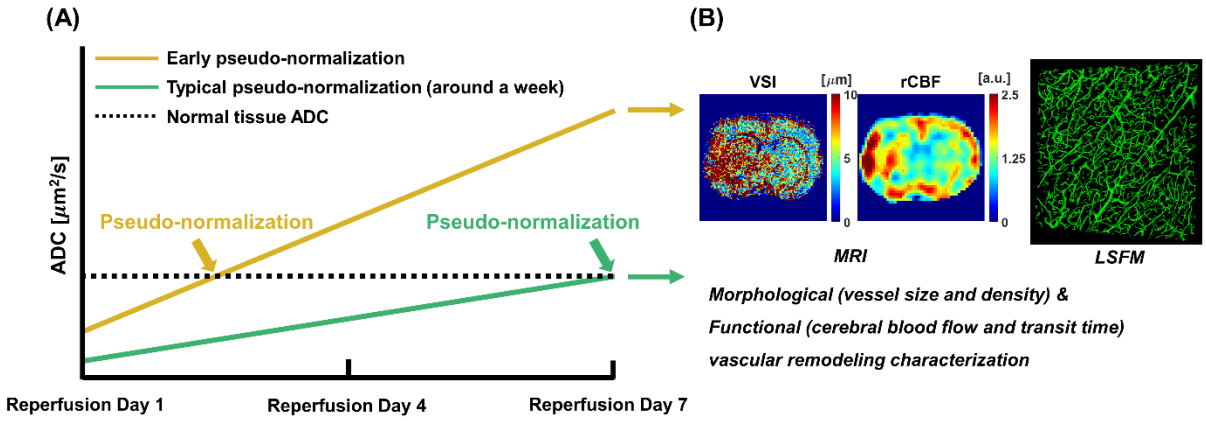

Figure 4.1 Conceptual illustration of edema progression in typical pseudo-normalization and early pseudo-normalization lesions. (A) ADC alterations in typical pseudo-normalization (green solid line) and early pseudo-normalization (gold solid line) lesions as reperfusion continued from day 1 to 7. The black dashed line indicates the ADC value of normal tissue. Two different time points of ADC pseudo-normalization in early and typical pseudo-normalization lesions are marked by gold and green arrows, respectively. (B) Exemplar MRI-derived morphological vascular remodeling related VSI map, functional vascular remodeling related rCBF map, and volume-rendered LSFM images to characterize vascular remodeling in typical pseudo-normalization and early pseudo-normalization lesions.

4.3.2 Morphological and functional microvascular remodeling mapping

Overall, Figure 4.2 shows longitudinally (reperfusion days 1, 4, and 7) acquired edema status surrogate (T_2 and ADC) maps with morphological (VSI and MVD) and functional (CBV, rCBF, and rMTT)

microvascular maps of a representative tMCAO rat model. At reperfusion day 1, the area of increased T_2 with decreased ADC indicates the edema lesion, as marked by yellow arrows in shown in Figures 4.2(A) and (B), respectively. Correspondingly, morphological (increased VSI and decreased MVD) and functional (reduced rCBF and elongated rMTT) microvascular variations are spatially matched with the corresponding edema lesion as shown in Figures 4.2(C), (D), (F), and (G), respectively. At reperfusion day 4, a slight decrease in T_2 and an increase in ADC values with respect to those values at reperfusion day 1 were observed, as shown in Figures 4.2(H) and (I), respectively. Along with such edema progression, spatially heterogeneous morphological and functional microvascular alterations are apparent (Figures 4.2(J), (K), (L), (M), and (N)). Specifically, there are conspicuous lesions marked by red arrows in Figures 4.2(H) and (I), which exhibit significantly increased T_2 and ADC. Such areas represent so-called early pseudo-normalization lesions. Even at reperfusion day 7, early pseudo-normalization lesions (ADC > 1500 $\mu m^2/s$ at reperfusion day 7) were observed with persistently enlarged VSI and reduced MVD values with respect to those values at reperfusion day 4, as shown in Figures 4.2(P), (Q), and (R). On the other hand, typical pseudo-normalization (ADC ~ 800 $\mu m^2/s$ at reperfusion day 7) tended to restore the morphological and functional microvascular parameters (except for rMTT), as shown in Figures 4.2(P), (Q), (R), (S), and (T).

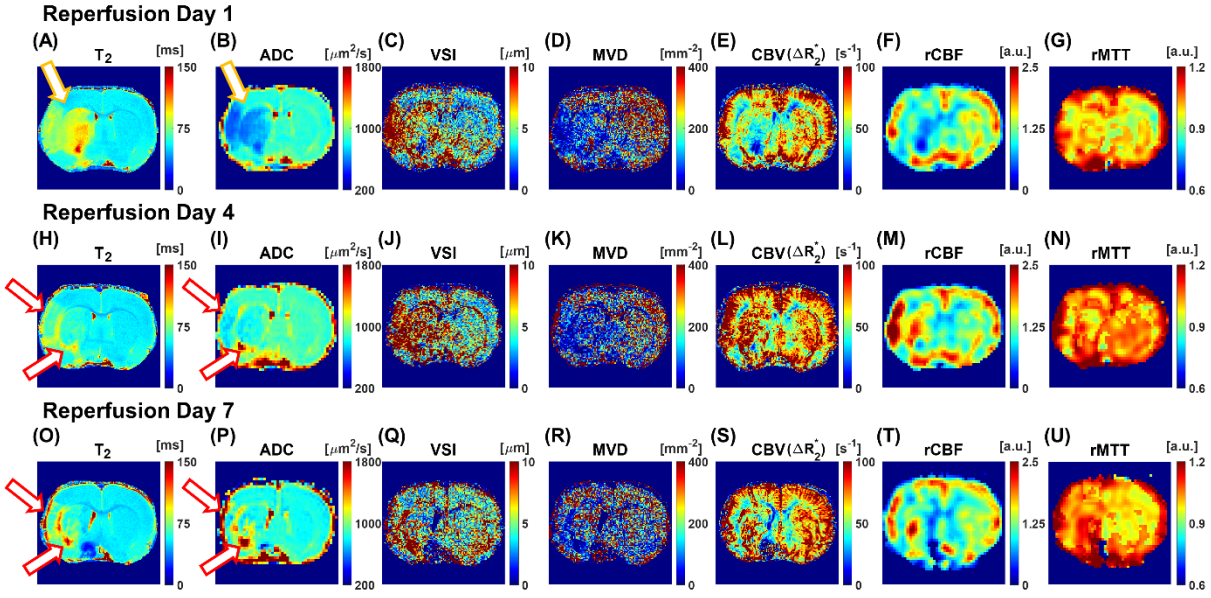

Figure 4.2 The representative lesion tissue status, as well as morphological and functional microvascular remodeling maps of one tMCAO rat model. (A-U) Longitudinally (at reperfusion days 1, 4, and 7) acquired lesion tissue status related T_2 and ADC maps, morphological microvascular remodeling related VSI and MVD maps, and functional microvascular remodeling related CBV, rCBF, and rMTT maps of one tMCAO rat model. The yellow arrows indicate edema lesion and red arrows

indicate early pseudo-normalization lesions.

4.3.3 ROI selection for early and typical pseudo-normalization lesions and the contralateral region

According to the ADC maps, typical pseudo-normalization, early pseudo-normalization lesions, and the contralateral region were selected and segmented, as shown in Figure 4.3. To cover whole-brain cerebral edema, three or four slices of each ADC map were used. At reperfusion day 1, ADC values under 650 $\mu m^2/s$ were considered as edema lesions and segmented as typical pseudo-normalization lesions, as indicated by the yellow boundary line in Figure 4.3(A). Then, the mirror region in the contralateral hemisphere was segmented as the contralateral region, as indicated by the green boundary line in Figure 4.3(A). Based on the segmented typical pseudo-normalization lesion and contralateral region at reperfusion day 1, the same ROIs were registered to the ADC maps of reperfusion days 4 and 7 and segmented (Figures 4.3(B) and (C)). In addition, vasogenic edema dominant and early pseudo-normalization lesions were selected and segmented. At reperfusion day 7, ADC values over 1500 $\mu m^2/s$ were considered as vasogenic edema dominant and segmented as early pseudo-normalization lesions, as indicated by the red boundary line in Figure 4.3(C). The ventricle regions show ADC values over 1500 $\mu m^2/s$ and if they are included in early pseudo-normalization lesions, they can induce bias to various vascular remodeling parameters. However, as accelerated vasogenic edema induced early pseudo-normalization lesions are structurally distinct from ventricle regions, the ventricle regions were not included in early pseudo-normalization lesions. Based on the segmented early pseudo-normalization lesion at reperfusion day 7, the same ROI was registered to the ADC maps of reperfusion days 1 and 4. From the mask of typical pseudo-normalization ROIs, the lesions of early pseudo-normalization ROIs were excluded for all reperfusion days. In addition, at each reperfusion day, the mirror region of the early pseudo-normalization lesion in the contralateral region was included as the contralateral region. All segmented ROIs were registered in DSC-MRI-derived perfusion maps as well.

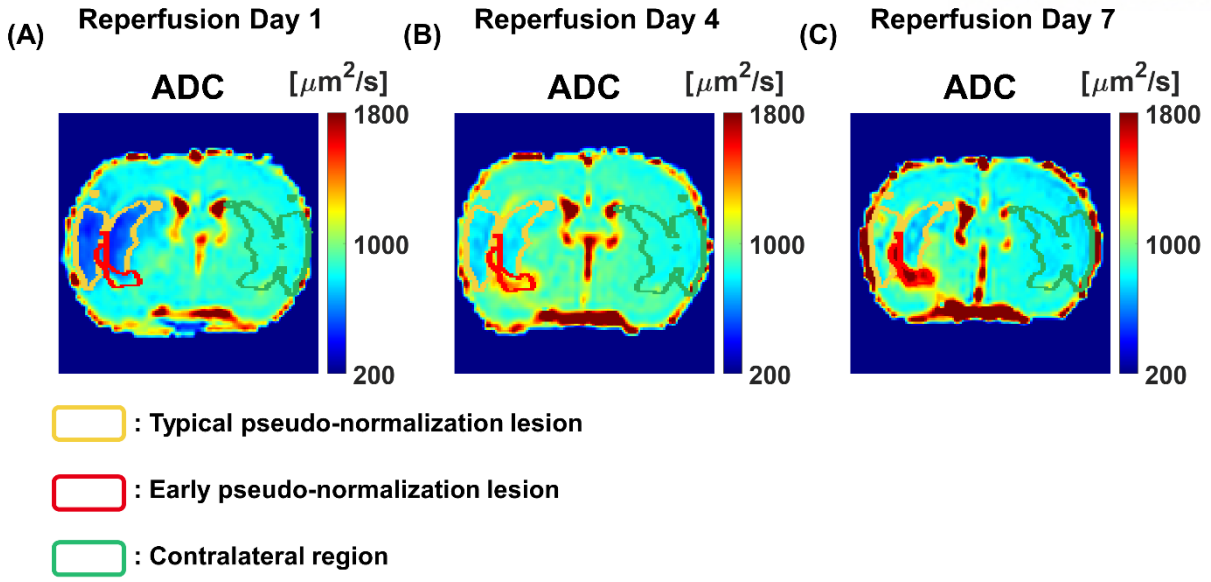

Figure 4.3 Respective ROIs for a typical pseudo-normalization lesion, early pseudo-normalization lesion, and contralateral region. (a-c) Selected ROIs for the typical pseudo-normalization lesion (yellow boundary lines, ADC < 650 $\mu m^2/s$ at reperfusion day 1), early pseudo-normalization lesion (red boundary lines, ADC > 1500 $\mu m^2/s$ at reperfusion day 7), and contralateral region (green boundary lines) at reperfusion day 1, 4, and 7. The contralateral region was selected as mirror regions of both typical and early pseudo-normalization lesions.

4.3.4 Comparisons of the morphological and functional microvascular remodeling

Next, a total of 33 cases of each of the ADC, T_2, and morphological and functional microvascular parameters were longitudinally (reperfusion day 1, 4, and 7) mapped for the 11 tMCAO rat models. Their median values were compared among the three ROIs, that is, typical and early pseudo-normalization lesions and the contralateral region. Figure 4.4 shows violin plots (distributions, median values, and interquartile ranges) of the edema status (ADC and T_2), as well as the morphological (VSI and MVD) and functional (CBV, rCBF, and rMTT) microvascular alterations of typical (blue) and early (red) pseudo-normalization lesions according to reperfusion days 1, 4, and 7. The median values are connected with dashed lines to evaluate the trend of vascular remodeling. In addition, the median values of the contralateral regions are connected with solid lines (orange) as reference values. In ADC, early pseudo-normalization lesions exhibited a median ADC value comparable to that of the contralateral region around reperfusion day 2, while typical pseudo-normalization lesions displayed it around reperfusion day 7 (Figure 4.4(A)). Elevated median T_2 values in typical and early pseudo-normalization lesions decreased over time (Figure 4.4(B)), except that early pseudo-normalization lesions showed

increasing median T_2 values as reperfusion continued from day 4 to 7. For morphological microvascular alterations, early pseudo-normalization lesions showed higher median VSI values than typical pseudo-normalization lesions at reperfusion days 4 and 7, while similar values were observed at reperfusion day 1 (Figure 4.4(C)). In addition, early pseudo-normalization lesion showed increased macrovascular diameter in UTE-MRAs compared to typical pseudo-normalization lesion as shown in Figure 4.5. In Figure 4.5(Q) and (R), the estimated cRHV diameters are shown as bar graphs. Both of the tMCAO rat models showed no significant alteration of cRHVs in the contralateral regions (orange) as reperfusion continued until day 7. In typical pseudo-normalization lesions, enlarged cRHV at reperfusion day 4 decreased at reperfusion day 7, indicating normalization of the macrovasculature (blue). However, in early pseudo-normalization lesions, enlarged cRHV at reperfusion day 4 did not significantly decrease at reperfusion day 7 compared to typical pseudo-normalization lesions (red). Early pseudo-normalization lesions showed lower median MVD values than typical pseudo-normalization lesions at all reperfusion days (Figure 4.4(D)). However, typical pseudo-normalization lesions showed increased median MVD values as reperfusion continued from day 4 to 7, while early pseudo-normalization lesions showed persistently lowered median MVD values. For functional microvascular alterations, early pseudo-normalization lesions showed higher median CBV and rCBF values than typical pseudo-normalization lesions at reperfusion days 4 and 7 (Figures 4.4(E) and (F), respectively). Early pseudo-normalization lesions showed higher median rMTT values than typical pseudo-normalization lesions at all reperfusion days (Figure 4.4(G)). As reperfusion continued from day 4 to 7, the median values of rMTT in early pseudo-normalization lesions became further elongated. For detailed distribution comparisons between typical pseudo-normalization lesions and contralateral regions, violin plots are shown in Figure 4.6. After Anderson-Darling tests for normal distribution decision, all Mann-Whitney U tests showed significant differences between typical pseudo-normalization and early pseudo-normalization lesions ($p < 0.01$) except for T_2 and VSI at reperfusion day 1 ($p = 0.371$ and $p = 0.947$, respectively).

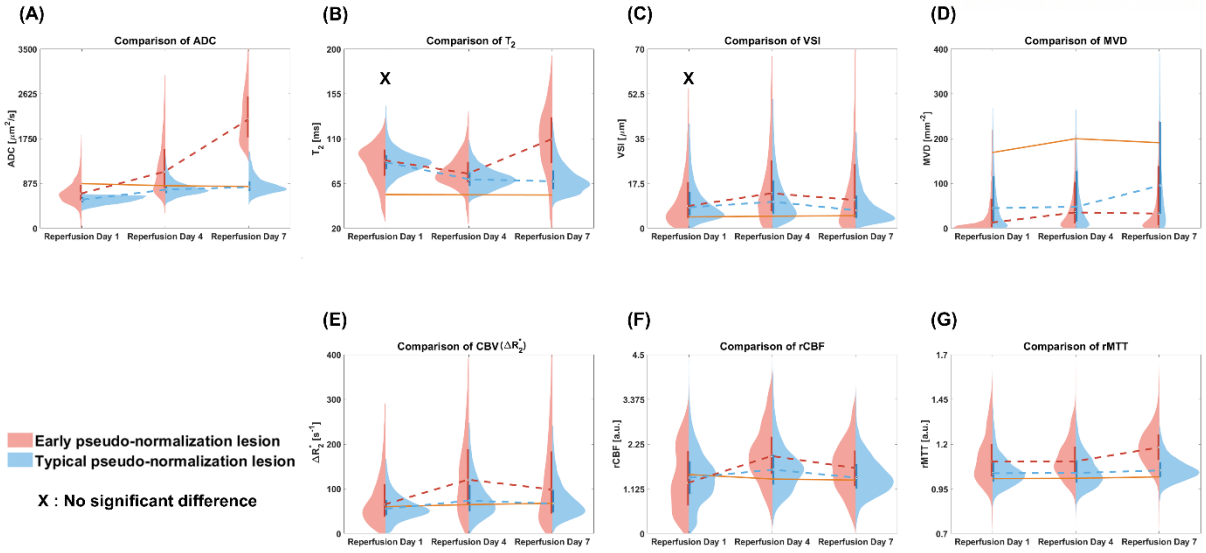

Figure 4.4 Violin plots of the lesion tissue status as well as morphological and functional microvascular remodeling. (A-G) Violin plots (distributions, median values, and interquartile ranges) of the lesion tissue status related ADC and T_2, morphological microvascular remodeling related VSI and MVD, and functional microvascular remodeling related CBV, rCBF, and rMTT in typical pseudo-normalization (blue) and early pseudo-normalization (red) lesions at reperfusion days 1, 4 and 7. The solid orange lines indicate the connected median values of the contralateral regions. The median values of each typical pseudo-normalization and early pseudo-normalization lesion were connected with dashed lines as reperfusion continued from days 1 to 7. The X marks indicate that no significant difference between typical and early pseudo-normalization lesions was found in the statistical analysis (T_2 and VSI at reperfusion day 1, $p = 0.371$ and $p = 0.947$ from the Mann-Whitney U tests, respectively).

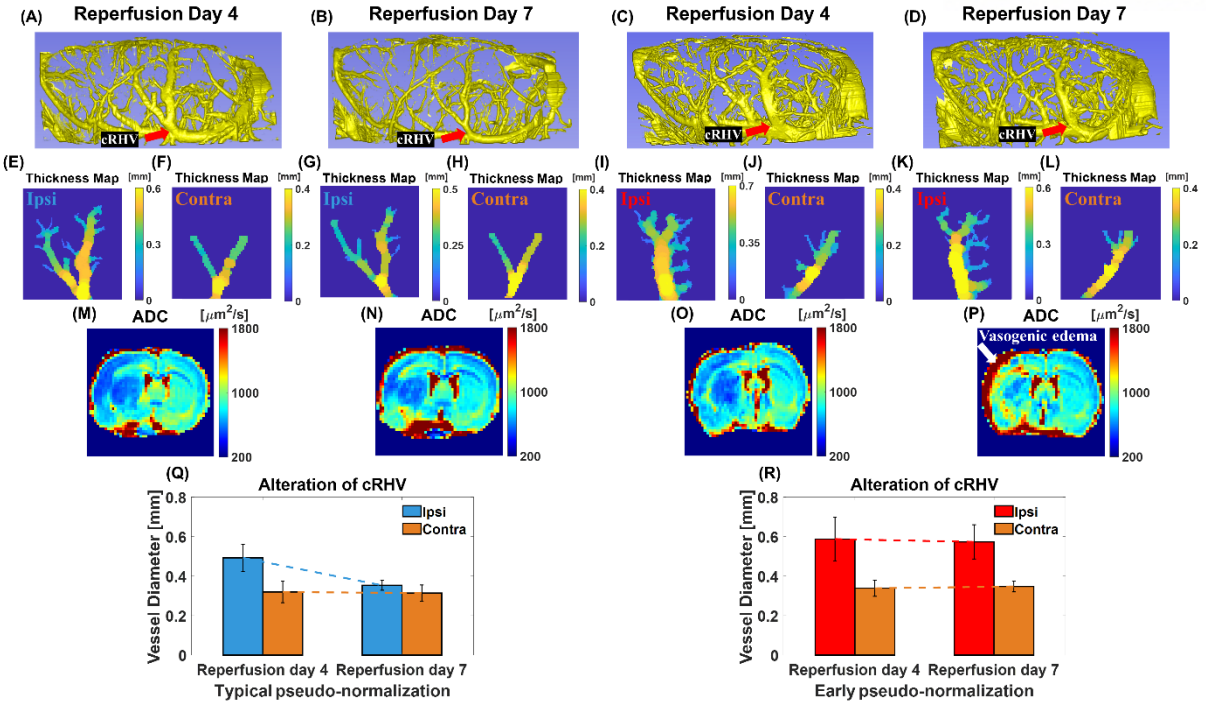

Figure 4.5 Comparison of macrovascular remodeling between typical pseudo-normalization and early pseudo-normalization lesions. (A-D) Lateral views of ipsilateral hemispheres in UTE-MRAs of two representative tMCAO rat models showing typical pseudo-normalization and early pseudo-normalization in cortical lesions at reperfusion days 4 and 7. The red arrows indicate the caudal rhinal veins (cRHVs) in the ipsilateral hemispheres. (E-L) Thickness maps of segmented cRHVs in the ipsilateral and contralateral hemispheres according to acquired UTE-MRAs. The blue letters represent cRHVs in the ipsilateral hemispheres of the tMCAO rat model showing typical pseudo-normalization at reperfusion days 4 and 7 (E and G, respectively). The red letters represent cRHVs in the ipsilateral hemispheres of the tMCAO rat model showing early pseudo-normalization at reperfusion days 4 and 7 (I and K, respectively). The orange letters represent cRHVs in the contralateral hemispheres of two tMCAO rat models (F, H, J, and L). (M-P) The ADC maps of typical pseudo-normalization and early pseudo-normalization lesions showing two tMCAO rat models at reperfusion days 4 and 7. The white arrow indicates vasogenic edema dominant and early pseudo-normalization lesions in the cortex. (Q and R) Bar graphs of the cRHV vessel diameters in the ipsilateral and contralateral hemispheres for typical pseudo-normalization and early pseudo-normalization lesions showing two tMCAO rat models at reperfusion days 4 and 7. The dashed lines show the vessel diameter alterations from reperfusion day 4 to 7.

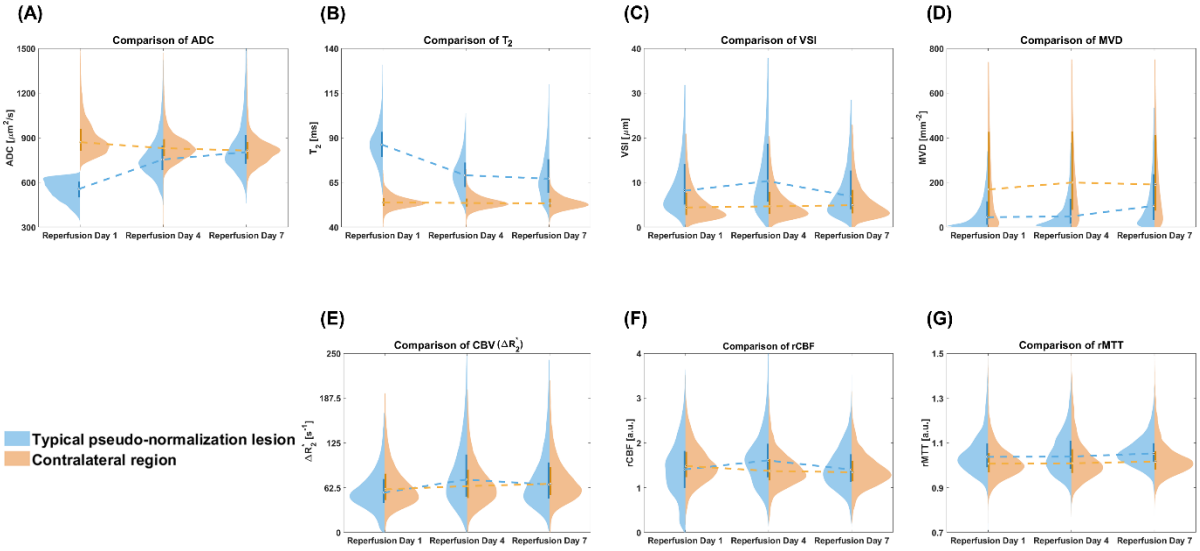

Figure 4.6 Violin plots for histograms and interquartile ranges comparison between typical pseudo-normalization lesion and contralateral region. (a-g) Violin plots of tissue status related ADC and T_2, morphological microvasculature related VSI and MVD, and functional microvasculature related CBV, rCBF, and rMTT in typical pseudo-normalization lesion (blue) and contralateral region (orange) at reperfusion days 1, 4, and 7. Median values are connected with dashed lines.

4.3.5 Correlations between the VSI versus rCBF and the MVD versus rMTT

Scatter plots of the VSI versus rCBF for hyperperfused and the MVD versus rMTT for transit-delay regions are shown in Figure 4.7 to investigate the relationships between morphological and functional microvascular parameters. The results especially link hyperperfusion versus vessel size and delayed transit time versus vessel density. Individual median VSI, rCBF, MVD, and rMTT values were acquired from three ROIs (typical pseudo-normalization, early pseudo-normalization lesions, and the contralateral region) of each tMCAO rat model for each reperfusion day and are shown in a scatterplot in Figure 4.7(A) and (B) (cases with hyperperfusion (A) and delayed transit time (B) were considered). Subsequently, the group median VSI, rCBF, MVD, and rMTT values of all tMCAO rat models were scatter-plotted, as shown in Figure 4.7(C) and (D). The group median values of typical pseudo-normalization (triangle) and early pseudo-normalization (star) lesions were separately included in scatterplots. After Anderson-Darling tests for normal distribution decision, an individual comparison of the VSI and rCBF showed a positive correlation ($r = 0.454$, $p < 0.001$ from paired student's t-test) (Figure 4.7(A)), while the group comparison showed a strong positive correlation ($r = 0.92$, $p < 0.001$ from paired student's t-test) (Figure 4.7(C)). Increased vessel size appears to be related to observed

hyperperfusion in subacute ischemic lesions. On the contrary, an individual comparison of the MVD and rMTT showed a negative correlation ($r = -0.415$, $p < 0.001$ from Wilcoxon signed-rank test) (Figure 4.7(C)), and the group comparison also showed a negative correlation ($r = -0.477$, $p = 0.012$ from paired student's t-test) (Figure 4.7(D)). Individual comparison of the MVD and rMTT (blue circles) showed a much higher correlation at reperfusion day 7 than that at reperfusion days 1 (red circles) and 4 (green circles) with $r = -0.604$ and $p < 0.001$ from Wilcoxon signed-rank test (inset figure of Figure 4.7(B)). This was presumably due to the distinct differences in the MVD and rMTT between early and typical pseudo-normalization lesions at reperfusion day 7. In addition, from the group median comparisons, increasing rMTT values were pair-wisely observed for early pseudo-normalization lesions with decreasing MVD values compared to those of typical pseudo-normalization lesions for each reperfusion day.

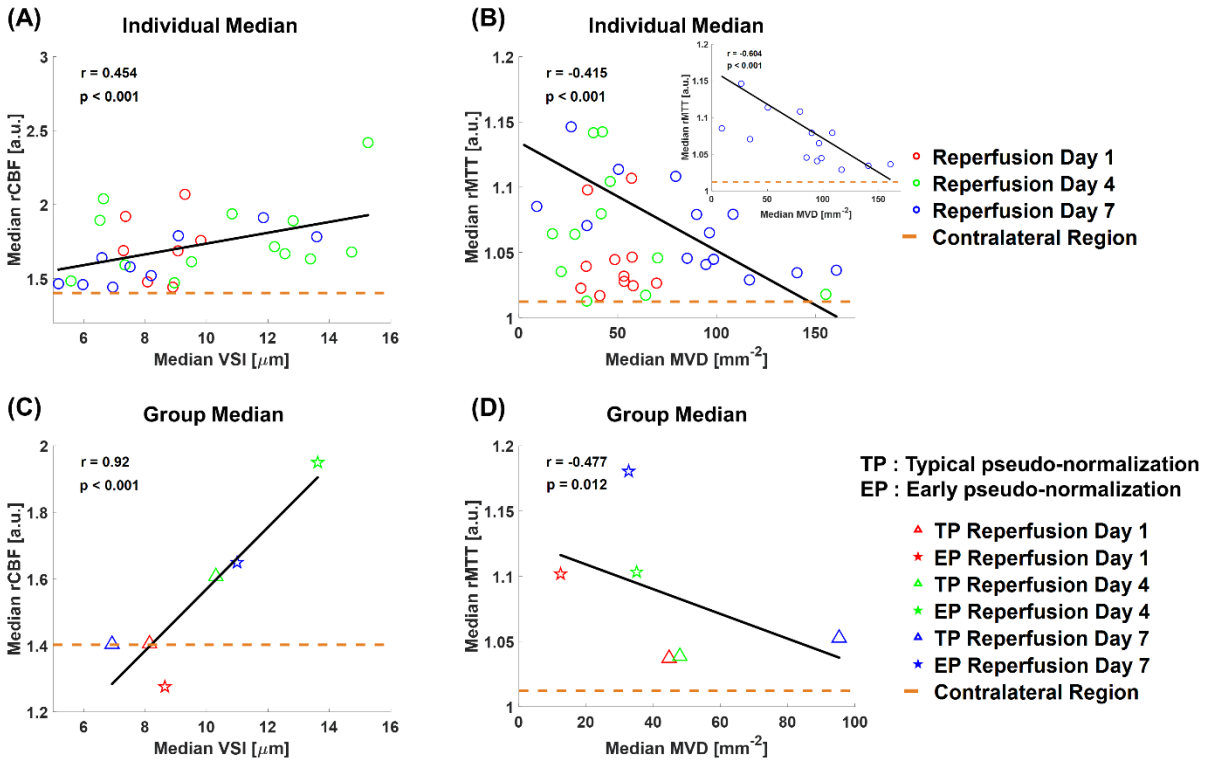

Figure 4.7 Correlations between the VSI versus rCBF and the MVD versus rMTT. (A and B) Scatter plots of the median rCBF and rMTT values over the averaged median rCBF and rMTT values in the contralateral regions of each tMCAO rat model with the corresponding median VSI and MVD values according to reperfusion day 1 (red circles), 4 (green circles), and 7 (blue circles). (inset figure of (B)) Scatter plot of MVD and rMTT at reperfusion day 7. Correlation coefficient $r = 0.454$, $r = -0.415$, and $r = -0.604$ and p-values < 0.001 from the paired student's t-test and Wilcoxon signed-rank tests, respectively. (C and D) Scatter plots of the median VSI versus rCBF and the MVD versus rMTT values

of typical pseudo-normalization (triangle) and early pseudo-normalization lesions (star) from all tMCAO rat models according to reperfusion day 1 (red), 4 (green), and 7 (blue). Correlation coefficient $r = 0.92$ and $r = -0.477$ and $p < 0.001$ and $p = 0.012$ from the paired student's t-tests, respectively. The black solid lines indicate the fitted lines. The orange dashed lines indicate the average median rCBF and rMTT values of the contralateral regions.

4.3.6 Comparisons of the MRI- and LSFM-derived microvascular parameters

To validate the microvascular parameters of the VSI, MVD, and CBV (ΔR_2^*) derived from MRI, LSFM images of two representative tMCAO rat models exhibiting typical pseudo-normalization and early pseudo-normalization in cortex lesions were acquired and quantitatively compared. The contralateral regions and ipsilateral lesions were separately compared in Figures 4.8 and 4.9, respectively. For each tMCAO rat model, six ROIs were selected and analyzed. Figure 4.10(A) shows six representative ROIs (three red ROIs in the ipsilateral lesion and three blue ROIs in the contralateral region) in the maximum intensity projection (MIP) image of 64 μm thickness LSFM images. In addition, a volume-rendered LSFM image via Imaris software (Bitplane, Switzerland) at a thickness of 2 mm is shown for reference in Figure 4.10(B) and addresses the 3-dimensional nature of LSFM images.

MRI-derived morphological microvascular parameters of the VSI and MVD values in the contralateral cortex regions were acquired through six slices at reperfusion day 7 for each tMCAO rat model, and an exemplar ROI is shown as a yellow region overlapped on the VSI and MVD maps, as shown in Figure 4.8(A) and (B), respectively. The median values of the VSI and MVD of each tMCAO rat model are shown as green dashed lines in Figures 4.8(C) and (D), respectively, for 11 cases. The red lines show the averaged VSI and MVD values of 11 tMCAO rat models, which are 4.2 μm and 314.2 mm^{-2}, respectively. MIP images of 64 μm thickness LSFM images are shown in Figures 4.8(E) and (F). In addition, two ROIs (blue boxes) in the contralateral cortex regions with zoomed-in volume-rendered images of each ROI are shown. The mean vessel radius and vessel density were calculated at six ROIs in the contralateral cortex regions (three ROIs for each tMCAO rat model) as blue dashed lines in Figures 4.8(G) and (H), respectively. The red lines show the average values of the mean vessel radius and vessel density, which are 4.26 μm and 286.3 mm^{-2}, respectively. The mean vessel radius and vessel density in Figures 4.8(G) and (H) were calculated from the thickness of 256 μm and 4 μm, respectively, as marked with red arrows in Figures 4.8(I) and (J), respectively. In the contralateral cortex region, the MRI-derived average VSI and MVD values and LSFM-derived average values of the mean vessel radius and vessel density were quantitatively comparable. To further investigate the thickness dependence of the LSFM-derived parameters, the mean vessel radius, vessel density, and BVf were

calculated according to the LSFM image thicknesses of 4, 8, 16, 32, 64, 128, and 256 μm, as shown in Figures 4.8(I), (J), and (K), respectively. The mean vessel radius, vessel density, and BVf of the six ROIs were averaged at each thickness. As the thickness increased, the vessel radius (~ 4 μm) and BVf (~ 2.5%) were not significantly altered, while the vessel density increased, which is also directly visible in the volume-rendered images of one ROI in the contralateral region according to various thicknesses as shown in Figure 4.11.

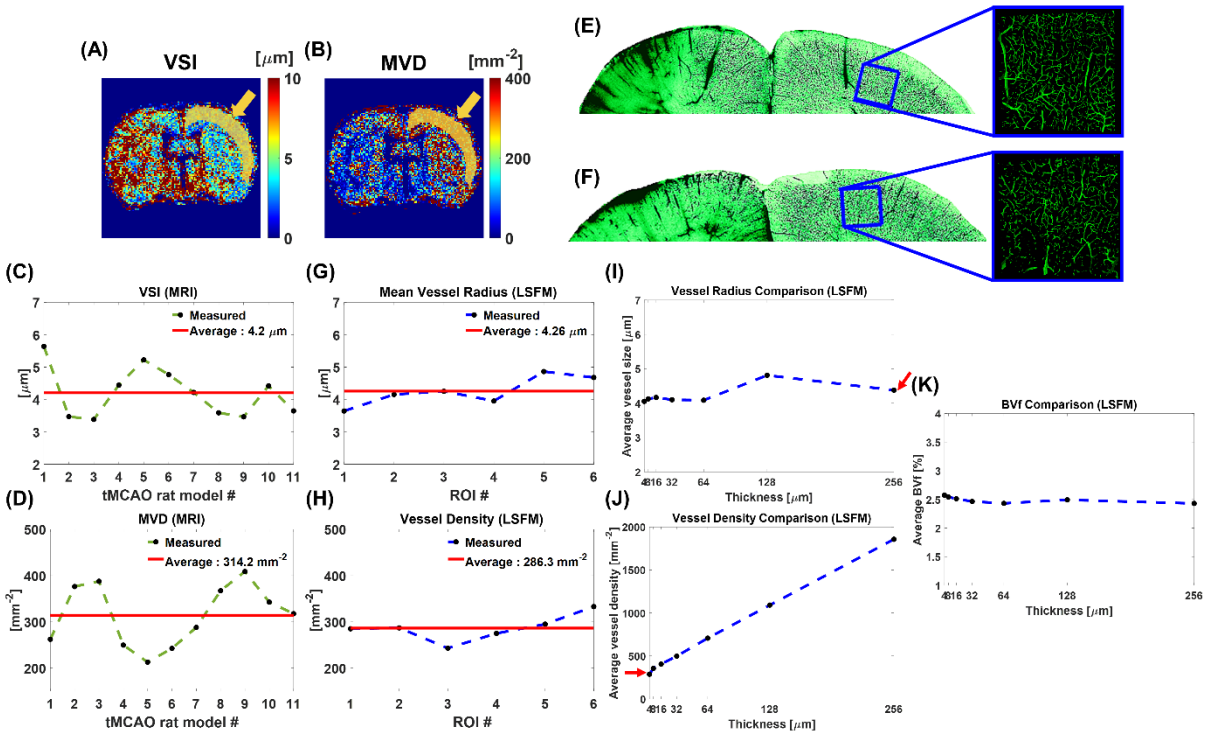

Figure 4.8 Quantitative comparisons of the MRI- and LSFM-derived vessel size and vessel density in the contralateral cortex regions. (A and B) Exemplar VSI and MVD maps at reperfusion day 7. The yellow arrows and overlapped yellow regions in each map indicate the segmented ROI in the contralateral cortex region for comparison. (C and D) Plots of the MRI-derived median VSI and MVD values in the contralateral cortex region for each tMCAO rat model. (E and F) MIP images of 64 μm thickness LSFM images of two representative tMCAO rat models and two ROIs (blue boxes) with zoomed-in volume-rendered images. (G and H) Plots of the LSFM-derived mean vessel radius and vessel density at each ROI. The red solid lines indicate the average values of the vessel sizes and densities derived from MRI and LSFM. (I-K) Comparison of the average mean vessel radii, vessel densities, and BVfs of six ROIs (three ROIs for each tMCAO rat model) according to the thickness of the LSFM image. The red arrows indicate the thickness of the LSFM image for the mean vessel radius and vessel density calculation and comparison (G and H, respectively).

Next, the ipsilateral cortex lesions of two representative cases were compared, as shown in Figure 4.9. MIP images of 64 μm thickness LSFM images are shown in Figures 4.9(A) and (B). In addition, two ROIs (blue boxes) in the ipsilateral cortex lesions with zoomed-in volume-rendered images of each ROI are shown in Figures 4.9(C) and (D). Figure 4.9(C) visually shows a larger vessel size and lower vessel density compared to those of Figure 4.9(D). At reperfusion day 1, cerebral edema was observed in both T_2-weighted images (Figures 4.9(E) and (F)). However, at reperfusion day 7, the ADC map showed abnormally increased ADC values compared to those of the contralateral regions in Figure 4.9(G), which is a signature of vasogenic edema dominant and early pseudo-normalization lesions. The other tMCAO rat model showed a typical pseudo-normalization case (Figure 4.9(H)). For LSFM images of thicknesses of 4, 8, 16, 32, 64, 128, and 256 μm, the average mean vessel radius, vessel density, and BVf of three ROIs for each tMCAO rat model are shown in Figures 4.9(I), (J), and (K), respectively. The early pseudo-normalization lesion showed a higher mean vessel radius than the typical pseudo-normalization lesion for all thicknesses (Figure 4.9(I)). A similar trend was observed for the BVf comparison in Figure 4.9(K). The early pseudo-normalization lesion showed a lower vessel density than the typical pseudo-normalization lesion for all thicknesses (Figure 4.9(J)). For quantitative comparison between the LSFM- and MRI-derived vascular parameters (size, density, and blood volume), the ratios between typical and early pseudo-normalization lesions were compared, as shown in Figures 4.9(L), (M), and (N), respectively. The ratios of MRI-derived vascular parameters were calculated from the median values of all tMCAO rat models at reperfusion day 7. The LSFM-derived ratios were in comparable ranges compared to those that were MRI-derived as marked by red arrows.

Fluorescence images acquired using a fluorescence stereo zoom microscope (without tissue clearing) also verified morphological microvascular remodeling differences between early and typical pseudo-normalization lesions, as shown in Figure 4.12. Figures 4.12(G), (I), (H), and (J) show zoomed-in images of ROIs in typical pseudo-normalization lesions (blue box), early pseudo-normalization lesions (red box), and contralateral regions (orange boxes), respectively. The zoomed-in images show increased vessel size and decreased vessel density in early pseudo-normalization lesions compared to typical pseudo-normalization lesions.

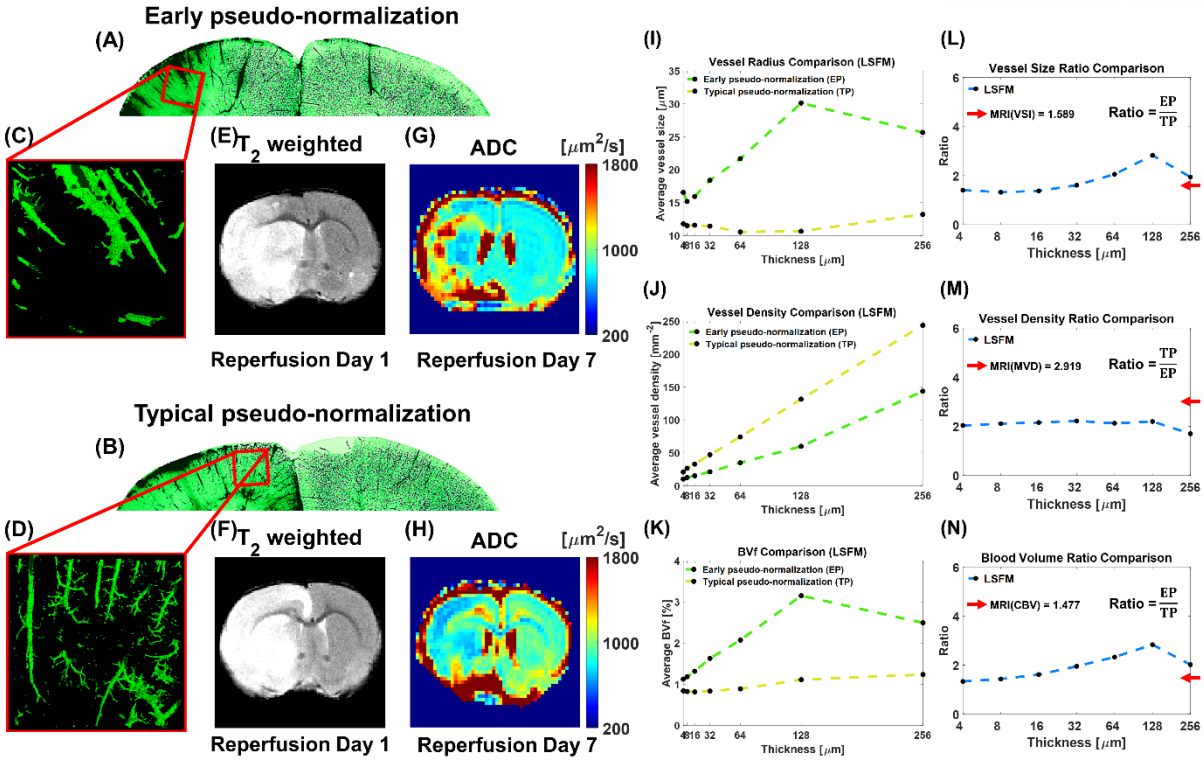

Figure 4.9 Quantitative comparisons of the MRI- and LSFM-derived vessel size, vessel density, and blood volume in the ipsilateral cortex lesions. (A and B) MIP images of 64 μm thickness LSFM images of early pseudo-normalization and typical pseudo-normalization in different tMCAO rat models. (C and D) Zoomed-in volume-rendered images of ROIs (red boxes) in (A) and (B). (E and F) T_2-weighted images at reperfusion day 1. (G and H) ADC maps at reperfusion day 7. (I-K) Comparison of the LSFM-derived averaged mean vessel radii, vessel densities, and BVfs of three ROIs according to the thickness of LSFM image in early pseudo-normalization (green dashed lines) and typical pseudo-normalization lesions (yellow dashed lines). (L-N) The ratios of vessel size, vessel density, and blood volume according to the LSFM image thickness between typical pseudo-normalization (TP) and early pseudo-normalization (EP) lesions. The red arrows indicate the ratios of vessel size (VSI), vessel density (MVD), and blood volume (CBV) derived from MRI.

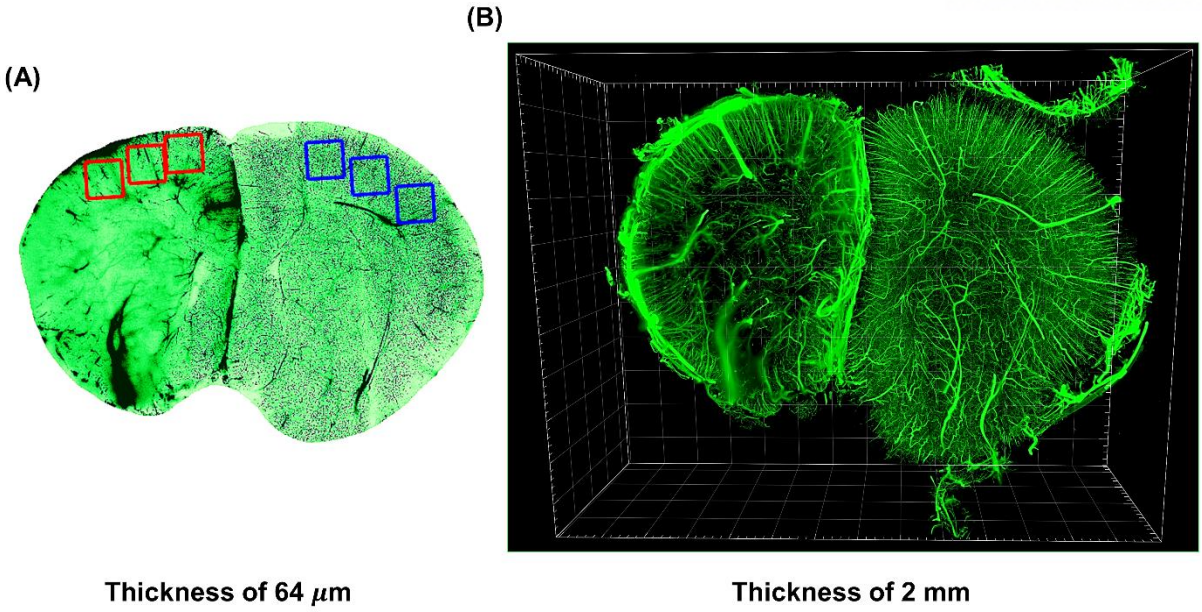

Figure 4.10 Representative LSFM images for visualization of ROIs and whole vasculature. (A) MIP image of 64 μm thickness LSFM images with three ROIs in ipsilateral lesion (red boxes) and three ROIs in contralateral region (blue boxes). (B) Volume-rendered LSFM image at thickness of 2 mm.

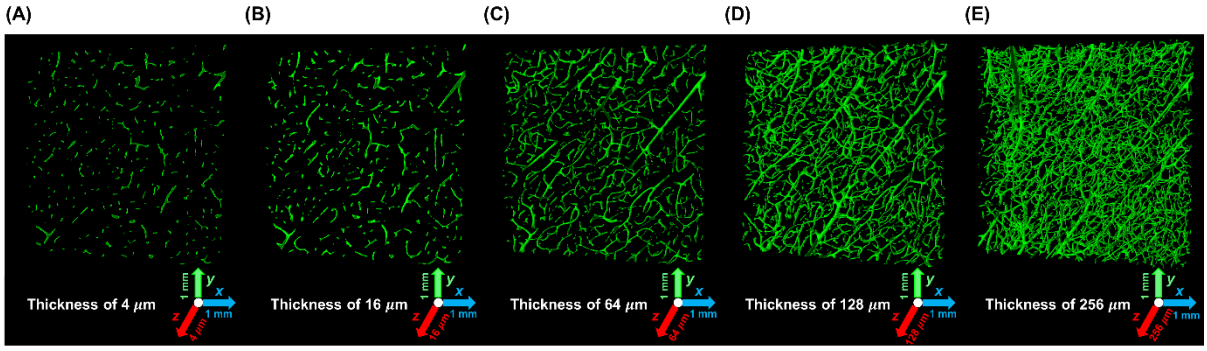

Figure 4.11 Volume-rendered LSFM images of one ROI in contralateral region at various thicknesses. (A-E) Volume-rendered LSFM images of selected one ROI in contralateral region for 3-dimensional visualization at thickness of 4, 16, 64, 128, and 256 μm.

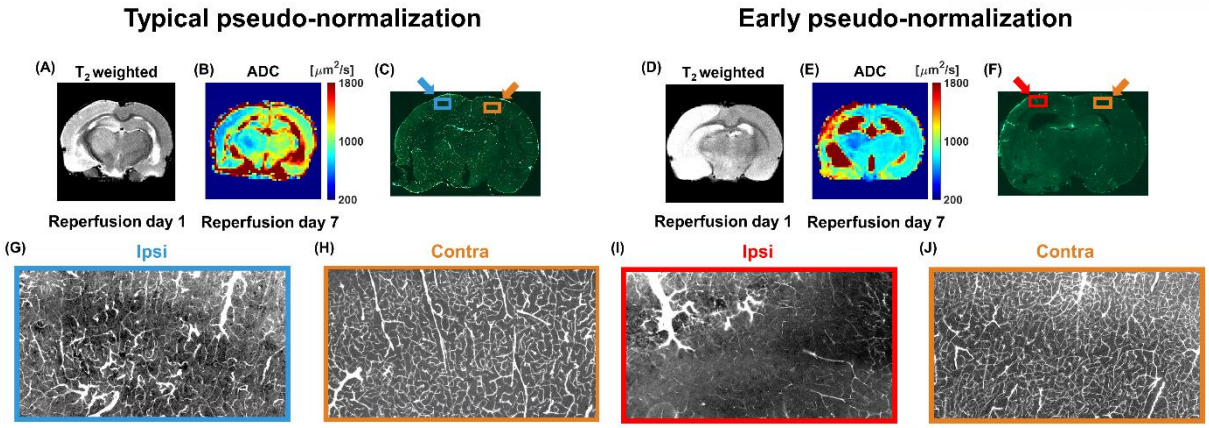

Figure 4.12 Fluorescence stereo zoom microscope image (without tissue clearing) of two tMCAO rat models showing typical pseudo-normalization and early pseudo-normalization in cortex lesion. (A and D) T_2 weighted images at reperfusion day 1. (B and E) ADC maps at reperfusion day 7. (C and F) Fluorescence images of two tMCAO rat models with ROIs. Blue arrow with blue box indicates ROI of typical pseudo-normalization lesion in cortex. Red arrow with red box indicates ROI of early pseudo-normalization lesion in cortex. Orange arrows with orange boxes indicates ROIs of contralateral region in cortex. (G) Zoomed-in images of blue box in typical pseudo-normalization lesion, (H) orange box in contralateral region, (I) red box in early pseudo-normalization lesion, (J) and orange box in contralateral region.

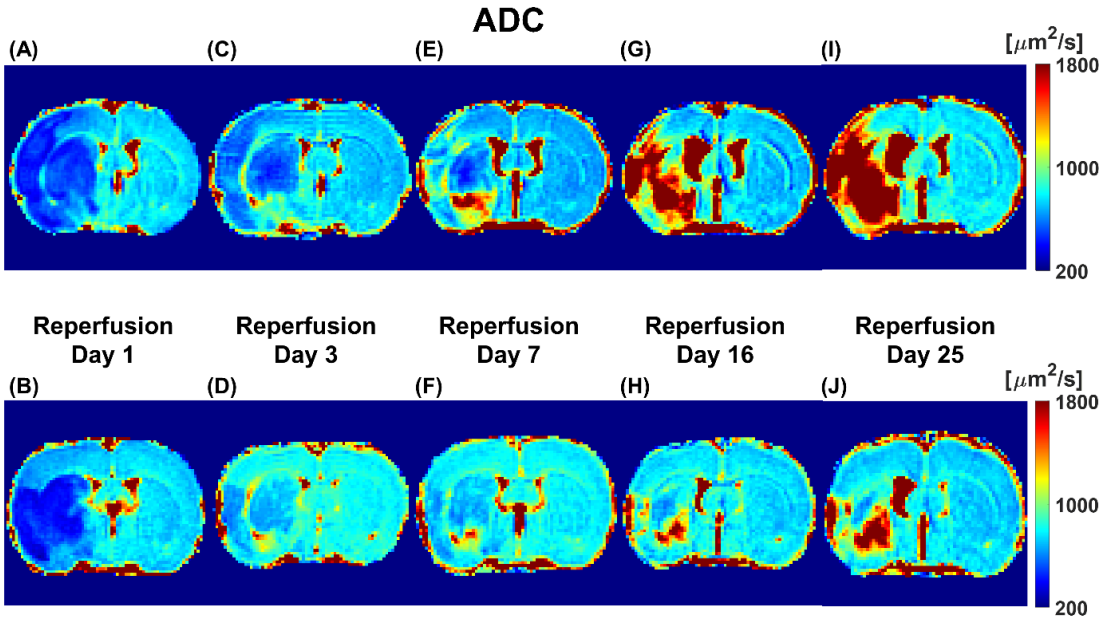

Figure 4.13 Longitudinally acquired ADC maps of two tMCAO rat models showing different vasogenic edema dominancy. (A-J) ADC maps of two tMCAO rat models acquired at reperfusion days 1, 3, 7, 16, and 25.

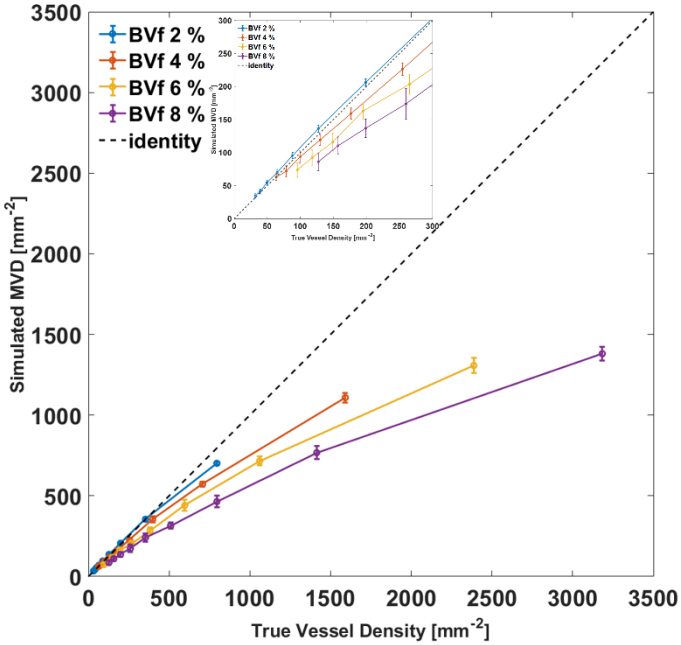

Figure 4.14 Results of Monte Carlo simulation. Comparison of simulated MVD with true vessel density according to BVfs of 2, 4, 6, and 8%. Zoomed-in image (up to true vessel density of 300 mm^{-2}) is shown in inset figure.

4.4 Discussion and conclusions

After a week of reperfusion, tMCAO rat models showed typical pseudo-normalization lesions in the ADC maps. However, there were spatiotemporally different lesions showing early pseudo-normalization of the ADC before then. Accordingly, typical pseudo-normalization and early pseudo-normalization lesions were separately investigated using the edema status (ADC and T_2), and morphological (VSI and MVD), and functional (rCBF and rMTT) vascular remodeling longitudinally. It should be noticed that focal brain ischemia was systematically induced without monitoring of sequential ADC or CBF, which may result in potential bias to acquired data because of inconsistently occluded MCA. At reperfusion day 1, tMCAO rat model showing no edema lesion in T_2-weighted image and/or ADC map was excluded from this study. Although heterogeneous morphological and functional microvascular remodeling were observed, correlative responses between them during the progression of ischemic stroke have not been well established. In a clinical study, hyperperfusion was observed after recanalization, and there is controversy regarding its effectiveness in hyperperfusion. Some cerebral hemodynamic studies have reported that hyperperfusion is a sign of successful recanalization with better clinical outcomes [97-100], while others have reported that hyperperfusion is

correlated with hemorrhagic transformation [97,101,102]. It should be considered that in this study, early pseudo-normalization lesions showed higher rCBF values compared to typical pseudo-normalization lesions. As early pseudo-normalization lesions have a dominance of vasogenic edema, such lesions are more likely to accompany the damaged blood-brain barrier. Thus, hyperperfusion observed in the subacute stage requires cautionary interpretation. The relationship between vascular size and blood volume (flow) in the subacute stage is also informative. Morphological vascular alteration was observed to regulate the CBF [103,104], and this study highlights that hyperperfusion in the subacute stage is driven by enlarged vessel size, even with reduced vessel density and delayed transit time. Besides hyperperfusion, delayed transit time was also observed in lesions. A previous study reported that the net extraction of oxygen negatively correlates with the capillary transit time and is limited mainly by capillary density [105]. The observed delayed transit time and low microvessel density may implicate delayed metabolism due to delayed oxygen and nutrient supply to the lesion. In addition, the association of delayed transit time with respect to low microvessel density provides insight into the role of capillaries in regulating (limiting) the CBF. Although confounding correlations may exist between morphological and functional microvascular remodeling, this result emphasizes the importance of monitoring morphological and functional vascular remodeling after ischemic stroke. Further investigation of vascular remodeling and lesion tissue status is required to estimate the recovery or progression of ischemic stroke in the acute stage.

It is important to emphasize that early pseudo-normalization lesions showed faster and more extensive expansion in the chronic stage. For example, in Figure 4.13, two tMCAO rat models showed different vasogenic edema dominancy in lesions at reperfusion day 7 (Figures 4.13(E) and (F)). A tMCAO rat model showing an extensive vasogenic edema dominant and early pseudo-normalization lesion at reperfusion day 7 displayed much faster expansion of early pseudo-normalization lesions at the chronic stage (reperfusion days 16 and 25), as shown in Figures 4.13(G), (H), (I), and (J). In connection with aggravation of early pseudo-normalization lesion, unnormalized morphological and functional vascular remodeling were observed compared to those of typical pseudo-normalization lesion. This emphasizes the necessity to characterize the lesions of early pseudo-normalization in the early subacute stages. This study observed that reduced MVD and elongated rMTT values were more discriminative factors of early pseudo-normalizations lesions at reperfusion day 1 than conventional ADC and T_2 values, as shown in Figure 4.4 at reperfusion day 1. Interquartile ranges of MVD and rMTT in early pseudo-normalization lesion showed the most conspicuous difference compared to those of typical pseudo-normalization lesion except for the ADC which interquartile range in early pseudo-normalization lesion is close to median value of contralateral region. However, in early pseudo-normalization lesion, CBV and rCBF showed more conspicuous alterations compared to rMTT in

Figure 4.4, which required further investigation regarding their association with edema progression. Assessing morphological and functional vascular remodeling in both edema lesions up to chronic stage could provide more accurate diagnostic and therapeutic information of ischemic stroke.

To validate MRI-derived microvascular remodeling related to the VSI, MVD, and CBV, 3-dimensional LSFM images were acquired and analyzed. In the contralateral cortex regions, the MRI- and LSFM-derived vessel size (4.2 μm and 4.26 μm, respectively) and vessel density (314.2 mm^{-2} and 286.3 mm^{-2}, respectively) quantities were comparable with each other. In addition, the size and density values were consistent with previous reports [13,46,66]. The ratios of the MRI-derived vessel size, vessel density, and blood volume values between early and typical pseudo-normalization lesions were in a comparable range to those of LSFM-derived. However, as the thickness of the LSFM image increased, the estimated vessel density was also observed to be increasing. This is directly visible in Figure 4.11, as more vessels are included with increasing thickness. Considering that MRI- and LSFM-derived vessel densities were comparable at 4∼6 μm of LSFM images, the results are consistent with a previous comparison between the MRI-derived vessel density and corresponding (similar thickness) histology results [46,50,106]. Such underestimation of the MRI-derived vessel density with larger thickness may be partially understood using a Monte Carlo simulation, as shown in Figure 4.14. A simulated MVD was calculated using MRI experimental conditions following previous methods [89]. The difference between the true vessel density and simulated MVD increased as the true vessel density increased. In contrast, the simulated MVD showed a similar value (linearity) with the true vessel density when the true vessel density was under 300 mm^{-2}, as shown in the inset figure of Figure 4.14. Further elucidation is required to rigorously verify the correlation with volumetric MRI-derived MVD and other validation methods, including 3-dimensional LSFM.

It is also noteworthy that the acquisition of LSFM images may be affected by the status of tissue clearing. Although the contralateral region showed complete tissue clearing status, ipsilateral lesions in both tMCAO rat models may not be perfectly cleared due to different tissue conditions than that of the contralateral region, which can induce bias for the absolute quantification of the vessel radius, vessel density, and blood volume. However, the ratio of vascular parameters appears to maintain close resemblance with respect to MRI measurements, which minimizes the clearing issues. In addition, the UTE-MRAs and fluorescence stereo zoom microscope image of two tMCAO rat models (without tissue clearing) showed an enlarged vessel size and reduced vessel density for early pseudo-normalization lesions, which is consistent with tissue-cleared LSFM findings, as shown in Figures 4.5 and 4.12. Establishing an optimization method for perfectly clearing ipsilateral ischemic lesions is necessary for the absolute quantification of microvascular alterations.

In this study, along with the tissue status, morphological and functional vascular remodeling were simultaneously visualized and quantitatively analyzed as reperfusion continued from day 1 to 7 (in the subacute stage). This enabled verification of contrasting vascular remodeling tendencies between early pseudo-normalization and typical pseudo-normalization lesions. Evaluation of both morphological and functional vascular remodeling in two spatiotemporally different lesions may help better inform clinical decision making on the prognosis and treatment of ischemic stroke in the subacute stage.

The original source of Chapter 4 is the article, Kang, M.; Jin, S.; Cho, H., MRI investigation of vascular remodeling for heterogeneous edema lesions in subacute ischemic stroke rat models: Correspondence between cerebral vessel structure and function. *Journal of Cerebral Blood Flow & Metabolism* **2021,** (Accepted).

Chapter 5. Concluding remarks

5.1 Summary

With the requirement of vascular remodeling assessment, dual contrast MRI enabled simultaneous visualization and quantification of whole brain morphological and functional vascular remodeling in ischemic edema lesion. Furthermore, vascular remodeling of spatiotemporally different ischemic edema lesions was separately investigated and those lesions showed different vascular remodeling tendencies. Correlations between morphological and functional vascular remodeling were observed, which could be utilized to understand ischemic stroke induced hemodynamics and metabolism alterations. Acquisition of various vascular parameters provided further information regarding progression of ischemic stroke in addition to conventional measurement of lesion status via ADC and T_2.

5.2 Limitations and Future works

Acquisition of dual contrast MRI for visualization of macro- and microvascular remodeling relies on the assumption that blood-pool contrast agent SPION is not extravasated through blood-brain barrier (BBB). Severe BBB disruption from cerebral edema could induce leakage of SPION and it may result in measurement bias of vascular remodeling. MC simulation was performed in a monotonous vascular system. Single vascular size cylinders were randomly generated in a matrix to represent microvessels in a tissue. However, various sizes of microvessels are populated in a tissue. Consequently, to perform rigorous MC simulation, various sizes of vasculature should be generated in a matrix to represent actual microvessel conditions. As dual contrast MRI acquires various vascular parameters, it takes relatively long scan time, which hampers its routine application. Regarding long scan time, physiological alterations during MR scanning could arise and it may induce translational misunderstanding.

For future researches, more detailed quantitative analysis of vascular remodeling will be performed. As current researches were mainly focused on assessment of vascular remodeling in a subacute phase of ischemic stroke, further vascular remodeling researches including not only subacute phase but also chronic phase of ischemic stroke is required for rigorous development of biomarker. Extended investigation of vascular remodeling will provide further information in aspect of diagnosis and prognosis for ischemic stroke patients.

References

1. De Leucio, A.; De Jesus, O., MR Angiogram. *StatPearls [Internet]* **2020**.
2. Haacke, E. M.; Brown, R. W.; Thompson, M. R.; Venkatesan, R., *Magnetic resonance imaging: physical principles and sequence design*. Wiley-liss New York:: 1999; Vol. 82.
3. Caravan, P.; Ellison, J. J.; McMurry, T. J.; Lauffer, R. B., Gadolinium (III) chelates as MRI contrast agents: structure, dynamics, and applications. *Chemical reviews* **1999,** *99* (9), 2293-2352.
4. Rohrer, M.; Bauer, H.; Mintorovitch, J.; Requardt, M.; Weinmann, H.-J., Comparison of magnetic properties of MRI contrast media solutions at different magnetic field strengths. *Investigative radiology* **2005,** *40* (11), 715-724.
5. Edelman, R. R.; Koktzoglou, I., Noncontrast MR angiography: an update. *Journal of Magnetic Resonance Imaging* **2019,** *49* (2), 355-373.
6. Reichenbach, J. R.; Venkatesan, R.; Schillinger, D. J.; Kido, D. K.; Haacke, E. M., Small vessels in the human brain: MR venography with deoxyhemoglobin as an intrinsic contrast agent. *Radiology* **1997,** *204* (1), 272-277.
7. Reichenbach, J. R.; Haacke, E. M., High-resolution BOLD venographic imaging: a window into brain function. *NMR in Biomedicine: An International Journal Devoted to the Development and Application of Magnetic Resonance In Vivo* **2001,** *14* (7-8), 453-467.
8. Prince, M. R.; Yucel, E. K.; Kaufman, J. A.; Harrison, D. C.; Geller, S. C., Dynamic gadolinium-enhanced three-dimensional abdominal MR arteriography. *Journal of Magnetic Resonance Imaging* **1993,** *3* (6), 877-881.
9. Prince, M. R., Gadolinium-enhanced MR aortography. *Radiology* **1994,** *191* (1), 155-164.
10. Ho, V. B.; Corse, W. R.; Maki, J. H., Contrast-enhanced MR angiography: theory and technical optimization. In *Magnetic Resonance Angiography*, Springer: 2005; pp 23-42.
11. Robson, M. D.; Gatehouse, P. D.; Bydder, M.; Bydder, G. M., Magnetic resonance: an introduction to ultrashort TE (UTE) imaging. *Journal of computer assisted tomography* **2003,** *27* (6), 825-846.
12. Herrmann, K.-H.; Krämer, M.; Reichenbach, J. R., Time efficient 3D radial UTE sampling with fully automatic delay compensation on a clinical 3T MR scanner. *PloS one* **2016,** *11* (3), e0150371.
13. Troprès, I.; Pannetier, N.; Grand, S.; Lemasson, B.; Moisan, A.; Péoc'h, M.; Rémy, C.; Barbier, E. L., Imaging the microvessel caliber and density: principles and applications of microvascular MRI. *Magnetic resonance in medicine* **2015,** *73* (1), 325-341.
14. Seevinck, P. R.; Deddens, L. H.; Dijkhuizen, R. M., Magnetic resonance imaging of brain

angiogenesis after stroke. *Angiogenesis* **2010,** *13* (2), 101-111.

15. Calamante, F.; Thomas, D. L.; Pell, G. S.; Wiersma, J.; Turner, R., Measuring cerebral blood flow using magnetic resonance imaging techniques. *Journal of cerebral blood flow & metabolism* **1999,** *19* (7), 701-735.
16. Jahng, G.-H.; Li, K.-L.; Ostergaard, L.; Calamante, F., Perfusion magnetic resonance imaging: a comprehensive update on principles and techniques. *Korean journal of radiology* **2014,** *15* (5), 554.
17. McGehee, B. E.; Pollock, J. M.; Maldjian, J. A., Brain perfusion imaging: how does it work and what should I use? *Journal of magnetic resonance imaging* **2012,** *36* (6), 1257-1272.
18. Petrella, J. R.; Provenzale, J. M., MR perfusion imaging of the brain: techniques and applications. *American Journal of roentgenology* **2000,** *175* (1), 207-219.
19. Essig, M.; Shiroishi, M. S.; Nguyen, T. B.; Saake, M.; Provenzale, J. M.; Enterline, D.; Anzalone, N.; Dörfler, A.; Rovira, À.; Wintermark, M., Perfusion MRI: the five most frequently asked technical questions. *American Journal of Roentgenology* **2013,** *200* (1), 24-34.
20. Zaharchuk, G., Theoretical basis of hemodynamic MR imaging techniques to measure cerebral blood volume, cerebral blood flow, and permeability. *American Journal of Neuroradiology* **2007,** *28* (10), 1850-1858.
21. Zierler, K. L., Theoretical basis of indicator-dilution methods for measuring flow and volume. *Circulation Research* **1962,** *10* (3), 393-407.
22. Østergaard, L., Principles of cerebral perfusion imaging by bolus tracking. *Journal of Magnetic Resonance Imaging: An Official Journal of the International Society for Magnetic Resonance in Medicine* **2005,** *22* (6), 710-717.
23. Liu, J.; Wang, Y.; Akamatsu, Y.; Lee, C. C.; Stetler, R. A.; Lawton, M. T.; Yang, G.-Y., Vascular remodeling after ischemic stroke: mechanisms and therapeutic potentials. *Progress in neurobiology* **2014,** *115*, 138-156.
24. Prior, B. M.; Yang, H.; Terjung, R. L., What makes vessels grow with exercise training? *Journal of applied physiology* **2004,** *97* (3), 1119-1128.
25. Tuttle, J. L.; Nachreiner, R. D.; Bhuller, A. S.; Condict, K. W.; Connors, B. A.; Herring, B. P.; Dalsing, M. C.; Unthank, J. L., Shear level influences resistance artery remodeling: wall dimensions, cell density, and eNOS expression. *American Journal of Physiology-Heart and Circulatory Physiology* **2001,** *281* (3), H1380-H1389.
26. Heil, M.; Eitenmüller, I.; Schmitz-Rixen, T.; Schaper, W., Arteriogenesis versus

angiogenesis: similarities and differences. *Journal of cellular and molecular medicine* **2006,** *10* (1), 45-55.

27. Arai, K.; Jin, G.; Navaratna, D.; Lo, E. H., Brain angiogenesis in developmental and pathological processes: neurovascular injury and angiogenic recovery after stroke. *The FEBS journal* **2009,** *276* (17), 4644-4652.
28. Slevin, M.; Kumar, P.; Gaffney, J.; Kumar, S.; Krupinski, J., Can angiogenesis be exploited to improve stroke outcome? Mechanisms and therapeutic potential. *Clinical Science* **2006,** *111* (3), 171-183.
29. Angels Font, M.; Arboix, A.; Krupinski, J., Angiogenesis, neurogenesis and neuroplasticity in ischemic stroke. *Current cardiology reviews* **2010,** *6* (3), 238-244.
30. Henderson, R. D.; Eliasziw, M.; Fox, A. J.; Rothwell, P. M.; Barnett, H. J., Angiographically defined collateral circulation and risk of stroke in patients with severe carotid artery stenosis. *Stroke* **2000,** *31* (1), 128-132.
31. Lima, F. O.; Furie, K. L.; Silva, G. S.; Lev, M. H.; Camargo, É. C.; Singhal, A. B.; Harris, G. J.; Halpern, E. F.; Koroshetz, W. J.; Smith, W. S., The pattern of leptomeningeal collaterals on CT angiography is a strong predictor of long-term functional outcome in stroke patients with large vessel intracranial occlusion. *Stroke* **2010,** *41* (10), 2316-2322.
32. Bang, O. Y.; Saver, J. L.; Kim, S. J.; Kim, G.-M.; Chung, C.-S.; Ovbiagele, B.; Lee, K. H.; Liebeskind, D. S., Collateral flow predicts response to endovascular therapy for acute ischemic stroke. *Stroke* **2011,** *42* (3), 693-699.
33. Ribo, M.; Flores, A.; Rubiera, M.; Pagola, J.; Sargento-Freitas, J.; Rodriguez-Luna, D.; Coscojuela, P.; Maisterra, O.; Piñeiro, S.; Romero, F. J., Extending the time window for endovascular procedures according to collateral pial circulation. *Stroke* **2011,** *42* (12), 3465-3469.
34. Bang, O. Y.; Saver, J. L.; Kim, S. J.; Kim, G.-M.; Chung, C.-S.; Ovbiagele, B.; Lee, K. H.; Liebeskind, D. S.; Collaborators, U.-S. S., Collateral flow averts hemorrhagic transformation after endovascular therapy for acute ischemic stroke. *Stroke* **2011,** *42* (8), 2235-2239.
35. Krupinski, J.; Kaluza, J.; Kumar, P.; Kumar, S.; Wang, J. M., Role of angiogenesis in patients with cerebral ischemic stroke. *Stroke* **1994,** *25* (9), 1794-1798.
36. Jiang, L.; Su, H.-B.; Zhang, Y.-D.; Zhou, J.-S.; Geng, W.; Chen, H.; Xu, Q.; Yin, X.; Chen, Y.-C., Collateral vessels on magnetic resonance angiography in endovascular-treated acute ischemic stroke patients associated with clinical outcomes. *Oncotarget* **2017,** *8*

(46), 81529.

37. Ichijo, M.; Miki, K.; Ishibashi, S.; Tomita, M.; Kamata, T.; Fujigasaki, H.; Mizusawa, H., Posterior cerebral artery laterality on magnetic resonance angiography predicts long-term functional outcome in middle cerebral artery occlusion. *Stroke* **2013,** *44* (2), 512-515.
38. Iwasawa, E.; Ichijo, M.; Ishibashi, S.; Yokota, T., Acute development of collateral circulation and therapeutic prospects in ischemic stroke. *Neural regeneration research* **2016,** *11* (3), 368.
39. Besselmann, M.; Liu, M.; Diedenhofen, M.; Franke, C.; Hoehn, M., MR angiographic investigation of transient focal cerebral ischemia in rat. *NMR in Biomedicine: An International Journal Devoted to the Development and Application of Magnetic Resonance In Vivo* **2001,** *14* (5), 289-296.
40. Jung, H.; Park, B.; Lee, C.; Cho, J.; Suh, J.; Park, J.; Kim, Y.; Kim, J.; Cho, G.; Cho, H., Dual MRI T1 and T2 (∗) contrast with size-controlled iron oxide nanoparticles. *Nanomedicine: Nanotechnology, Biology and Medicine* **2014,** *10* (8), 1679-1689.
41. Jung, H.; Jin, S.; Cho, J.; Han, S.; Lee, D.; Cho, H., UTE–ΔR2–ΔR2* combined MR whole-brain angiogram using dual-contrast superparamagnetic iron oxide nanoparticles. *NMR in Biomedicine* **2016,** *29* (6), 690-701.
42. Jensen, J.; Chandra, R., MR imaging of microvasculature. *Magnetic Resonance in Medicine: An Official Journal of the International Society for Magnetic Resonance in Medicine* **2000,** *44* (2), 224-230.
43. Tropres, I.; Grimault, S.; Vaeth, A.; Grillon, E.; Julien, C.; Payen, J. F.; Lamalle, L.; Décorps, M., Vessel size imaging. *Magnetic Resonance in Medicine: An Official Journal of the International Society for Magnetic Resonance in Medicine* **2001,** *45* (3), 397-408.
44. Moisan, A.; Favre, I. M.; Rome, C.; Grillon, E.; Naegele, B.; Barbieux, M.; De Fraipont, F.; Richard, M.-J.; Barbier, E. L.; Rémy, C., Microvascular plasticity after experimental stroke: a molecular and MRI study. *Cerebrovascular Diseases* **2014,** *38* (5), 344-353.
45. Xu, C.; Schmidt, W. U.; Villringer, K.; Brunecker, P.; Kiselev, V.; Gall, P.; Fiebach, J. B., Vessel size imaging reveals pathological changes of microvessel density and size in acute ischemia. *Journal of Cerebral Blood Flow & Metabolism* **2011,** *31* (8), 1687-1695.
46. Bosomtwi, A.; Jiang, Q.; Ding, G. L.; Zhang, L.; Zhang, Z. G.; Lu, M.; Ewing, J. R.; Chopp, M., Quantitative evaluation of microvascular density after stroke in rats using

MRI. *Journal of Cerebral Blood Flow & Metabolism* **2008,** *28* (12), 1978-1987.

47. Lin, C.-Y.; Chang, C.; Cheung, W.-M.; Lin, M.-H.; Chen, J.-J.; Hsu, C. Y.; Chen, J.-H.; Lin, T.-N., Dynamic changes in vascular permeability, cerebral blood volume, vascular density, and size after transient focal cerebral ischemia in rats: evaluation with contrast-enhanced magnetic resonance imaging. *Journal of Cerebral Blood Flow & Metabolism* **2008,** *28* (8), 1491-1501
48. Boehm-Sturm, P.; Farr, T. D.; Adamczak, J.; Jikeli, J. F.; Mengler, L.; Wiedermann, D.; Kallur, T.; Kiselev, V.; Hoehn, M., Vascular changes after stroke in the rat: a longitudinal study using optimized magnetic resonance imaging. *Contrast media & molecular imaging* **2013,** *8* (5), 383-392.
49. Ielacqua, G. D.; Schlegel, F.; Füchtemeier, M.; Xandry, J.; Rudin, M.; Klohs, J., Magnetic resonance Q mapping reveals a decrease in microvessel density in the arcaβ mouse model of cerebral amyloidosis. *Frontiers in aging neuroscience* **2016,** *7*, 241.
50. Wu, E. X.; Tang, H.; Jensen, J. H., High-resolution MR imaging of mouse brain microvasculature using the relaxation rate shift index Q. *NMR in Biomedicine: An International Journal Devoted to the Development and Application of Magnetic Resonance In Vivo* **2004,** *17* (7), 507-512.
51. Kohno, K.; Back, T.; Hoehn-Berlage, M.; Hossmann, K.-A., A modified rat model of middle cerebral artery thread occlusion under electrophysiological control for magnetic resonance investigations. *Magnetic resonance imaging* **1995,** *13* (1), 65-71.
52. Uluç, K.; Miranpuri, A.; Kujoth, G. C.; Aktüre, E.; Başkaya, M. K., Focal cerebral ischemia model by endovascular suture occlusion of the middle cerebral artery in the rat. *JoVE (Journal of Visualized Experiments)* **2011,** (48), e1978.
53. Pathak, A. P.; Ward, B. D.; Schmainda, K. M., A novel technique for modeling susceptibility-based contrast mechanisms for arbitrary microvascular geometries: the finite perturber method. *Neuroimage* **2008,** *40* (3), 1130-1143.
54. Lee, D.; Song, Y. K.; Park, B.; Cho, H.; Yeom, J. S.; Cho, G.; Cho, H., The robustness of T 2 value as a trabecular structural index at multiple spatial resolutions of 7 Tesla MRI. *Magnetic resonance in medicine* **2018,** *80* (5), 1949-1961.
55. Han, S.; Cho, J.; Jung, H.; Suh, J.; Kim, J.; Kim, Y.; Cho, G.; Cho, H., Robust MR assessment of cerebral blood volume and mean vessel size using SPION-enhanced ultrashort echo acquisition. *NeuroImage* **2015,** *112*, 382-389.
56. Kim, S. G.; Harel, N.; Jin, T.; Kim, T.; Lee, P.; Zhao, F., Cerebral blood volume MRI with intravascular superparamagnetic iron oxide nanoparticles. *NMR in Biomedicine* **2013,**

26 (8), 949-962.

57. Maggioni, M.; Katkovnik, V.; Egiazarian, K.; Foi, A., Nonlocal transform-domain filter for volumetric data denoising and reconstruction. *IEEE transactions on image processing* **2012,** *22* (1), 119-133.
58. Kjonigsen, L. J.; Lillehaug, S.; Bjaalie, J. G.; Witter, M. P.; Leergaard, T. B., Waxholm Space atlas of the rat brain hippocampal region: three-dimensional delineations based on magnetic resonance and diffusion tensor imaging. *Neuroimage* **2015,** *108*, 441-449.
59. Hildebrand, T.; Rüegsegger, P., A new method for the model-independent assessment of thickness in three-dimensional images. *Journal of microscopy* **1997,** *185* (1), 67-75.
60. Doube, M.; Kłosowski, M. M.; Arganda-Carreras, I.; Cordelières, F. P.; Dougherty, R. P.; Jackson, J. S.; Schmid, B.; Hutchinson, J. R.; Shefelbine, S. J., BoneJ: free and extensible bone image analysis in ImageJ. *Bone* **2010,** *47* (6), 1076-1079.
61. Mayerich, D.; Abbott, L.; McCormick, B., Knife-edge scanning microscopy for imaging and reconstruction of three-dimensional anatomical structures of the mouse brain. *Journal of microscopy* **2008,** *231* (1), 134-143.
62. Mayerich, D.; Kwon, J.; Sung, C.; Abbott, L.; Keyser, J.; Choe, Y., Fast macro-scale transmission imaging of microvascular networks using KESM. *Biomedical optics express* **2011,** *2* (10), 2888-2896.
63. Schlaug, G.; Siewert, B.; Benfield, A.; Edelman, R.; Warach, S., Time course of the apparent diffusion coefficient (ADC) abnormality in human stroke. *Neurology* **1997,** *49* (1), 113-119.
64. Lansberg, M. G.; Thijs, V. N.; O'Brien, M. W.; Ali, J. O.; De Crespigny, A. J.; Tong, D. C.; Moseley, M. E.; Albers, G. W., Evolution of apparent diffusion coefficient, diffusion-weighted, and T2-weighted signal intensity of acute stroke. *American Journal of Neuroradiology* **2001,** *22* (4), 637-644.
65. Albers, G. W., Diffusion-weighted MRI for evaluation of acute stroke. *Neurology* **1998,** *51* (3 Suppl 3), S47-S49.
66. Lemasson, B.; Valable, S.; Farion, R.; Krainik, A.; Rémy, C.; Barbier, E. L., In vivo imaging of vessel diameter, size, and density: a comparative study between MRI and histology. *Magnetic resonance in medicine* **2013,** *69* (1), 18-26.
67. Yanev, P.; Seevinck, P. R.; Rudrapatna, U. S.; Bouts, M. J.; van der Toorn, A.; Gertz, K.; Kronenberg, G.; Endres, M.; van Tilborg, G. A.; Dijkhuizen, R. M., Magnetic resonance imaging of local and remote vascular remodelling after experimental stroke. *Journal of Cerebral Blood Flow & Metabolism* **2017,** *37* (8), 2768-2779.

68. Duong, T. Q.; Kim, S. G., In vivo MR measurements of regional arterial and venous blood volume fractions in intact rat brain. *Magnetic Resonance in Medicine: An Official Journal of the International Society for Magnetic Resonance in Medicine* **2000,** *43* (3), 393-402.

69. Bosomtwi, A.; Chopp, M.; Zhang, L.; Zhang, Z. G.; Lu, M.; Jiang, Q., Mean microvessel segment length and radius after embolic stroke: Comparison of magnetic resonance imaging (MRI) and laser scanning confocal microscopy (LSCM). *Brain research* **2011,** *1381*, 217-227.

70. Lustig, M.; Donoho, D.; Pauly, J. M., Sparse MRI: The application of compressed sensing for rapid MR imaging. *Magnetic Resonance in Medicine: An Official Journal of the International Society for Magnetic Resonance in Medicine* **2007,** *58* (6), 1182-1195.

71. Wang, Y., Description of parallel imaging in MRI using multiple coils. *Magnetic Resonance in Medicine: An Official Journal of the International Society for Magnetic Resonance in Medicine* **2000,** *44* (3), 495-499.

72. Dong, C.; Loy, C. C.; He, K.; Tang, X., Image super-resolution using deep convolutional networks. *IEEE transactions on pattern analysis and machine intelligence* **2015,** *38* (2), 295-307.

73. Chen, Y.; Xie, Y.; Zhou, Z.; Shi, F.; Christodoulou, A. G.; Li, D. In *Brain MRI super resolution using 3D deep densely connected neural networks*, 2018 IEEE 15th International Symposium on Biomedical Imaging (ISBI 2018), IEEE: 2018; pp 739-742.

74. Mader, I.; Schöning, M.; Klose, U.; Küker, W., Neonatal cerebral infarction diagnosed by diffusion-weighted MRI: pseudonormalization occurs early. *Stroke* **2002,** *33* (4), 1142-1145.

75. Roberts, T. P.; Rowley, H. A., Diffusion weighted magnetic resonance imaging in stroke. *European journal of radiology* **2003,** *45* (3), 185-194.

76. Schwamm, L. H.; Koroshetz, W. J.; Sorensen, A. G.; Wang, B.; Copen, W. A.; Budzik, R.; Rordorf, G.; Buonanno, F. S.; Schaefer, P. W.; Gonzalez, R. G., Time course of lesion development in patients with acute stroke: serial diffusion-and hemodynamic-weighted magnetic resonance imaging. *Stroke* **1998,** *29* (11), 2268-2276.

77. Walker, P. M.; Salem, D. e. B.; Lalande, A.; Giroud, M.; Brunotte, F., Time course of NAA T2 and ADCw in ischaemic stroke patients: 1H MRS imaging and diffusion-weighted MRI. *Journal of the neurological sciences* **2004,** *220* (1-2), 23-28.

78. Warach, S.; Gaa, J.; Siewert, B.; Wielopolski, P.; Edelman, R. R., Acute human stroke studied by whole brain echo planar diffusion-weighted magnetic resonance imaging. *Annals of Neurology: Official Journal of the American Neurological Association and the Child*

Neurology Society **1995,** *37* (2), 231-241.

79. Keep, R.; Andjelkovic, A.; Xi, G., Cytotoxic and Vasogenic Brain Edema. In *Primer on Cerebrovascular Diseases*, Elsevier: 2017; pp 145-149.
80. Michinaga, S.; Koyama, Y., Pathogenesis of brain edema and investigation into anti-edema drugs. *International journal of molecular sciences* **2015,** *16* (5), 9949-9975.
81. Liang, D.; Bhatta, S.; Gerzanich, V.; Simard, J. M., Cytotoxic edema: mechanisms of pathological cell swelling. *Neurosurgical focus* **2007,** *22* (5), 1-9.
82. Rosenberg, G. A., Ischemic brain edema. *Progress in cardiovascular diseases* **1999,** *42* (3), 209-216.
83. Klatzo, I., Pathophysiological aspects of brain edema. *Acta neuropathologica* **1987,** *72* (3), 236-239.
84. Rogers, H. J.; McGarry, B. L.; Knight, M. J.; Jokivarsi, K. T.; Gröhn, O. H.; Kauppinen, R. A., Timing the ischaemic stroke by 1H-MRI: improved accuracy using absolute relaxation times over signal intensities. *NeuroReport* **2014,** *25* (15), 1180-1185.
85. McGarry, B. L.; Rogers, H. J.; Knight, M. J.; Jokivarsi, K. T.; Sierra, A.; Gröhn, O. H.; Kauppinen, R. A., Stroke onset time estimation from multispectral quantitative magnetic resonance imaging in a rat model of focal permanent cerebral ischemia. *International Journal of Stroke* **2016,** *11* (6), 677-682.
86. Jha, S., Cerebral edema and its management. *Medical Journal, Armed Forces India* **2003,** *59* (4), 326.
87. Walcott, B. P.; Kahle, K. T.; Simard, J. M., Novel treatment targets for cerebral edema. *Neurotherapeutics* **2012,** *9* (1), 65-72.
88. Rosenberg, G. A.; Yang, Y., Vasogenic edema due to tight junction disruption by matrix metalloproteinases in cerebral ischemia. *Neurosurgical focus* **2007,** *22* (5), 1-9.
89. Kang, M.; Jin, S.; Lee, D.; Cho, H., MRi Visualization of Whole Brain Macro-and Microvascular Remodeling in a Rat Model of ischemic Stroke: A pilot Study. *Scientific reports* **2020,** *10* (1), 1-12.
90. Wang, D. J.; Alger, J. R.; Qiao, J. X.; Hao, Q.; Hou, S.; Fiaz, R.; Gunther, M.; Pope, W. B.; Saver, J. L.; Salamon, N., The value of arterial spin-labeled perfusion imaging in acute ischemic stroke: comparison with dynamic susceptibility contrast-enhanced MRI. *Stroke* **2012,** *43* (4), 1018-1024.
91. Copen, W. A.; Schaefer, P. W.; Wu, O., MR perfusion imaging in acute ischemic stroke. *Neuroimaging Clinics* **2011,** *21* (2), 259-283.
92. Shen, Q.; Duong, T. Q., Magnetic resonance imaging of cerebral blood flow in animal stroke

models. *Brain circulation* **2016,** *2* (1), 20.

93. Percie du Sert, N.; Hurst, V.; Ahluwalia, A.; Alam, S.; Avey, M. T.; Baker, M.; Browne, W. J.; Clark, A.; Cuthill, I. C.; Dirnagl, U., The ARRIVE guidelines 2.0: Updated guidelines for reporting animal research. *Journal of Cerebral Blood Flow & Metabolism* **2020,** *40* (9), 1769-1777.
94. Lee, D.; Kang, M.; Cho, H., MRI size assessment of cerebral microvasculature using diffusion-time-dependent stimulated-echo acquisition: A feasibility study in rodent. *NeuroImage* **2020**, 116784.
95. Gage, G. J.; Kipke, D. R.; Shain, W., Whole animal perfusion fixation for rodents. *JoVE (Journal of Visualized Experiments)* **2012,** (65), e3564.
96. Barbier, E. L.; Lamalle, L.; Décorps, M., Methodology of brain perfusion imaging. *Journal of Magnetic Resonance Imaging: An Official Journal of the International Society for Magnetic Resonance in Medicine* **2001,** *13* (4), 496-520.
97. Zhang, Z.; Pu, Y.; Mi, D.; Liu, L., Cerebral hemodynamic evaluation after cerebral recanalization therapies for acute ischemic stroke. *Frontiers in neurology* **2019,** *10*, 719.
98. Bivard, A.; Stanwell, P.; Levi, C.; Parsons, M., Arterial spin labeling identifies tissue salvage and good clinical recovery after acute ischemic stroke. *Journal of neuroimaging* **2013,** *23* (3), 391-396.
99. Marchal, G.; Young, A. R.; Baron, J.-C., Early postischemic hyperperfusion: pathophysiologic insights from positron emission tomography. *Journal of Cerebral Blood Flow & Metabolism* **1999,** *19* (5), 467-482.
100. Marchal, G.; Furlan, M.; Beaudouin, V.; Rioux, P.; Hauttement, J. L.; Serrati, C.; de la Sayette, V.; Doze, F. L.; Viader, F.; Derlon, J. M., Early spontaneous hyperperfusion after stroke: A marker of favourable tissue outcome? *Brain* **1996,** *119* (2), 409-419.
101. Yu, S.; Liebeskind, D. S.; Dua, S.; Wilhalme, H.; Elashoff, D.; Qiao, X. J.; Alger, J. R.; Sanossian, N.; Starkman, S.; Ali, L. K., Postischemic hyperperfusion on arterial spin labeled perfusion MRI is linked to hemorrhagic transformation in stroke. *Journal of Cerebral Blood Flow & Metabolism* **2015,** *35* (4), 630-637.
102. Yu, S.; Ma, S. J.; Liebeskind, D. S.; Yu, D.; Li, N.; Qiao, X. J.; Shao, X.; Yan, L.; Yoo, B.; Scalzo, F., ASPECTS-based reperfusion status on arterial spin labeling is associated with clinical outcome in acute ischemic stroke patients. *Journal of Cerebral Blood Flow & Metabolism* **2018,** *38* (3), 382-392.
103. Paulson, O.; Strandgaard, S.; Edvinsson, L., Cerebral autoregulation. *Cerebrovascular and*

brain metabolism reviews **1990,** *2* (2), 161-192.

104. Hall, C. N.; Reynell, C.; Gesslein, B.; Hamilton, N. B.; Mishra, A.; Sutherland, B. A.; O'Farrell, F. M.; Buchan, A. M.; Lauritzen, M.; Attwell, D., Capillary pericytes regulate cerebral blood flow in health and disease. *Nature* **2014,** *508* (7494), 55-60.

105. Gjedde, A.; Kuwabara, H.; Hakim, A. M., Reduction of functional capillary density in human brain after stroke. *Journal of Cerebral Blood Flow & Metabolism* **1990,** *10* (3), 317-326.

106. Klein, B.; Kuschinsky, W.; Schrock, H.; Vetterlein, F., Interdependency of local capillary density, blood flow, and metabolism in rat brains. *American Journal of Physiology-Heart and Circulatory Physiology* **1986,** *251* (6), H1333-H1340.

Acknowledgement

It is my privilege to express my sincere gratitude to those who helped me complete my Master-Doctoral course.

First of all, I would like to express my deepest gratitude to my advisor, HyungJoon Cho, who guided and encouraged me to successfully complete my combined Master-Doctoral course. For the last six years, he has continuously inspired me to keep researching. I would like to show my respect for not only his academic accomplishments but also his kindness and generosity. Also, I would like to thank my committee members, Professor Joon-Mo Yang, Woonggyu Jung, Jung-Hoon Park, and Jae-Hyeok Lee for their professional advisement and comments on this thesis.

I would like to express my appreciation to our lab members for their enormous help and genuine advice. Our lab members HoeSu Jung, SoHyun Han, and DongKyu Lee taught me overall research-related processes including MRI experiments and image processing. Also, Seokha Jin, Hansol Lee, MinJung Jang, HwaPyeong Cho, Soonji Lee, Yelim Gong, Tessema Abel Worku, and YoonKyung Jun supported my researches with productive discussions. It was a great pleasure researching with them. Over the last six years, I have made great memories because of them. I hope we can keep in touch with each other after graduation. I hope for their successful research career.

I would like to thank my friends for their support. They encouraged me to complete my Ph.D. degree. For over a decade, they always welcomed me and listened to my problems. I hope each of us will accomplish our dreams shortly.

Lastly, I want to express my gratitude to my family. Their endless support always kept me mentally stable. Regarding my problems, they always provided me a correct answer, which for a clear pathway in my life. Without their support, I would not complete my Master-Doctoral course.